**UNIVERSITÄTSKLINIKUM HAMBURG-EPPENDORF**

# Physically-motivated analysis and modelling methods of MRI data

**Dissertation**

zur Erlangung des Doktorgrades Dr. rer. biol. hum.
an der Medizinischen Fakultät der Universität Hamburg

vorgelegt von:

Björn Diethard Fricke
aus Hamburg

Hamburg 2025

**Angenommen von der**
**Medizinischen Fakultät der Universität Hamburg am: 15.12.2025**

**Veröffentlicht mit Genehmigung der**
**Medizinischen Fakultät der Universität Hamburg.**

| | |
|---|---|
| **Prüfungsausschuss, der/die Vorsitzende:** | **Prof. Dr. Siawoosh Mohammadi** |
| **Prüfungsausschuss, zweite/r Gutachter/in:** | **Prof. Dr. Lars Ruthotto** |
| **Prüfungsausschuss, dritte/r Gutachter/in:** | **Prof. Dr. René Werner** |

Table of contents

# 1 Introduction

The diffusion MRI (dMRI) technique enables the possibility to measure tissue microstructure parameters, which is done by acquiring multiple measurements which estimate the diffusion along different spatial directions (Callaghan et al., 1988; Le Bihan et al., 1988; Stejskal and Tanner, 1965). So far, most of the research focus is on brain dMRI (e.g., brain development (Dubois et al., 2014; Miller et al., 2002), aging (Draganski et al., 2011; Sullivan et al., 2010)); however, other regions of the human body like the spinal cord are experiencing a growing interest (Cohen et al., 2017; Martin et al., 2016). Also, ex vivo DWI studies which enable the possibility to measure dedicated parts of the body at a sub-millimeter resolution and thereby bridge the spatial gap to other measurement techniques (e.g., electron microscopy) are increasingly becoming the focus of attention (Barazany et al., 2009; Kelm et al., 2016; Papazoglou et al., 2024).

dMRI measurements are affected by artifacts like motion (Andersson and Sotiropoulos, 2016), eddy currents (Mohammadi et al., 2010), noise (Becker et al., 2014; Veraart et al., 2016), Rician bias (Oeschger et al., 2023a), or susceptibility artefacts (Gu and Eklund, 2019; Ruthotto et al., 2012) which can be corrected retrospectively with software tools based on physical models via preprocessing. There are several software applications to correct these types of artefacts (e.g., the FMRIB Software Library (FSL[1]) (Jenkinson et al., 2012), MRtrix[2] (Tournier et al., 2019), DESIGNER[3] (Ades-Aron et al., 2018)). Most of the developed tools are made only for brain dMRI datasets.

[1] https://fsl.fmrib.ox.ac.uk/fsl

[2] https://www.mrtrix.org/

[3] https://github.com/NYU-DiffusionMRI

For the interpretation of the results and the estimation of diffusion parameters, different model fit approaches like diffusion tensor imaging (DTI) (Basser et al., 1994) or diffusion kurtosis imaging (DKI) (Hansen et al., 2016; Jensen et al., 2005) are used. These models use the different diffusion gradient strengths/directions to estimate the diffusion tensor or kurtosis tensor via cumulant development of the logarithmic diffusion weighted signal in dependence of the diffusion strength (Kiselev, 2017).

Furthermore, biophysical models have been developed for the white and gray matter, allowing a deeper characterization of the tissue properties. These approaches link the diffusion parameter maps to biological microstructure. For this, the biophysical models NODDI-DTI (Edwards et al., 2017) or WMTI-Watson (Alexander et al., 2019; Novikov et al., 2019) are often used approaches to estimate biophysical parameters like axonal water fraction ($AWF/f$) or extra-axonal diffusivities ($D_{e,par}$ and $D_{e,perp}$). Typically, biophysical modelling toolboxes like NODDI (Zhang et al., 2012) or SMI (Coelho et al., 2022) do not provide preprocessing options or pipelines.

Therefore, it is necessary to use additional preprocessing tools to analyze a whole dataset from raw data to diffusion or biophysical parameters. For optimal performance, each of these tools has to be optimized for the specific body part being measured. In addition, existing software packages often have their own input syntax, data structure, or own data formats (e.g., ".mif" file format in FSL). This implies a high amount of work to make the output of each single tool compatible with the next (e.g., when biophysical modelling toolboxes are used after preprocessing), is error-prone, and reduces the reproducibility in the field of diffusion MRI. Moreover, the different formats make it more difficult to structure the output of the processing steps, which complicates the analysis of, e.g., a high number of different datasets in one study. This results in low flexibility, as for example, the addition of a preprocessing tool could require manual interaction in the whole analysis code and data structuring script.

In this thesis, a toolbox was developed that is the first to solve these weaknesses in analysis pipelines and open the possibility to analyze in vivo brain as well as in vivo spinal cord and ex vivo datasets in a way which is automatable and applicable for big data analyses. This was achieved by adding additional tissue type-specific preprocessing options via code extensions and new modules to an existing brain dMRI analysis toolbox named now "A Comprehensive Toolbox for Image Processing and Modeling of Brain, Spinal Cord, and Ex Vivo Diffusion MRI Data" (ACID[4]) (David et al., 2024). In particular, the specific types of artifacts in spinal cord dMRI (Barker, 2001; Stroman et al., 2014), as well as the highly variable geometry and diffusion properties in ex vivo dMRI ((Sébille et al., 2019) provides a list of ex vivo/ postmortem dMRI studies), are addressed. ACID is an open-source extension to the MATLAB[5] based Statistical Parametric Mapping (SPM[6]) (Penny et al., 2011) software and therefore benefits from a GUI and strong, well-established statistical analysis functions and modules from the SPM framework (e.g., (Ashburner and Friston, 2011)). The ACID toolbox includes state-of-the-art image preprocessing and artefact correction tools, the model fitting approaches DTI and DKI, as well as the biophysical parameter estimation methods NODDI-DTI and WMTI-Watson. As one of the strengths of ACID is the modularized code structure, external tools like FSL's eddy[7] (Andersson and Sotiropoulos, 2016) have been easily implemented. ACID offers a fully modularizable software which enables an easy creation of analysis pipelines consisting of several modules. The implementation of additional processing/modelling methods is possible without a high amount of work or the need for major changes in analysis pipelines or data structuring

[4] http://diffusiontools.com/

[5] https://www.mathworks.com

[6] https://www.fil.ion.ucl.ac.uk/spm/

[7] https://fsl.fmrib.ox.ac.uk/fsl/fslwiki/eddy

scripts. In addition, other SPM extensions (e.g., the hMRI-toolbox[8,9] (Tabelow et al., 2019)) can be directly integrated into analysis pipelines without changes on the code level. Furthermore, ACID includes the Brain Imaging Data Structure (BIDS) standard (Gorgolewski et al., 2016; Karakuzu et al., 2022) and is therefore applicable to big data analysis, which is required for, e.g., machine learning applications (e.g., Clinica (Routier et al., 2021)). The parameters of the ACID modules can be easily adjusted to support required tissue type. The use of the SPM-provided GUI as well as the modular organization of ACID and additional comfort utility functions (e.g., automatic metadata readout), make the toolbox user-friendly for unexperienced users. To ensure ACID is valuable and reusable academic software, the FAIR principles (Barker et al., 2022; Wilkinson et al., 2016) are harmonized with the toolbox.

To show the capabilities ACID provides, the analyses of example datasets for the three supported body regions are presented, while each processing step is shown. Furthermore, the effect of different artefacts (Kurtosis bias (Edwards et al., 2017), Rician bias) on parameter estimation is presented.

To investigate the performance of different denoising methods, a comparison via a synthetic dMRI dataset is presented, in which all denoising methods which are integrated in ACID (even methods from external sources like FSL) have been compared.

The capability of ACID to process and analyze multiple datasets (group analysis) BIDS-conform is demonstrated by the processing of an example study containing four datasets and the comparison of parameter estimates when different biophysical model approaches are used.

---

[8] https://www.cbs.mpg.de/abteilungen/neurophysik/software/hmri-toolbox

[9] https://github.com/hMRI-group/hMRI-toolbox

# 2 Structure of the thesis

In addition to the introduction (section 1) and this section, this thesis consists of six further sections. The following list provides an overview for each of these sections:

- Section 3 gives an overview of the theoretical background. The goal of this section is to give the reader an introduction of the required knowledge to understand the need for a toolbox for preprocessing and interpreting diffusion MRI data. First, the theory behind an MRI measurement is explained and how diffusion can be acquired. Also, models for fitting the acquired diffusion signals and how parameters can be estimated are described. Furthermore, biophysical models are introduced. On the technical side, the MRI sequence for a diffusion measurement is explained and typical artefacts for dMRI measurements are introduced and explained.
- Section 4 focuses on the concept changes and developments which were performed for ACID. The organization of the ACID code is explained, and the benefits ACID features through its integration into SPM are discussed. The refactoring of the ACID toolbox is presented in the beginning with a description of the initial state of ACID at the beginning of the PhD project, and the changes which are performed are explained in several sections like conceptual changes, the implementation of the BIDS structure, and the harmonization with the FAIR principles.
- Section 5 is based on the toolbox paper published during this PhD project (David et al., 2024) (see section 14 for details) and has the goal of presenting all modules implemented in ACID and their usage.
- Section 6 is partially based on the toolbox paper published during this PhD project (David et al., 2024) (see section 14 for details; the specific parts are named in section 6) and provides exemplary investigations and use cases for ACID. The section explains the settings of the three ACID-supported tissue types: in vivo brain, in vivo

spinal cord, and ex vivo specimen. Also, this section shows, for example, how a user can decide which biophysical model should be used for a specific dataset. In addition, an exemplary group analysis is presented showing a comparison of biophysical parameter estimations over different estimation models. Furthermore, the group analysis demonstrates the possibilities ACID provides now for large dataset analyses through, e.g., BIDS integration or pipeline generation.

- Sections 7 and 8 provide a general discussion, summarizing the results, and give a conclusion and outlook.

The development of ACID is an ongoing process, and updates are released continuously. The current commit for this thesis is "[132b548c][10]" and can be found on the git repository website[11].

[10] 132b548ccb895b2000a59092ceb9edb693edb44e

[11] https://bitbucket.org/siawoosh/acid-artefact-correction-in-diffusion-mri/src/master/

# 3 Theoretical background

In this section, the fundamental principles of magnetic resonance imaging (see section 3.1), the principles of diffusion MRI (see section 3.2), a description of biophysical models (see section 3.3), as well as the challenges for diffusion MRI datasets (see section 3.4) are explained.

## 3.1 Fundamentals of Magnetic Resonance Imaging (MRI)

This section highlights the general fundamentals an MRI is based on, containing the basic principles (see section 3.1.1; structure is based on (Fricke, 2020)), how the excitation and echo are generated (see section 3.1.2), the spatial encoding techniques (see section 3.1.4), and an explanation of the k-space (see section 3.1.5).

### 3.1.1 Basic principles of Magnetic Resonance Imaging (MRI)

Magnetic Resonance Imaging (MRI) is a non-invasive imaging technology which uses the physical principles of Nuclear Magnetic Resonance (NMR), where the nuclear spin (usually hydrogen nuclei; because the human body consists largely of it) interacts with external magnetic fields. The main static magnetic field is named $B_0$ field.

The hydrogen nuclei consist of one proton with nuclear spin $\frac{1}{2}$. This leads to a magnetic moment which interacts with the $B_0$ field, usually oriented along the $z$-axis. Due to the rules of spin algebra, the spins align parallel- or anti-parallel to this field and precess around this axis because of their behavior as a magnetic dipole in a magnetic field (Dössel, 2016). The vector sum of all magnetic dipoles in one volume element (voxel) is named magnetization $\vec{M}$ and can be described as (Dössel, 2016):

$$\vec{M} = \frac{d\vec{m}}{dv} = \frac{vector\ sum\ of\ all\ magnetic\ dipomoments\ in\ dv}{volume\ dv}. \quad (1)$$

In MRI acquisitions, the spatial density of this magnetization is measured.

The precessing spins are not phase coherent (thermal equilibrium), and no transversal magnetization builds up (because $B_0$ is here in $z$-direction (longitudinal), the magnetization can be simplified to $\vec{M} = M_z$). The frequency of the precession movement is dependent on the strength of the magnetic field and named Larmor frequency

$$\omega_{Larmor} = \gamma \cdot B_0, \tag{2}$$

where $\gamma$ is the gyromagnetic ratio and $B_0$ is the magnetic field strength (e.g., 3T). The gyromagnetic ratio for hydrogen is $\gamma_H = 42{,}576 \frac{MHz}{T}$.

The two different spin states (parallel and anti-parallel) have two different energy levels due to the Zeeman-Effect

$$E = \pm\frac{1}{2} \cdot \gamma\hbar \cdot B_0 \tag{3}$$

(positive sign is anti-parallel, negative sign is parallel alignment) (Dössel, 2016; Zeeman, 1897). This leads to a difference between both energy states

$$\Delta E = \gamma\hbar \cdot B_0 \tag{4}$$

As the parallel state has a lower energy, more spins are in this alignment. The difference in the number of spins of both states can be described via the Boltzmann-Distribution

$$N_i = N_0 \cdot e^{-\frac{\Delta E}{\kappa_B T}}, \tag{5}$$

where $N_0$ is the number of spin states, $\kappa_B$ is the Boltzmann constant, and $T$ is the temperature (Dössel, 2016). The number of spin states can be described by the sum of both $N = N_{parallel} + N_{antiparallel}$. Together with the formula of the Boltzmann distribution, the number of spins in the antiparallel state can be described as

$$N_{antiparallel} = N_{parallel} \cdot e^{-\frac{\Delta E}{\kappa_B T}} = N_{parallel} \cdot e^{-\frac{\gamma\hbar \cdot B_0}{\kappa_B T}}. \tag{6}$$

With the approximation that $\gamma\hbar \cdot B_0$ is much smaller than $\kappa_B T$, the formula can be simplified to

$$N_{antiparallel} \approx N_{parallel} \cdot \left(1 - \frac{\gamma\hbar \cdot B_0}{\kappa_B T}\right). \tag{7}$$

The formula of the difference between both states, therefore, is

$$\Delta N = N_{parallel} - N_{antiparallel} \approx N_{parallel} \cdot \frac{\gamma\hbar \cdot B_0}{\kappa_B T}. \tag{8}$$

With the assumption that $N_{parallel} \approx \frac{N}{2}$ follows that

$$\Delta N \approx \frac{N}{2} \cdot \frac{\gamma\hbar \cdot B_0}{\kappa_B T} \tag{9}$$

This difference is the reason for a longitudinal magnetization $M_z$ (Liang and Lauterbur, 2000), which is used in MRI measurements.

### 3.1.2 Excitation of the spin system and echo

The phenomena described in the section 3.1.1 make it possible to excite the spin system with an oscillatory electromagnetic high frequency (HF, $B_1$) wave which is perpendicular to the $B_0$ field (commonly $B_0$ field in $z$-direction, $B_1$ wave in $xy$-plane). To excite the spin system, the frequency must be the Larmor frequency to be in resonance with the spin system, which is necessary to be able to perturb the spin system (Dössel, 2016). The Larmor frequency is, e.g., $127.728\,MHz$ for hydrogen in a 3 Tesla magnetic field. This frequency can be described as "radio frequency" (RF), which shows that no ionizing radiation is used for MRI measurements. If a spin system is excited this way, the longitudinal magnetization (here, e.g., $M_z$) is flipped into the $x$-$y$ plane. The angle of the flip ($\alpha$) is dependent on the amplitude of the transversal field ($B_1$) and duration ($\tau$) of the HF pulse:

$$\alpha = \gamma \cdot B_1 \cdot \tau. \tag{10}$$

Figure 1 shows a visualization of this phenomenon.

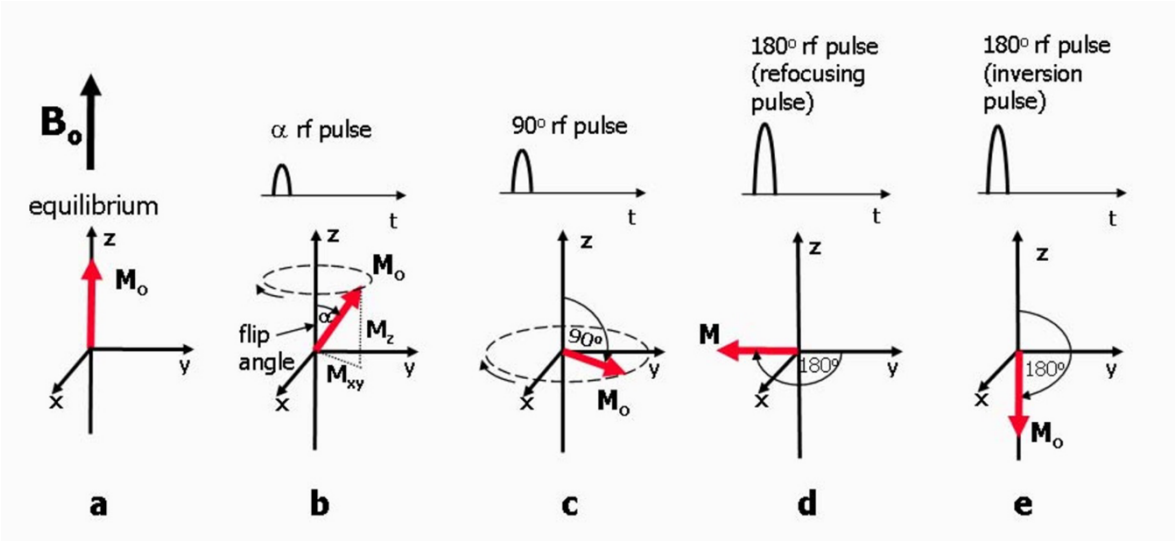


Figure 1: Net Magnetization, rf pulses and flip angle. a) At equilibrium, the net magnetization, $M_0$ is at equilibrium, aligned along the $z$-axis. b). When a rf pulse is applied, $M_0$ makes an angle with the $z$-axis, known as the flip angle, and rotates around the axis in the direction of the curved arrow. At any instant the magnetisation can be split into two components, $M_z$ and $M_{xy}$. The rotating $M_{xy}$ component generates the detectable MR signal. c) The maximum detectable signal amplitude after a single rf pulse occurs when $M_0$ lies entirely in the plane of the $x$ and $y$ axes as this gives the largest $M_{xy}$ component. This pulse has a 90° flip angle and is referred to as a 90° rf pulse or saturation pulse. d) A 180° rf refocusing pulse is usually applied while there is transverse magnetisation already rotating in the $xy$ plane and is used to instantaneously flip the transverse component of magnetisation through 180° about an axis also rotating in the $xy$ plane. e) A 180° inversion pulse is usually applied at equilibrium and is used to rotates the net magnetization through 180° from the positive to the negative $z$-axis. This is also known as a magnetization preparation pulse and is used is the preparation scheme for black blood imaging techniques. Source: Figure and modified caption reproduced from (Ridgway, 2010), published under CC BY 2.0 license.

During this process $M_z$ decreases while the transverse magnetization $M_{xy}$ increases. This $M_{xy}$ magnetization precedes in phase and also with the Larmor frequency. Through this pulse, an energy transfer is performed, which results not only in the excitation of the spin

system but also in a heating of the specimen/subject. Therefore, the duration and amplitude of the HF pulses are limited to the allowed heating of the subject. Immediately after the excitation pulse, the spin system starts to relax back to its ground state magnetization ($M_{xy}$ decreases while the longitudinal magnetization $M_z$ increases). The underlying relaxation process consists of two parts:

(1) The longitudinal magnetization $M_z$ which is flipped due to excitation in the $xy$-plane, relaxes back to the ground state ($z$-axis). This happens because of interactions of the spin system with, e.g., other atoms (often named: spin-lattice-relaxation), which result in an energy loss (e.g., heating). The longitudinal relaxation time $T_1$ (e.g., $680 \pm 120$ ms for white matter) is defined via the formula (assuming $M_z = 0$ for $t = 0$):

$$M_z(t) = M_0 \cdot \left(1 - e^{-\frac{t}{T_1}}\right), \tag{11}$$

where $M_0$ is the magnetization of the ground state (before excitation) (Dössel, 2016).

(2) The spins within the $xy$-plane lose their coherence with increasing time due to their own magnetic fields which interact with each other or local differences in the magnetic field of the measured volume element which result in precession of different Larmor frequencies. This results in a decrease of the length of the transverse magnetization $M_{xy}$. This relaxation type (often named: spin-spin-relaxation) is defined via the formula:

$$M_{transversal}(t) = M_{transversal}(0) \cdot e^{-\frac{t}{T_2}}, \tag{12}$$

where $T_2$ (e.g., $92 \pm 22$ ms for white matter) is the transversal relaxation time (Dössel, 2016).

The precessing spins in the $xy$-plane can be defined as a time-varying magnetic field which induces a voltage (which can be defined as an echo or signal $S$) in, e.g., detector coils placed

around the measured object, due to Faraday's law of induction (Griffiths, 2013). This type of echo, which can be measured directly after the excitation of the spin system, is named "free induction decay" (FID). However, the FID is not usable for MRI applications as the relaxation times are in general shorter than $T_2$. Due to inhomogeneities of the $B_0$ field, an acceleration of the dephasing of the spins is caused. The therefore modified spin–spin relaxation time $T_2$ is named $T_2^*$ and is defined as:

$$\frac{1}{T_2^*} = \frac{1}{T_2'} + \frac{1}{T_2} \,, \tag{13}$$

where $T_2'$ defines the additional acceleration in relaxation.

### 3.1.3 Echo generation

As described in section 3.1.2, the FID signal is not usable for MRI applications. But there are several techniques using gradients and/or RF pulses to generate an acquirable echo.

One of these techniques is named gradient echo. For this method, a gradient is applied after the excitation, which results in an additional (faster) dephasing of the spins and a faster vanishing of the FID. After that, a second gradient is applied with the same amplitude but double length and opposite direction. The additional dephasing of the first gradient is therefore neglected, and the FID re-appears as a measurable echo limited for its maximum by the $T_2^*$ relaxation. The time from the excitation to the point where the echo reaches its maximum is named generally echo time ($TE$). Figure 2 provides a visualization of the gradient echo sequence principle.

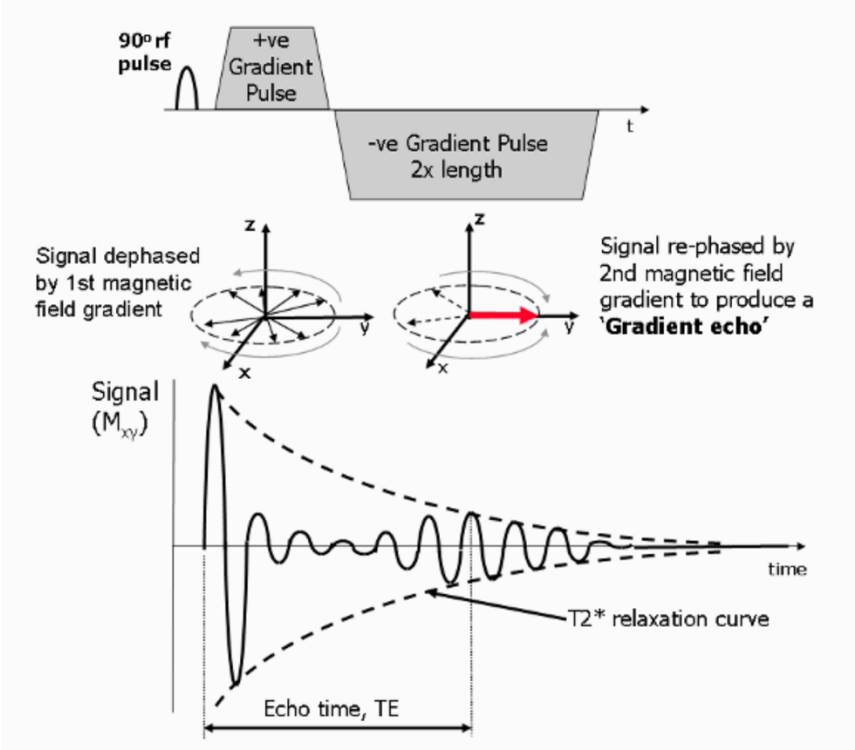


Figure 2: Generating a gradient echo. This diagram shows how the reversal of a magnetic field gradient is used to generate a gradient echo. The application of the 1st positive magnetic field gradient causes rapid de-phasing of the transverse magnetization, $M_{xy}$, and therefore the FID signal to zero amplitude. The application of the 2nd negative magnetic field gradient reverses the de-phasing caused by the first gradient pulse, resulting in recovery of the FID signal to generate a gradient echo at the echo time, TE. Extension of the time duration of the second gradient to twice that of the first gradient causes the FID to then de-phase to zero. The maximum amplitude of the echo depends on both the $T_2^*$ relaxation rate and the chosen $TE$. Source: Figure and modified caption reproduced from (Ridgway, 2010), published under CC BY 2.0 license.

Another technique is named spin echo. The technique uses an 180° RF pulse after the relaxation time $T_2^*$ which changes the signs of all spins within the spin ensemble. This results in a rephasing of the spin ensemble, and the FID re-appears as a measurable echo. One advantage of this technique is that the 180° pulse compensates for the inhomogeneities of the magnetic field, due to the spins perceiving the same inhomogeneities on their return path

with the opposite sign. As a result, the relaxation only occurs with $T_2$ instead of $T_2^*$. Figure 3 provides a visualization of the spin echo sequence principle.

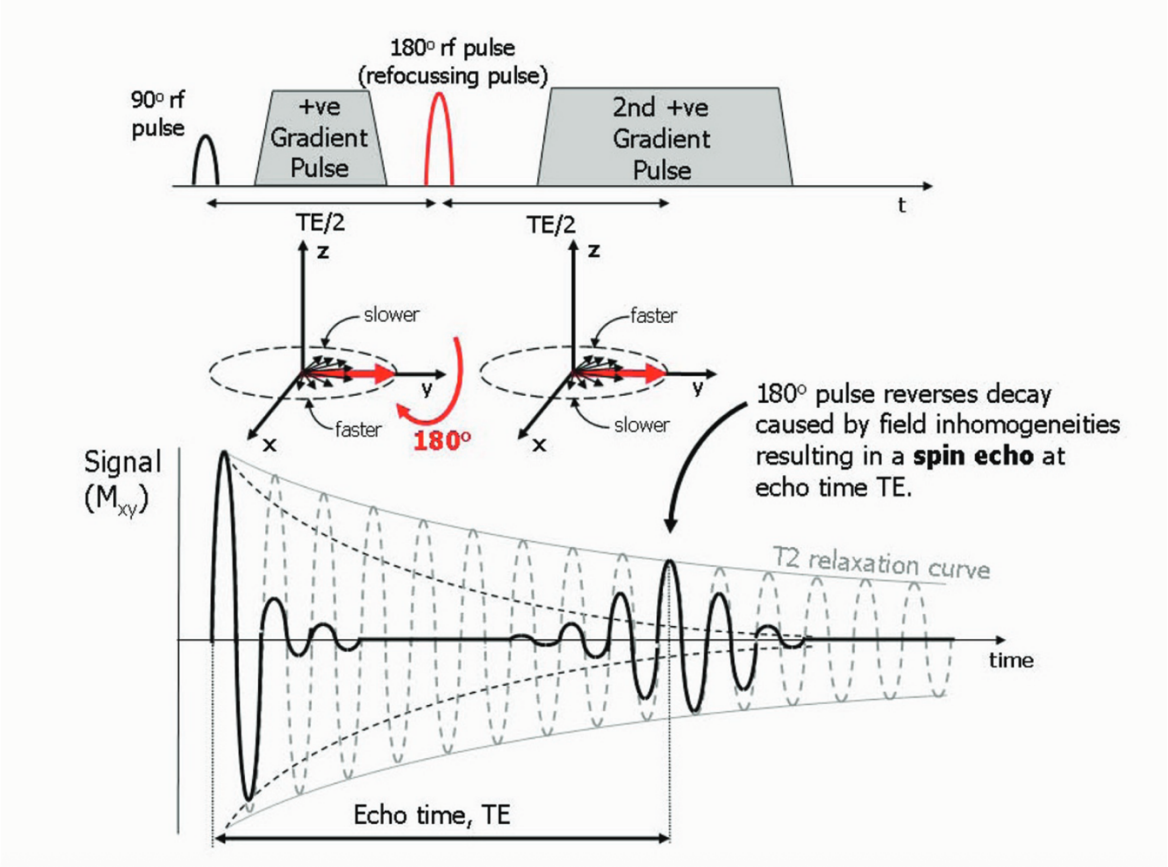


Figure 3: Generating a spin echo. The presence of magnetic field inhomogeneities causes additional de-phasing of the proton magnetic moments. The Larmor frequency is slower where the magnetic field is reduced and faster where the field is increased resulting in a loss or gain in relative phase respectively. After a period of half the echo time, $TE/2$, the application of a 180° rf pulse causes an instantaneous change in sign of the phase shifts by rotating the spins (in this example) about the y axis. As the differences in Larmor frequency remain unchanged, the proton magnetic moments the move back into phase over a similar time period, reversing the de-phasing effect of the magnetic field inhomogeneities to generate a spin echo. In addition to the effect of the 180° refocusing pulse, gradients are applied to de-phase and re-phase the signal for imaging purposes. Note that for spin echo pulse sequences, the second gradient has the same sign as the first, as the 180° pulse also changes the sign of the phase shifts caused by the first

gradient. Source: Figure and caption reproduced from (Ridgway, 2010), published under CC BY 2.0 license.

This procedure can be repeated with an additional 180° RF pulse. This results in a so-called "Echo-Train" where multiple echoes are generated for one excitation and is used for, e.g., echo planar imaging (EPI) readout approaches.

### 3.1.4 Spatial encoding

The further described excitation would result in a signal without any spatial information as all spin systems in the $B_0$ would precess with the same Larmor (resonance) frequency and would be excited when an RF pulse is applied. Therefore, a spatial encoding is used to enable the possibility to combine the spatially encoded signals into one image. To spatially encode in three dimensions, three different encoding techniques are needed:

(1) For the z-direction, typically an additional magnetic gradient $G_S$ is added to the $B_0$ field. As the strength of the magnetic field varies, therefore, along the $z$-axis, the Larmor frequency becomes spatially dependent along this direction. This enables the possibility to only excite a single slice of the measured subject by applying an RF pulse with the corresponding Larmor frequency (slice selection). Figure 4 shows a visualization of the slice selection technique.

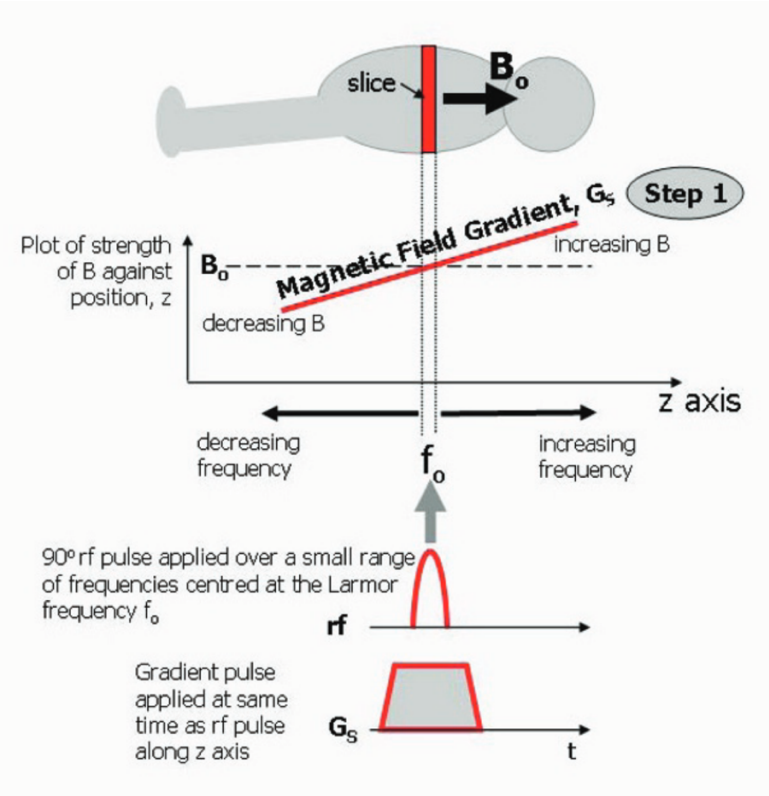


Figure 4: Image formation, Step 1 - Selecting a slice. For step 1 of image formation process, a slice of tissue is selected by applying a magnetic field gradient $G_S$ at the same time as the rf excitation pulse. The position along the gradient (in this example along the $z$ axis) determines the Larmor frequency and resonance only occurs where this matches the frequency of the rf pulse, $f_0$, defining a plane (slice) of tissue perpendicular to the $z$-axis. In practice the rf pulse is applied over a small range of frequencies, thus defining the thickness of the slice. Source: Figure and modified caption reproduced from (Ridgway, 2010), published under CC BY 2.0 license.

(2) To encode along the $y$-direction in the excited slice, phase encoding is used. This encoding technique uses an additional gradient $G_P$ after the slice selection but before the echo. This makes the phase of the spins linearly dependent along the $y$-direction. To use this phase shift for spatial encoding, this step has to be repeated with different phase encoding gradient strengths. Figure 5 shows a visualization of this encoding technique.

(3) To encode the $x$-direction, an additional gradient $G_F$ during the echo (readout) is applied. This makes the acquired frequencies linearly dependent along this direction as the Larmor frequencies are now spatially dependent. Figure 5 shows a visualization of this encoding technique.

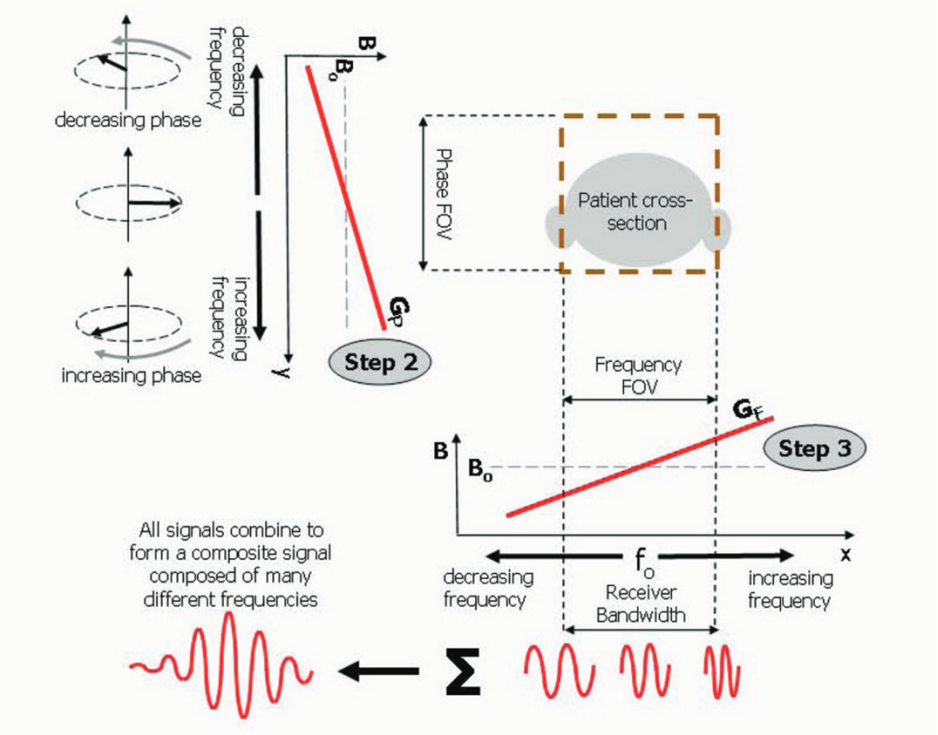


Figure 5: Image formation, Steps 2 & 3 - Phase and frequency encoding. For step 2 of the image formation process, a phase encoding gradient, $G_P$, is applied in a direction along the selected image plane (in this case the phase encoding direction is along the $y$-direction). This causes a range of phase shifts of the proton magnetic moments dependent on their position along the gradient as well as the slope and duration of the gradient. For step 3, following the phase encoding gradient, the frequency encoding gradient, $G_F$, is applied also in the plane of the selected slice but perpendicular to the phase encoding direction. The MR signal echo is measured during this period. The frequency encoding gradient determines the Larmor frequency according to position along its direction (in this case, the $x$ direction). The detected MR signal from the slice of tissue is therefore comprised of many different frequencies. The field of view is predefined and matched to a specific range of frequencies, referred to as the receiver

bandwidth. Source: Figure and modified caption reproduced from (Ridgway, 2010), published under CC BY 2.0 license.

These three encoding techniques make it possible to acquire the signal for several separated volume element (voxel).

### 3.1.5 k-Space

As described in section 3.1.4, the signal of an MRI acquisition is a spatially encoded electromagnetic echo. This represents a sampling of discrete areas in a reciprocal space (named $k$-space) which can be seen as the Fourier transformation of the acquired image. This matrix is filled with frequency values during the MRI measurement. After the acquisition, the filled matrix can be inverse Fourier transformed to calculate the acquired image. An MRI can only acquire spatially discrete areas in the $k$-space; therefore, the image quality depends on the sampling of the acquired $k$-space area.

The $k$-space is symmetric; therefore, it is only mandatory that more than $50\%$ are sampled. Also, the location of the acquired $k$-space area influences the resulting image. The center of the $k$-space includes predominantly the intensity values, as the outer regions include retrospectively predominantly the tissue structure. An exemplary visualization of this phenomenon is shown in Figure 6 (last sentence in captions belongs to the presented work in (Li et al., 2018)).

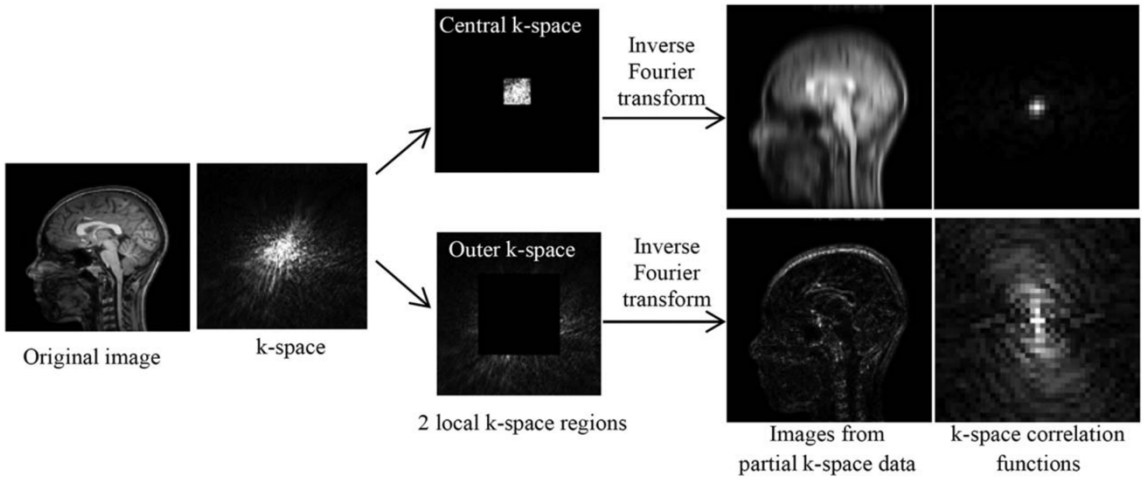


Figure 6: Illustration of tissue-boundary sparsity variation with a brain image. A central and an outer k-space region may each generate an image by inverse Fourier transform. The image generated from outer k-space data have higher tissue-boundary sparsity than that from central k-space data. Correspondingly, the correlation function shows a stronger spread-out pattern around the k-space center, indicating more neighboring data are correlated in the outer than in the central k-space. This k-space variant data correlation associated with tissue-boundary sparsity is used to improve correlation imaging in the presented work. Source: Figure and caption reproduced from (Li et al., 2018). Published online 7 July 2017 in Wiley Online Library (wileyonlinelibrary.com). © 2017 International Society for Magnetic Resonance in Medicine.

## 3.2 Diffusion MRI

The in section 3.1 described operating principles for an MRI can be used within sequences (see section 3.2.2 for details) to perform measurements. One of these sequences enables the measurement of diffusion (see section 3.2.1 for details) within the measured subject. Furthermore, the interpretation of the diffusion signal is described (see section 3.2.3 for details).

### 3.2.1 Diffusion

Diffusion can be explained as microscopic arbitrary motion (Brownian motion) (Einstein, 1956) of molecules if a concentration gradient is present. This phenomenon is

mathematically described by Fick's laws of diffusion (Meschede, 2010). As in an MRI measurement, only hydrogen atoms are acquired, there is initially no concentration gradient. The concentration gradient is created during the diffusion-weighted measurement (see section 3.2.2) because there, hydrogen molecules are "labeled", which results in a concentration gradient of labeled and unlabeled molecules.

### 3.2.2 Diffusion MRI sequence

A diffusion-weighted sequence consists of additional gradients which are named diffusion gradients. After the excitation pulse (90° flip angle, combined with a slice selective gradient), a diffusion gradient is applied which applies an additional phase shift (similar to the in section 3.1.3 discussed gradient echo). After the application, a 180° slice selective (same slice as for the 90° pulse) HF pulse is applied followed by a second diffusion gradient with the same length and strength as the first. As the 180° HF pulse switches the signs of the phases (similar to the in section 3.1.3 discussed spin echo), the second gradient neglects the phase shift of the first diffusion gradient for spins which have not moved. Spins which have moved do not collect the same phase shift during the application of the second reversed gradient compared to the first one. Therefore, these spins are not in phase after the application of both diffusion gradients and do not contribute to the following acquirable echo. This principle makes it possible to measure the strength of the diffusion as the measured echo depends on the strength of water diffusion inverted (higher diffusion → weaker echo (Stejskal and Tanner, 1965).

A widely used diffusion sequence is a combination of a pulsed-gradient spin-echo (PGSE) sequence for diffusion weighting with a spin echo planar imaging (SE-EPI) approach for spatial encoding. An example of this pulse sequence is displayed in Figure 7. As for diffusion signal models, multiple acquisitions with different $b$-values and $b$-vectors are required (see

section 3.2.3 for details); this allows the measurement of a whole DWI dataset in a suitable time for a human subject ($< 1\ h$).

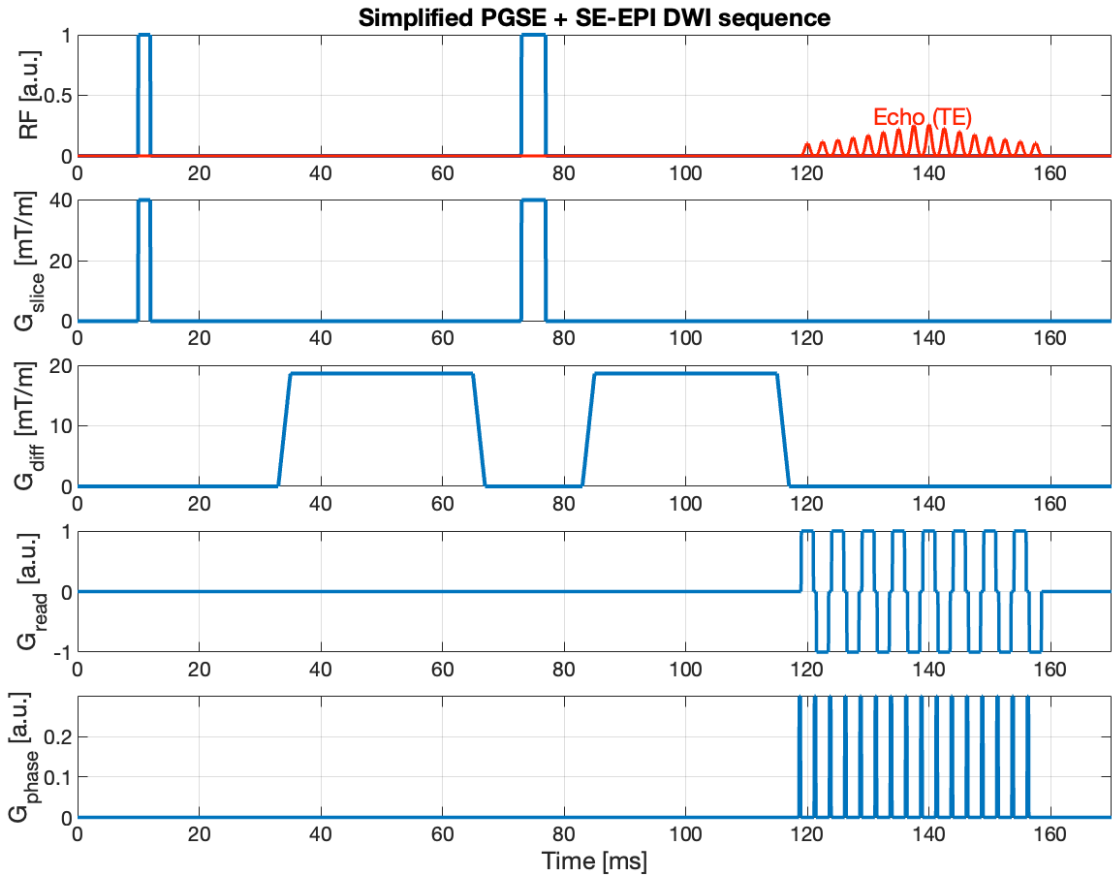


Figure 7: Simplified spin-echo dMRI pulse sequence (PGSE + SE-EPI). First, a slice selective 90° RF pulse is applied. Two trapezoidal diffusion lobes ($G_{diff}$) are applied with the same hardware polarity; the 180° RF pulse is placed midway between their effective centers (including ramps). Readout and phase-encoding begin after the second lobe, and the readout is centered at the peak of TE. The RF panel overlays an echo train whose amplitudes follow a $T_2$* envelope (peak at TE) with global $T_2$ scaling. Plotting code, and caption was created by the use of ChatGPT5 (https://chatgpt.com/).

### 3.2.3 Interpretation of the diffusion signal

Diffusion MRI (dMRI) investigates the thermally driven, random motion of water molecules. A molecule's displacement $x - x_0$ over a diffusion time $t$ can be modeled as the sum of many short, uncorrelated steps. The mathematical construct to describe this behavior is called Green's function or diffusion propagator (Kiselev, 2017). The diffusion

propagator $\mathcal{G}(t, x, x_0)$ is the probability density that a molecule moves from position $x_0$ to $x$ during time $t$. In free, homogeneous media, $\mathcal{G}$ is Gaussian with a variance equal to the sum of the variances of the underlying elementary steps. The diffusion propagator describes the behavior for each molecule in a voxel and is therefore not tractable practically (Kiselev, 2017). Therefore, a frequently used quantity is the medium-averaged propagator $G(\Delta x, t)$, which describes only the net displacement $\Delta x = x - x_0$ and is obtained by averaging over all starting positions of molecules in the voxel. Under standard assumptions (constant spin density within a voxel and negligible relaxation differences across diffusion encodings), the measured diffusion-weighted signal $S(t, q)$ is the Fourier transform of the medium-averaged propagator:

$$S(t, q) = \int G(\Delta x, t) \cdot e^{-i \cdot q \cdot \Delta x} \, d^3 \Delta x, \tag{14}$$

where $q$ defines the area under a single diffusion-encoding gradient lobe, often called the "wave vector" of the sequence, which sets the spatial direction and strength of the displacement encoding (Kiselev, 2017).

The strength of the diffusion gradient is mathematically expressed via the $b$ value which describes the sensitivity of the acquisition to movement of water molecules (diffusion). A $b$-value of 0 results in no diffusion sensitivity ($b_0$ image). These images are needed for the interpretation of the signal profile but are also acquired to include images without diffusion-related artefacts (see section 3.4 for details) to the measured datasets. Higher $b$-values result in a weaker echo due to the higher sensitivity to diffusion. Therefore, the SNR is reduced as the higher the $b$-value is, which limits the maximum $b$-value which can be acquired. The signal can be mathematically expressed as:

$$S(b) = S_0 \cdot e^{-b \cdot D}, \tag{15}$$

where $b = q^2 \cdot t$ , $D$ is the diffusion coefficient and $S_0$ is the non-diffusion-weighted signal (Kiselev, 2017).

For the interpretation of the diffusion-weighted signal, several diffusion signal models exist like Diffusion Tensor Imaging (DTI) or Diffusion Kurtosis Imaging (DKI).

In the DTI approach, the diffusion is assumed to be Gaussian in a homogeneous fluid. Therefore, the logarithm of the normalized signal decay can be approximated linearly with $b$:

$$ln\frac{S(b)}{S_0} \approx -b \cdot D. \tag{16}$$

This linear relation is obtained by Taylor expanding the signal at low $q$ (equivalently, low $b$) under the condition $q \cdot \Delta x \ll 1$. This very short movement can be treated as Gaussian which is described by $D$ and where higher orders of the Taylor expansion vanish (Kiselev, 2017). Therefore, DTI is only valid for $b$ values up to $b \approx 1000\frac{s}{mm^2}$ (in vivo).

As the signals $S_0$ and $S$ are acquired during a diffusion measurement, the diffusion coefficient $D$ can be calculated by solving the formula transformed from equation (16):

$$D = \frac{ln\frac{S_0}{S(b)}}{b}. \tag{17}$$

To solve this formula, two measurements would be sufficient. One diffusion weighted image ($S(b)$) and one image without diffusion weighting ($S_0$). The result would be the diffusion coefficient for one direction or, when the diffusion is isotropic, for all directions. As the diffusion is, e.g., in tissue not isotropic, multiple measurements with different diffusion directions are necessary to calculate the diffusion coefficient.

The definition of the diffusion coefficient depends on the medium for which the coefficient is calculated. Differently than for an isotropic medium, for an anisotropic medium, where the diffusion coefficient depends on the direction of diffusion, $D$ can be expressed as a $3 \times 3$ symmetric matrix:

$$D = \begin{bmatrix} D_{xx} & D_{xy} & D_{xz} \\ D_{xy} & D_{yy} & D_{yz} \\ D_{xz} & D_{yz} & D_{zz} \end{bmatrix}, \tag{18}$$

where the diagonal values $D_{xx}$, $D_{yy}$, and $D_{zz}$ are the expressions of diffusion along the named axis. The off-diagonal values $D_{xy}$, $D_{yz}$, and $D_{xz}$ represent correlations between the two named directions. The diffusion coefficient matrix is symmetric for, e.g., water due to the reciprocity theorem and principle of microscopic reversibility of nonequilibrium thermodynamics (Basser et al., 1994). As the diffusion coefficient (18) consists of six independent elements, the minimum number of measurements to estimate the diffusion coefficient are six linearly independent directions (and one measurement without diffusion weighting for $S_0$).

When the diffusion coefficient is calculated, all matrix elements of Equation (18) are filled (see section 5.3 for exemplary algorithms). As the diffusion tensor is symmetric and positive (semi)-definite (because it is determined by the mean squared displacement of molecules (Kiselev, 2017)), it can be diagonalized.

$$D_{diagonal} = Q^T D\, Q, \tag{19}$$

where $Q$ is an orthogonal matrix containing the eigenvectors.

The diagonalized diffusion tensor has then the form

$$D_{diagonal} = \begin{bmatrix} \lambda_1 & 0 & 0 \\ 0 & \lambda_2 & 0 \\ 0 & 0 & \lambda_3 \end{bmatrix}, \tag{20}$$

where $\lambda_1$, $\lambda_2$,and $\lambda_3$ are the eigenvalues; commonly assuming $\lambda_1 > \lambda_2 \geq \lambda_3$.

Eigenvalues and eigenvectors can be seen as the parameters of a diffusion ellipsoid where the eigenvalues define the length along the three orthogonal axes, and the eigenvectors define the orientation. Note that the orientation is aligned with the $x$, $y$, and $z$-axis after diagonalization. A visualization of the diffusion ellipsoid and the effect of diagonalization is shown in Figure 8.

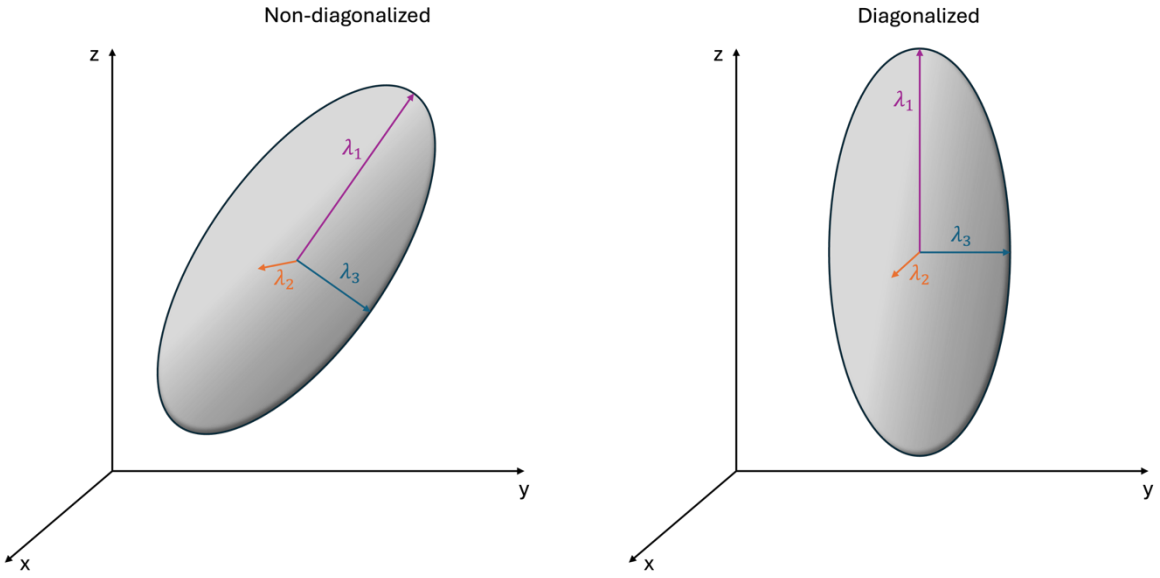


Figure 8: Visualization of the diffusion ellipsoid before (left) and after (right) diagonalization. Diagonalization does not affect the size of the ellipsoid but align the axes with the reference frame.

The eigenvalues are rotational invariant, as a rotation of the ellipsoid would not shrink or stretch the ellipsoid (length of eigenvalues would be unchanged). Therefore, it is possible to estimate invariant diffusion metrics out of the eigenvalues of the diffusion tensor. The typical DTI metrics are mean diffusivity (MD), axial- and radial diffusivity (AD/RD), and fractional anisotropy (FA). These metrics can be calculated via the following formulas:

$$MD = \frac{\lambda_1 + \lambda_2 + \lambda_3}{3} \tag{21}$$

$$AD = \lambda_1 \tag{22}$$

$$RD = \frac{\lambda_2 + \lambda_3}{2} \tag{23}$$

$$FA = \sqrt{\frac{3}{2} \cdot \left( \frac{(\lambda_1 - MD)^2 + (\lambda_2 - MD)^2 + (\lambda_3 - MD)^2}{\lambda_1^2 + \lambda_2^2 + \lambda_3^2} \right)} \tag{24}$$

The DTI model assumes a linear signal decay, which is not valid as an approximation for higher $b$-values where the assumption $q \cdot \Delta x \ll 1$ is not valid and Gaussian diffusion can no longer be assumed. Departures from this strict Gaussian diffusion regime require a further term of the cumulant expansion. Writing the fourth cumulant of displacement in terms of a diffusion kurtosis $K$ yields a second-order approximation:

$$ln\frac{S(b)}{S_0} \approx -b \cdot D + \frac{1}{6} \cdot b^2 \cdot D^2 \cdot K + \cdots, \tag{25}$$

where odd powers are not existent due to the symmetry of the propagator (Kiselev, 2017). This diffusion-kurtosis model captures non-Gaussian features arising from restrictions and heterogeneity of tissue compartments. Therefore, DKI is valid for measured b-values up to $b_{max} \approx 2000 \frac{s}{mm^2}$ (in vivo). The DKI model is an expansion of the DTI model. Therefore, the DTI metrics are estimated by DKI as well as additional kurtosis metrics like mean kurtosis (MK), axial kurtosis (AK), and radial kurtosis (RK). For a detailed explanation of the DKI formalism and definitions of the DKI metrics, see, e.g., (Tabesh et al., 2011).

For a complete interpretable DWI dataset, a sufficient number of directions have to be measured. For DTI, at least six linearly independent directions for one nonzero b-value are required to estimate the diffusion tensor. DKI requires at least 15 linearly independent directions for two different nonzero b-values to estimate the additional kurtosis tensor (Tabesh et al., 2011). In practice, more directions are acquired as this increases the robustness against, e.g., noise.

### 3.3 Biophysical models

The results of DTI and DKI can be used for biophysical models, which enables a connection to the tissue microstructure (Jelescu et al., 2020). For this connection, the dMRI signal is

split into distinguishable components, which can be linked to specific tissue compartments. There are several biophysical models with different approaches.

For example, the NODDI-DTI model was developed to estimate biophysical parameters out of DTI datasets. This is done by excluding CSF compartments out of the NODDI model, which results in a restriction of application to voxels without CSF partial volume contamination (see (Edwards et al., 2017) for further details).

Another example is the white matter tract integrity (WMTI)-Watson model, which is based on the Standard Model (Alexander et al., 2019; Novikov et al., 2019). This approach assumes two non-exchanging water compartments in tissue water (intra-axonal / extra-axonal), where the intra-axonal part is characterized as zero radius "sticks" (Alexander et al., 2019; Novikov et al., 2019). The model uses the DKI tensor outputs (see (Jespersen et al., 2018; Novikov et al., 2018) for details), which makes the module require a DKI-compatible dataset.

## 3.4 Typical artefacts in diffusion MRI

The EPI-based DWI sequence has some challenges and diffusion-related artefacts which occur typically during an acquisition. In this section, the most important challenges like motion (see section 3.4.1), eddy currents (see section 3.4.2), susceptibility artefacts (see section 3.4.3), as well as noise and rician bias (see section 3.4.4) are presented.

These artefacts of DWI measurements are often corrected during preprocessing before the modelling of the data is performed.

### 3.4.1 Motion

For a full DWI dataset, many diffusion directions have to be acquired (see section 3.2.3 for details), which is typically done via EPI readout approaches (see section 3.2.2 for details). Therefore, the full dataset is strongly sensitive to motion (Andersson and Sotiropoulos, 2016). If, e.g., a subject moves or cardiac pulsation happens during the measurement, this can result in signal loss or/and can be seen as a shift over the single images of the dataset.

This can corrupt the parameter estimation and introduce blurring artefacts. Movement shifts can be corrected before all DWI images are mathematically "merged" into diffusion parameter maps (via, e.g., DTI or DKI).

### 3.4.2 Eddy currents

Due to the diffusion gradients and the rapidly changing gradients during the EPI readout, eddy currents (EC) can be induced in the coils, which can also cause artefacts like geometric distortions (Jezzard et al., 1998; Mohammadi et al., 2013, 2010). The magnitude of the induced additional EC-field $B_z^{EC}$ can be described in a first-order approximation as:

$$B_z^{EC}(\vec{r}) \approx B_z^{EC,0} + \vec{\boldsymbol{r}} \cdot \vec{\boldsymbol{G}}^{EC}, \tag{26}$$

where $\vec{r}$ is the position, $B_z^{EC,0}$ is the homogeneous linear part of the EC field, $\vec{\boldsymbol{G}}^{EC}$ the gradient of the linear part of the EC field, and the time dependence is neglected (Mohammadi et al., 2010).

The EC parameters $B_z^{EC,0}$ and $\vec{\boldsymbol{G}}^{EC}$ can be expressed in the following linear relation:

$$B_z^{EC,0}(\vec{\imath}) = \vec{\boldsymbol{\alpha}}^0 \cdot \vec{\boldsymbol{G}}^D(i) \tag{27}$$

$$G_n^{EC}(\vec{\imath}) = \vec{\boldsymbol{\alpha}}^n \cdot \vec{\boldsymbol{G}}^D(i), \tag{28}$$

with $n = x, y, z$, $\vec{\boldsymbol{G}}^D$ is the diffusion gradient, and $\vec{\boldsymbol{\alpha}}^0$ is the coefficient vector of the homogeneous part of the EC field, $\vec{\boldsymbol{\alpha}}^n$ are the coefficient vectors of the three components of the EC gradient, and $i$ is the index of the diffusion gradient which runs from 1 to the number of diffusion directions (Mohammadi et al., 2010). The complete formalism and derivation of the formulas (26), (27) and (28) can be found in (Mohammadi et al., 2010).

A visualization of the 3D EC distortions is displayed in Figure 9.

| 3d EC distortions | 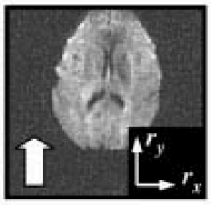 transl. $\Delta r_y(i)$ (*in-plane*) | 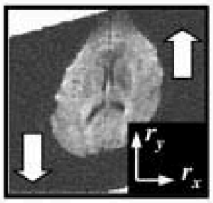 shear. $\kappa_{xy}(i)$ (*in-plane*) | 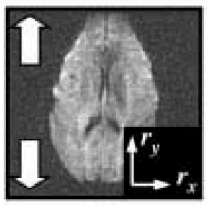 scal. $s_y(i)$ (*in-plane*) | 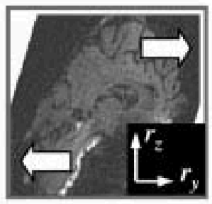 shear. $\kappa_{yz}(i)$ (*through-plane*) |
|---|---|---|---|---|
| *slicewise* | $c\left(B_z^{0,EC}(i)+r_z G_z^{EC}(i)\right)$ | $c\,G_x^{EC}(i)$ | $c\,G_y^{EC}(i)$ | — |
| *whole-brain* | $c\,B_z^{0,EC}(i)$ | $c\,G_x^{EC}(i)$ | $c\,G_y^{EC}(i)$ | $c\,G_z^{EC}(i)$ |

Figure 9: Three *in-plane* EC distortions are corrected by the affine, slicewise registration approach: translation, shearing, scaling. In this *slicewise* representation, the translation parameter depends on the homogenous part of the EC-field and on the z-component of the EC gradient. If the EC distortions as revealed by *whole-brain* registrations are evaluated in three dimensions, a fourth, additional affine deformation (*through-plane* shearing $\kappa_{yz}$) can be related to first-order eddy-current effects, leading to a unique correspondence between EC field components and EC distortions (c is a proportionality constant, involving sequence parameters). Source: Figure and caption reproduced from (Mohammadi et al., 2010). Published online 22 June 2010 in Wiley Online Library (wileyonlinelibrary.com). © 2010 Wiley-Liss, Inc.

A correction of these algorithms can be done, e.g., retrospectively via a model which links the spatial distortions to the EC-field (Haselgrove and Moore, 1996).

For example, established methods are eddy (Andersson and Sotiropoulos, 2016) and ECMOCO (Mohammadi et al., 2015, 2013, 2010), which are also correcting for motion artefacts (section 3.4.1).

### 3.4.3 Susceptibility artefacts

In addition, an EPI sequence can introduce geometric distortions in the acquired data at regions where different tissues (e.g., bones, fat, or cerebrospinal fluid) with different magnetic susceptibilities come together. These susceptibility changes can lead to local inhomogeneities in the magnetic field (Ruthotto et al., 2013, 2012). As mentioned in section

3.1.4, the magnetic field is manipulated for spatial encoding during an MRI session. This encoding assumes a homogeneous magnetic field as a base, and inhomogeneities can therefore lead to spatial distortions as the spatial encoding is corrupted.

To correct this type of artefact retrospectively, an image with the opposite phase encoding direction can be acquired. The images of both phase encoding directions can be combined to estimate the warping field and correct the geometrical distortions by applying the estimated warping field to the DWI dataset. To estimate the field inhomogeneity, the distance functional of both oppositely distorted images $I_1$ and $I_2$ have to be minimized:

$$D[B] = \frac{1}{2}\int_{\Omega} \Big(I_1(x + B(x)v)\big(1 + \partial_v B(x)\big) - I_2(x - B(x)v)\big(1 - \partial_v B(x)\big)\Big)^2 dx, \tag{29}$$

where $B : \Omega \rightarrow \mathbb{R}, where\ \Omega \subset \mathbb{R}^3$ is a field inhomogeneity and $v$ is the unit vector of the phase encoding direction (Ruthotto et al., 2013, 2012).

The unwarping of the images applies two changes. First, the correction of the distortions along the phase encoding direction and second, a correction of the intensities corrupted by the geometrical distortions (Ruthotto et al., 2013).

The field inhomogeneity is estimated by solving:

$$\min_B J\,[B] := D[B] + \alpha S^{diff}[B] + \beta S^{jac}[B], \tag{30}$$

where $S^{diff}$ is a diffusion-, and $S^{jac}$ is a nonlinear regularization term that ensures $-1 < \partial_v \mathrm{B} < 1$, which translates to invertible geometrical transformations and positive intensity modulations (Ruthotto et al., 2013). $\alpha$ and $\beta$ are both > 0 and balance between the regularization functionals and the minimization of the distance (Ruthotto et al., 2013). The complete formalism and derivation of the formulas (29) and (30) can be found in (Ruthotto et al., 2012).

For example, established methods are topup (Smith et al., 2004), or HySCO (Macdonald and Ruthotto, 2018; Ruthotto et al., 2013, 2012).

### 3.4.4 Noise and Rician bias

dMRI datasets have a noise overlay which is higher than for other measurement techniques due to the exponential decay of the diffusion-weighted signal (Stejskal and Tanner, 1965). Noise in dMRI data has a Rician distribution if the acquisition is performed using a single coil receiver (Gudbjartsson and Patz, 1995) and has a noncentral χ-distribution for multiple receiver coils (Aja-Fernández et al., 2014). For example, the signal $S$ of this noncentral χ-distribution with $2L$ degrees of freedom can be described as

$$\frac{S}{\sigma} \sim \chi_{2L}\left(\frac{\zeta}{\sigma}\right), \tag{31}$$

where $L$ is the number of receiver coils, ζ is the true noiseless signal, and σ is the standard deviation of the complex Gaussian distribution of the k-space data (Polzehl and Tabelow, 2016).

If a diffusion signal model is fitted to a DWI dataset that is corrupted with noise out of these distributions, this results in a bias, which is described as the Rician bias and has an impact on the diffusion tensor (Basser and Pajevic, 2000; Gudbjartsson and Patz, 1995; Jones and Basser, 2004), the kurtosis parameters (Veraart et al., 2011, 2013a), and the biophysical modelling parameters (Andersson et al., 2022; Fan et al., 2020; Howard et al., 2022) estimates. The highest impact of this bias is visible in low SNR datasets (Polzehl and Tabelow, 2016), where the noise has a higher proportion to the magnitude intensity.

The EPI sequence uses short echo and fast readout times. This limits the possible measurable SNR. Also, if high $b$ values are acquired, this results in a reduced SNR due to the weaker echo. This can introduce noise to the DWI dataset, which can blur or result in incorrect parameter estimation in addition to the above-mentioned Rician bias.

There are several denoising methods to reduce variance in DWI datasets. For example, established methods are: Local Principal Component Analysis (LPCA) (Manjón et al., 2013), Marchenko-Pastur Principal Component Analysis (MP-PCA) (Veraart et al., 2016), and multi-shell Position-Orientation Adaptive Smoothing (msPOAS) (Becker et al., 2014).

# 4 Concept and development of the ACID Toolbox

This section describes the software and developments for the ACID toolbox. This includes an overview of the architecture and organization of ACID (section 4.1), the benefits of the integration into SPM and MATLAB (section 4.2), how the refactoring was done (section 4.3), the usage of the FAIR principles for ACID (section 4.4), the test system (section 4.5), the implementation of the BIDS standard (section 4.6), and how pipelines can be set up (section 4.7).

## 4.1 Architecture and organization of ACID

The ACID toolbox is fully integrated into the batch system of the Statistical Parametric Mapping (SPM) Software. As an integrated part of it, the functions and modules of ACID can be combined with SPM functions and modules (e.g., for segmentation (Ashburner and Friston, 2005)). Therefore, ACID uses several SPM functions for, e.g., data handling but also uses modified or own functions to enable additional features such as native 4D data handling or generation of BIDS-conform filenames. In addition to the SPM functions and modules, SPM also offers a GUI which is also used by ACID. For a detailed organigram of ACID and its integration into SPM, see Figure 10.

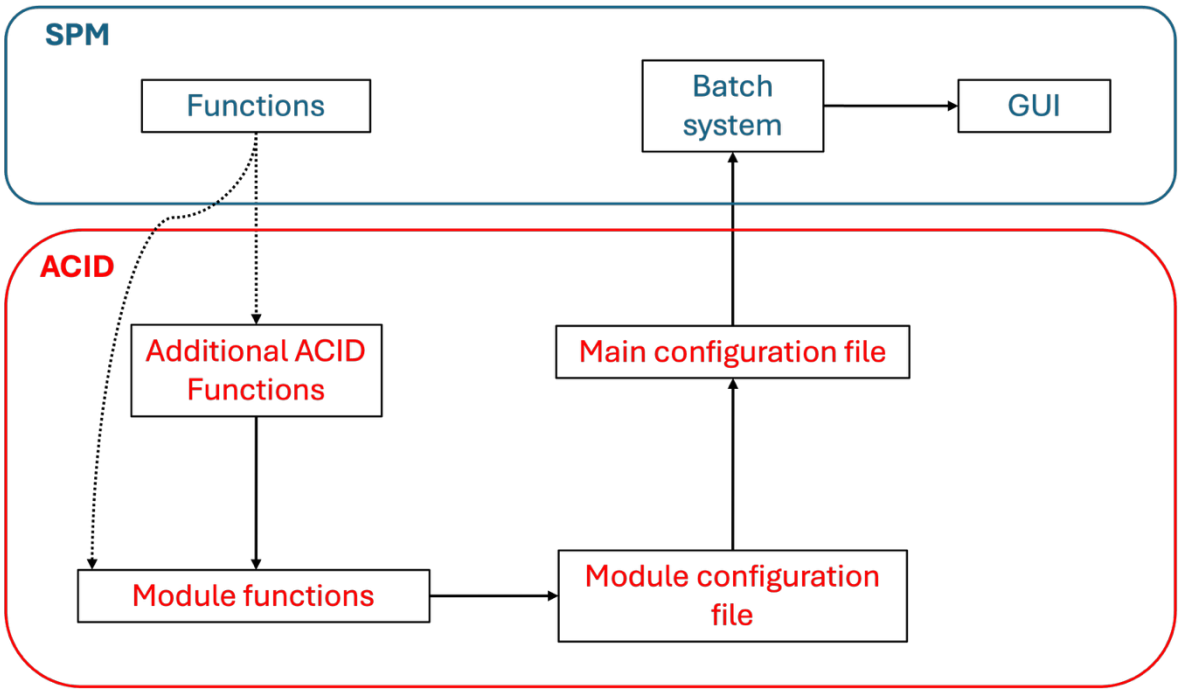


Figure 10: Structure of SPM and the integration of ACID into it visualized via an organigram. The SPM Software provides three parts: The SPM functions, the SPM Batch, and the SPM GUI. The ACID toolbox provides the main configuration file, the module configuration file, the module functions, and additional ACID functions. ACID is integrated into the SPM Batch system via the main configuration file. Every ACID module has its own module configuration file which is named for initialization in the main file. The module configuration file calls the module functions with the in the batch/GUI defined parameters. The module functions are using ACID functions (e.g., for data import) and both have also the possibility to use SPM functions (e.g., spm_coreg for coregistration or spm_vol for import of 3D NIfTI headers). This organization makes it easy to implement new modules (e.g., from external sources), as the module functions only need a few adaptations via ACID functions (e.g., for data handling/naming) and can be linked to a new ACID module configuration file which directly enables an integration into the ACID/SPM batch ecosystem.

The modular organization of ACID and SPM makes it easy to implement new modules and functionalities because the new code files can be added to the existing files, and changes in the existing files are only needed for additions in the main file. This reduces the risk of

damaging existing code and ensures that no error is introduced to the already existing modules.

On the code level, ACID has a main configuration file acid_tbx_cfg.m which is initialized by the SPM batch system. To find the configuration files from external toolboxes, a dedicated toolbox folder exists in the SPM folder structure, in which all configuration main files are identified and initialized. The configuration main file initializes the ACID toolbox, which includes the steps of adding the folder paths of the ACID subfolders to the MATLAB search path and loading all module configuration files. The file also contains the batch syntax for the structure of the modules, which results in the user-selectable drop-down menu and possibility of selecting modules for the "Module List" (see Figure 11, left side). The module configuration files contain the batch structure for each dedicated module (e.g., tbx_cfg_acid_ecmoco.m for ECMOCO) which defines the required inputs for each module and selectable options (see Figure 11, right side). Also, the help instructions for the input parameters are defined on this level (see Figure 11, bottom). The module configuration file calls the module functions (e.g., acid_ecmoco.m for ECMOCO) with the user-defined inputs and starts the module processing. After processing, the module configuration file creates dependencies by saving the locations and parameters (e.g., b-values or processed images) of needed files for following modules in a from the batch system provided structure variable. This whole structure ensures flexibility through modularization and allows the addition of a new module into the batch system by adding a new module configuration file to the main configuration file.

The setup of the modules benefits also from the GUI provided by SPM as all needed parameters are displayed, and additional information can be provided for each parameter (see Figure 11) in one window.

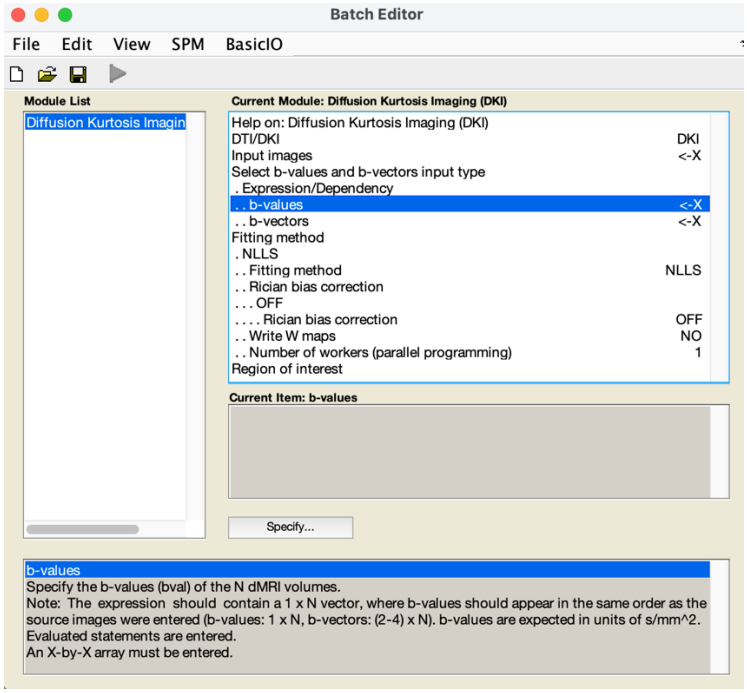


Figure 11: The image shows the SPM Batch Editor with the ACID module Diffusion Kurtosis Imaging (DKI) selected. The mandatory inputs are indicated by "<-X". For the most parameters (e.g., "b-values"), additional information is provided in the lower box.

All ACID modules can work on their own. As it can be seen in Figure 11, e.g., the DKI module shows all required inputs and can be started directly if all inputs are filled in. But the modules can also be combined with additional modules. For example, preprocessing modules can be executed before the model fit is done. This allows users to create pipelines in which the data are computed by the first module of the pipeline and will be directly handed to the next. Figure 12 shows an example in which the results of msPOAS are used for the DKI fit.

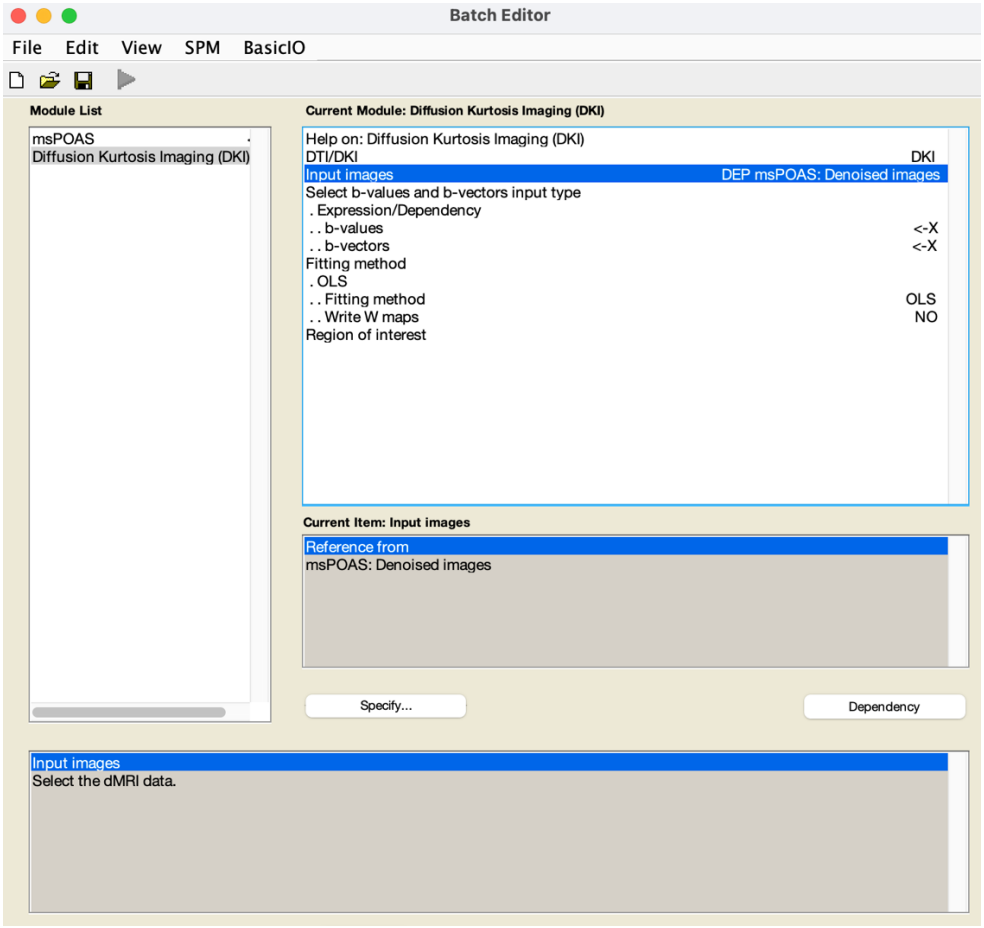


Figure 12 : The image shows the SPM Batch Editor with the ACID modules msPOAS, and Diffusion Kurtosis Imaging (DKI) selected. For the first mandatory input of DKI, "Input images", the dependency "DEP msPOAS: Denoised images" is selected. This has the effect that the denoised output images of msPOAS are handed directly to the DKI module without any user interaction needed.

Also, the combination with modules from other toolboxes (e.g., hMRI toolbox) is possible. SPM also allows the user to save and modify scripts of constructed batches containing one or more modules. This gives the possibility to apply the same batch to different datasets or to modify one or more parameters within a batch for a single analyzed dataset (see Figure 13 for an example script).

```
% List of open inputs
% msPOAS: Input images - cfg_files
% msPOAS: b-values - cfg_entry
% msPOAS: b-vectors - cfg_entry
% msPOAS: Expression/Dependency - cfg_entry
% Diffusion Kurtosis Imaging (DKI): Input images - cfg_files
% Diffusion Kurtosis Imaging (DKI): b-values - cfg_entry
% Diffusion Kurtosis Imaging (DKI): b-vectors - cfg_entry
nrun = X; % enter the number of runs here
jobfile = {'PATH/TO/SCRIPT/example_script_job.m'};
jobs = repmat(jobfile, 1, nrun);
inputs = cell(7, nrun);
for crun = 1:nrun
    inputs{1, crun} = MATLAB_CODE_TO_FILL_INPUT; % msPOAS: Input images - cfg_files
    inputs{2, crun} = MATLAB_CODE_TO_FILL_INPUT; % msPOAS: b-values - cfg_entry
    inputs{3, crun} = MATLAB_CODE_TO_FILL_INPUT; % msPOAS: b-vectors - cfg_entry
    inputs{4, crun} = MATLAB_CODE_TO_FILL_INPUT; % msPOAS: Expression/Dependency - cfg_entry
    inputs{5, crun} = MATLAB_CODE_TO_FILL_INPUT; % Diffusion Kurtosis Imaging (DKI): Input images - cfg_files
    inputs{6, crun} = MATLAB_CODE_TO_FILL_INPUT; % Diffusion Kurtosis Imaging (DKI): b-values - cfg_entry
    inputs{7, crun} = MATLAB_CODE_TO_FILL_INPUT; % Diffusion Kurtosis Imaging (DKI): b-vectors - cfg_entry
end
spm('defaults', 'FMRI');
spm_jobman('run', jobs, inputs{:});
```

Figure 13: Example of a saved batch script. In this script, the modules msPOAS and DKI are executed one after another. The fields “MATLAB_CODE_TO_FILL_INPUT” have to be filled with the corresponding input parameter. This enables the possibility to execute this batch script with different datasets and/or parameters through a “for” loop. If the dependency in Figure 12 would be set before saving the script, the DKI Input “Input Images” would not appear in the saved script as it is internally set.

## 4.2 Benefits of integration into MATLAB and SPM

ACID benefits from the integration into SPM and MATLAB in several ways: MATLAB is a widely used analysis software which is well established in many institutions. It is also available for the three most popular operating systems Windows, Mac, and Linux, which make SPM and ACID independent of the platform used by the user. This also ensures that, for example, a free-of-charge Linux distribution can be used to process data with ACID. For users who have no access to commercial MATLAB licenses, SPM provides the possibility to generate standalone versions. These include ACID if the standalone version is compiled using a SPM version containing ACID. This allows the use of ACID without any costs for

licenses of OS or MATLAB. The only requirement is the MATLAB Runtime, which is freely available[12].

MATLAB also offers general statistical functions and visualization tools which can be used directly in SPM and ACID. This makes further analyses of ACID results easier for the users as they can directly use functions for advanced statistics or visualization.

SPM provides a complete ecosystem containing statistical functions, analysis modules, and a user-friendly GUI. The software is developed for the spatial analysis of structural and functional MRI data and was therefore ideal for the integration of ACID as, e.g., for ACID required file formats for dMRI are the same (NIfTI), and SPM functions can be directly used for the ACID results.

## 4.3 Refactoring of ACID

In this section the refactoring of ACID is explained. This includes a description of the initial state of ACID (section 4.3.1), the conceptual changes through the refactoring (section 4.3.2), the changes on code level (section 4.3.3), the new organization of the file structure (section 4.3.4), the ways ACID guides unexperienced users (section 4.3.5), and how the extraction of metadata is implemented (section 4.3.6).

### 4.3.1 Initial state

The in Figure 10 presented modular organigram structure was not implemented in the initial stage of ACID at the beginning of the PhD project. The initial existing modules were implemented all for their own. They had their own syntax and were designed to work without the use of the SPM batch system (e.g., manual selection or hardcoding of input parameters). Default values were hardcoded, and parts of the code (e.g., data import) were redundant for each module or implemented in different ways (e.g., different functions for the same task or

[12] https://www.mathworks.com/products/compiler/mcr/index.html

different output formats for different modules (3D or 4D NIfTIs)). Also, the naming of output files was not BIDS compliant (prefix instead of module name in "_desc" field) or consistent (e.g., "poas_" for msPOAS and "u" for HySCO). Also, different (and outdated) versions for some modules were included in the folders (e.g., msPOAS versions 2, 3, and 4 as well as the HySCO versions 1 and 2). The functions were not clearly named (e.g., sub-functions of modules did not include the module name) and it was not visible if all existing functions belong to the latest module version or were part of an outdated version. Also, the modular batch structure was not implemented as all module batch configuration code parts were included in the ACID main configuration file which made the code hardly to maintain (2624 lines). The main file contained also several dummy options (which were not used anymore) to load only a part of the tools to the batch system and which would need a change of hardcoded variables in the file. Some modules which were not part of ACID anymore were also implemented in the main file but deactivated via hardcoded dummy variables. Furthermore, the batch dependencies were not working for all modules as the implementation was inconsistent and unnecessarily complicated. For example, a module function creates new files with a specific name, but the name is not directly handed to the dependency. Instead, an additional function loads the files again and reads out the file names which are then handed to the dependency.

In addition, the C files which should enable the possibility to compile own .mex files were too old to be compiled with actual versions of MATLAB.

### 4.3.2 Conceptual changes

To implement a modular organization, the ACID main file was recreated, and all module configuration parts were outsourced to dedicated module configuration files (e.g., tbx_cfg_acid_ecmoco.m for ECMOCO). Also, all unnecessary and outdated code parts were deleted e.g., unused dummy variables or no longer supported deactivated modules). This reduced the number of lines from 2624 to 577. The acid main file contains now only the in

section 4.1 described parts. These changes implemented a modular structure on batch level as now only one line of additional code and an insertion into the batch module list is necessary to integrate a new module config file and therefore a new module into ACID.

The batch configuration for the modules was harmonized by using the same inputs and names for identical parameters (e.g., “b-vectors” instead of “Diffusion Directions”). In order to be compliant with the BIDS standard (see section 4.6 for details) ACID generates 4D NIfTIs for the DWI datasets. To provide an option to handle 3D datasets and convert them into a BIDS usable 4D dataset, a startup module was developed which provides a structured storage for imported 3D/4D NIfTIs as well as for imported or extracted from metadata b-values and b-vectors (see section 5.1 for details).

### 4.3.3 Code changes

To improve the stability of the code, several changes were performed, like fixing code errors, cleaning up the code, and enabling, e.g., error-free dependencies for all modules. Exemplary tasks are presented in section 4.3.1.

Also, the C files were updated, and support now compilation on newer systems (e.g., MacBooks using ARM CPUs).

Multicore support was implemented for ECMOCO to accelerate the processing when the multi-target correction is performed (see section 5.2.1 for details).

To reduce the number of redundancies, also changes on the code level for different functions were performed. For example, the code for Diffusion Tensor Imaging (DTI) and Diffusion Kurtosis Imaging (DKI) was similar in their structure. Additionally, the NLLS algorithm, which can be used in DTI as well as DKI, had its own function with the mostly identical code structure as the DKI function. To solve these redundancies, both diffusion signal models as well as all available fitting algorithms for them were integrated into one file. This results in the creation of only one main function file for model fitting (444 lines) instead of three single function files (DTI: 477 lines, DKI: 421 lines, NLLS: 258 lines). Also, the batch

configuration files were merged into one file. The same was done in combining the ECMOCO versions “Single Target” and “Multi Target” into one config and one function file.

Several functions (e.g., data import) were merged through the development of one function which features all possible use cases for their task. For example, the import function now supports compressed and uncompressed 4D NIfTIs and is integrated and used in all ACID modules. This reduces the amount of maintenance work, as a potential fix in the input function takes effect for all modules using it.

### 4.3.4 File structure

To prepare ACID for further developments, a refactoring of the file structure was done. The aim was that every part of the code and files should be named clearly and structured. This makes the code more robust as it reduces the risk of redundancies and gives a better possibility to solve errors as every part of the code can be found easily. For ACID, the most task to implement this aspect was to rename almost all code files and restructure the folders of ACID. One example of the renaming of the files is shown in Figure 14.

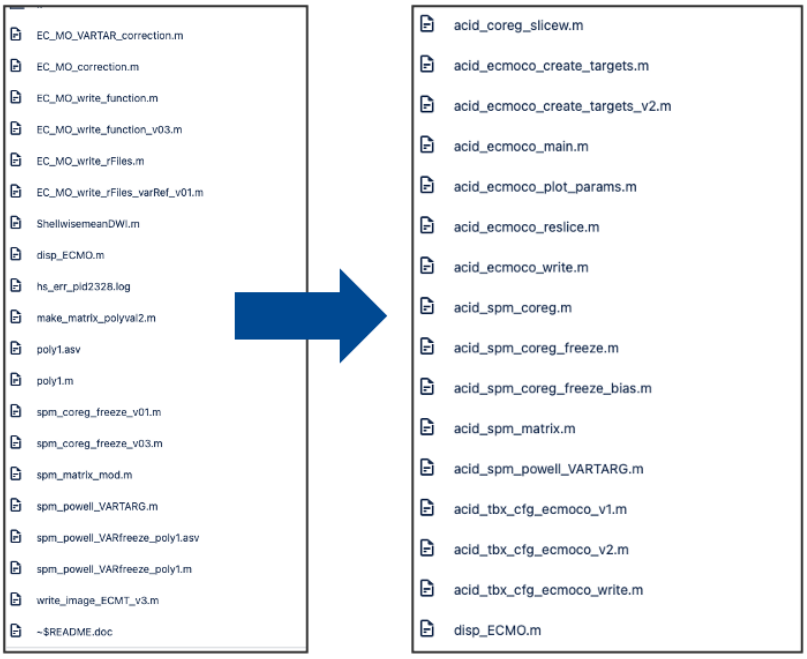


Figure 14: Example of renamed files which are part of the ACID toolbox. In the left panel, the old unstructured filenames are displayed. In the right panel, the renamed files are shown. A structured naming system is implemented based on “acid” as a prefix followed by the module name the file is contributing to (e.g., ecmoco, or tbx_cfg for main files).

### 4.3.5 Guidance for unexperienced users

The goal of ACID is to be usable for unexperienced users. To ensure this, the ACID repository contains a wiki[13] (actual 23 sites) in which the modules and functionalities are described in more detail and instructions for e.g., the standalone version are provided. Furthermore, to reduce the risk of unintended use of ACID, warnings are implemented which appear when basic assumptions of the underlying models are not fulfilled, e.g., a diffusion shell contains less than three diffusion directions, which could make the fitting of the available diffusion signal models to the data bad conditioned.

[13] https://bitbucket.org/siawoosh/acid-artefact-correction-in-diffusion-mri/wiki/Home

### 4.3.6 Extraction of metadata

The ACID toolbox uses NIfTI files which contain not only the acquired image but also metadata. A processing of dMRI data requires the inclusion of metadata information, e.g., b-values or b-vectors. However, these metadata are often not easily accessible and require manual interaction from the user (e.g., for creating b-value/vector matrices in MATLAB), which leads to a risk of mistakes. To solve this, ACID has the possibility to extract automatically b-values and b-vectors from the DICOM header. This reduces the risk of errors compared to manual generation of b-values and b-vectors. Furthermore, in this extraction step, a text file is generated containing the most important acquisition parameters (see Figure 15).

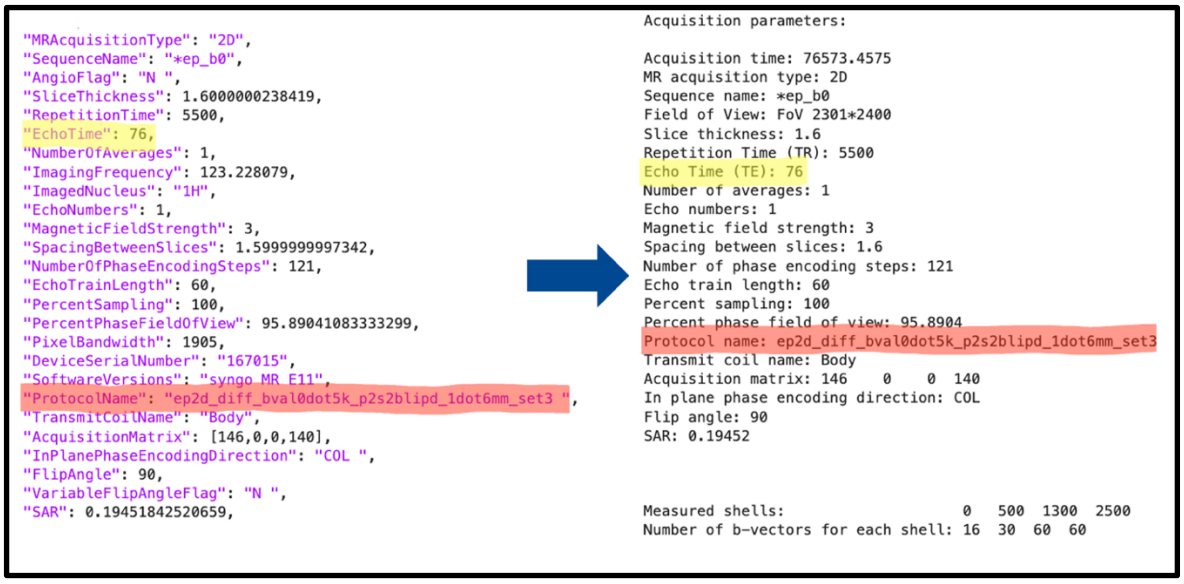


Figure 15: Example of JSON file extraction in ACID. On the left, a part of the JSON file from an example dataset is shown. The parameter fields of Echo Time (TE) (yellow) and protocol name (red) are marked. These are extracted among other values in a dedicated .txt file, which is formatted in a format easy for humans to understand.

This text file provides a documentation of the acquisition parameters and is therefore a good solution for big data analysis, as the documentation of acquisition parameters is done in an automated and structured way. For example, the text file can be used to structure data based

on their imaging parameters such as echo time or repetition time. If in a large study, some of the acquisition protocol parameters varied due to mistakes by the radiographers or due to scanner updates, this is automatically noted by this text file.

## 4.4 FAIR principles in ACID

To develop ACID to a reusable and valuable academic software, the FAIR principles Findable (section 4.4.1), Accessible (section 4.4.2), Interoperable (section 4.4.3), and Reusable (section 4.4.4)) were used. This section gives an overview of how these four principles are used in ACID.

### 4.4.1 Findable

The first aspect of FAIR ensures the findability of software. To fulfill these requirements, ACID has its own website[14] and is located in a git repository[15] containing also a wiki (section 4.3.5). This enables full source control with the possibility to identify each version and change in the code via the git hash number. Furthermore, ACID has a publication which is uniquely identifiable via the DOI number[16].

### 4.4.2 Accessible

The second aspect of FAIR guarantees the availability of the software and code. As git is an open-source and free available code management system, it fulfills the requirements of this FAIR principle. The localization of ACID on a git repository[15] makes the download and update of the toolbox possible in a standardized way (e.g., HTTPS or SSH connections, and git commands). Additionally, the code is fully available through this git located hosting (open source).

---

[14] http://diffusiontools.com/

[15] https://bitbucket.org/siawoosh/acid-artefact-correction-in-diffusion-mri/src/master/

[16] https://doi.org/10.1162/imag_a_00288

### 4.4.3 Interoperable

The third aspect of FAIR is interoperability. This means that the output data of ACID must be usable for other toolboxes and software. Also, the requirements for the input data should be as low as possible, to allow the usage of ACID for as many data sources (e.g., MRI scanner types) as possible. To make the usage of different scanner types for metadata extraction possible, ACID contains a routine to analyze the scanner type and read out the JSON files in the corresponding syntax to the scanner. This is mainly developed and implemented for SIEMENS scanner types (e.g., Siemens PRISMA or different *syngo* MR software types). The structure of the code can easily extend to support additional/new scanner types which provide the needed metadata in JSON files.

For the interoperability of the output files, the BIDS standard is implemented. This ensures that output files are stored in a standardized way and can be used directly in other (BIDS-compliant) tools. In addition, the BIDS standard enables a structured storage for large datasets, which improves the usability for machine learning tools which often require BIDS compliant stored datasets for machine learning analyses (e.g., Clinica). See section 4.6 for details on how the BIDS standard is implemented in ACID.

Furthermore (as mentioned in section 4.2), ACID (as well as SPM) can be used on the most popular operating systems (Windows, Mac, and Linux).

### 4.4.4 Reusable

The last aspect of FAIR is reusability. For this, the code of the ACID toolbox is available open-source. The open-source availability ensures the highest transparency and gives everyone the possibility to control the code, which enhances confidence in the code. Furthermore, this makes it possible to use the complete code for any new project or module.

## 4.5 Test system

ACID contains a test system for the most important processing modules (ECMOCO, msPOAS, HySCO, DTI/DKI, and WMTI-Watson). For a test of a module, a dataset is processed, and the result is compared to a previously generated ground truth. This ensures that the output of a module has not changed due to, e.g., the implementation of new functionalities. Also, it indicates that previously results could be wrong if the test failed after, e.g., conceptual changes or bug fixes.

## 4.6 Implementation of the Brain Imaging Data Structure (BIDS)

ACID uses the Brain Imaging Data Structure (BIDS) (Gorgolewski et al., 2016; Karakuzu et al., 2022) standard on two levels: the folder structure and the file naming.

The results of the several ACID modules are stored in a dedicated "derivatives" folder. Within this folder, each module has its own subfolder (e.g., "ECMOCO" or "msPOAS"). In each subfolder, the output of the corresponding module is stored.

The filename is changed after using an ACID module in a BIDS-compliant way. For this, in the file name, a "_desc" field is added (if it is not existing) and the module name is added behind that. If more than one ACID module is used for the analysis, the module names are concatenated in the desc field (e.g., "_desc-ECMOCO-msPOAS"). To make the identification of the output type BIDS-compliant, a suffix is added for each file containing the name of the data type (e.g., "_dwi" for diffusion-weighted images or "_map" for e.g., DKI-maps). Figure 16 shows an example of the BIDS-compliant output of ACID.

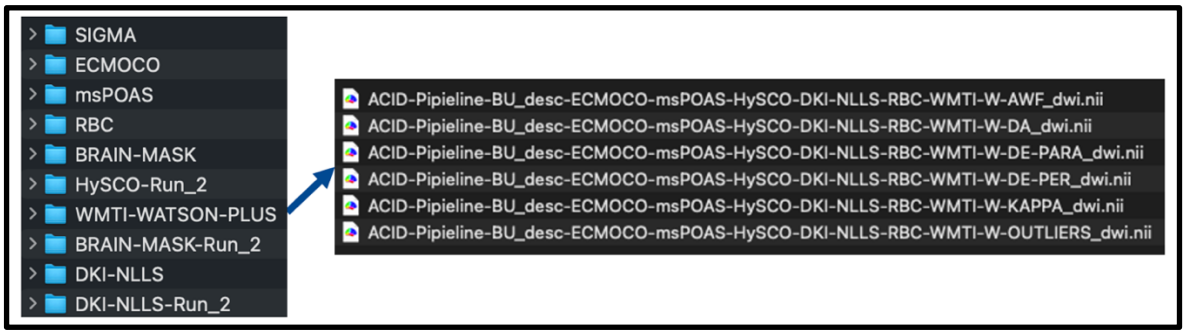


Figure 16: Example of the output structure of ACID. On the left, the folder names are displayed, showing the name for each module that was used in the executed pipeline. If a module is executed again in the same run, a new folder with the extension "-Run_#" is created. On the right side, the content of the "WMTI-WATSON-PLUS" is shown. The "_desc" field in the filename shows all used modules in the executed order. This makes it easier for the user to recognize which modules have been applied to this data and in which order.

## 4.7 Pipeline generation

As described in section 4.1, the modules of ACID can be combined in pipelines via dependencies, enabling the possibility to bring all processing steps (e.g., DICOM to NIfTI conversion, preprocessing, model fitting) into one executable batch script (see section 4.2). This opens up the potential to use ACID for big data analysis where a huge number of datasets must be processed in the same structured way. To give this a higher flexibility and structure, a startup module is integrated in ACID, which offers the option to set up a specific individual output directory if needed or set a specific filename. Also, it is possible to define defaults that ensure optimal usage of the processing steps for dedicated usage (see section 5.1 for details).

# 5 ACID modules

As described in section 4.1 ACID has a modular structure. This section explains all modules of ACID and its functionality. The modules of the ACID toolbox include the startup module (section 5.1), the preprocessing modules (section 5.2), the diffusion signal model fitting modules (section 5.3), biophysical modelling modules (section 5.4), external modules (section 5.5) as well as utility tools (section 5.6). This section is based on the publication (David et al., 2024), published under CC BY 4.0 license.

Many of the in the ACID toolbox used modules have already been published in the scientific dMRI literature (Table 1).

Table 1: Peer-reviewed methods used in the ACID toolbox. Source: Table and caption based on (David et al., 2024), published under CC BY 4.0 license.

| Method | Publication |
|---|---|
| ECMOCO: Eddy-current and motion correction | (Mohammadi et al., 2015, 2013, 2010) |
| HySCO: Susceptibility artifact corrections | (Macdonald and Ruthotto, 2018; Ruthotto et al., 2013, 2012) |
| HySCO: Combine blip-up and blip-down | (Clark et al., 2021) |
| msPOAS: Adaptive denoising | (Becker et al., 2014; Tabelow et al., 2015) |
| RBC: Rician bias correction | (Oeschger et al., 2023a) |
| DTI using robust fitting | (Mohammadi et al., 2013) |
| DKI and axisymmetric DKI using NLLS | (Oeschger et al., 2023a, 2023b) |
| NODDI-DTI | (Edwards et al., 2017) |
| WMTI-Watson | (Oeschger et al., 2023b)* |
| Reliability masking | (David et al., 2017) |

DKI, diffusion kurtosis imaging; DTI, diffusion tensor imaging; NLLS, nonlinear least squares; NODDI, neurite orientation dispersion and density imaging; WMTI, white matter tract integrity. *The ACID implementation is based on the method introduced by (Jespersen et al., 2018).

### 5.1 Startup

MRI scanners normally generate dMRI datasets in DICOM format. This format is not well suited for the use in ACID as every slice of each DWI volume is stored separately. To make the data useable for ACID a conversion to the NIfTI format is required. However, there are several conversion tools which save the data in individual NIfTI formats (3D, 4D or compressed 4D NIfTI) and storage systems (e.g., different folder structures). To enable the handling of these different data storage situations, ACID includes a startup module in which

the user can import the NIfTI files as well as the b-values and b-vectors. The module supports the import of existing 3D/4D NIfTI (also if they are compressed) and b-values/b-vectors as well as the import from 3D NIfTIs with corresponding JSON files (only if they are converted via the SPM DICOM import module). In the second case, the b-values and b-vectors as well as a text file which contains the acquisition parameters (see section 4.3.6 for details) are extracted out of the JSON file.

In addition, the module allows setting up a (BIDS compliant) file name for the output NIfTI file and to set an output directory in which the further processing steps are done. In this directory, the 4D NIfTI file (either directly imported or generated out of selected 3D NIfTIs) as well as the b-values and b-vectors and the parameter text file are stored. The further processing steps are then performed in the derivatives folder at this location. This enables a structured analysis as the raw data, and the derivatives are in one directory unit. If a large number of datasets (big data) is analyzed, each of them has its own folder and derivatives subfolder and can be therefore found easily.

The startup module can also be used to load individual defaults (see section 5.1.1 for details).

### 5.1.1 ACID defaults

The ACID modules have several parameters which have an influence on the performance of the modules. This allows the user to choose optimal parameter settings for each module, which can vary depending on the input data. For example, for the DTI or DKI module, additional outputs (e.g., diffusion tensor, kurtosis tensor) can be activated in the ACID defaults. This can be done in the GUI (e.g., see Figure 11) or, respectively, in the saved batch script (e.g., see Figure 13). However, there are several parameters which are not recommended to change, and which are therefore not displayed in the GUI. Advanced users can change these parameters, if necessary, by modifying the acid_local_defaults.m file. For the changes to become effective, the defaults file has to be loaded via the startup module (see section 5.1). The implementation of the ACID defaults is based on those used in the

hMRI toolbox. This makes it also possible to create individual default files for different datasets which can be loaded then automatically via a batch script in the processing pipeline.

## 5.2 Image preprocessing in ACID

The preprocessing of images is a substantial step in analyzing dMRI data. This section provides an overview of the preprocessing methods implemented. The ACID toolbox corrects different artefacts like motion and eddy currents (see section 5.2.1), noise (see section 5.2.2 and 5.2.3), Rician bias (see section 5.2.4), or susceptibility artefacts (see section 5.2.5).

### 5.2.1 Eddy current and motion correction (ECMOCO)

In ACID, the Eddy Current and MOtion COrrection (ECMOCO (Mohammadi et al., 2010)) method is implemented to correct motion and eddy current artifacts in dMRI datasets. In ECMOCO, two registration types are implemented. A single target mode which registers all images to one specified target image and a multi target mode in which a registration is performed for each diffusion shell to an individual shell target image (see Figure 17).

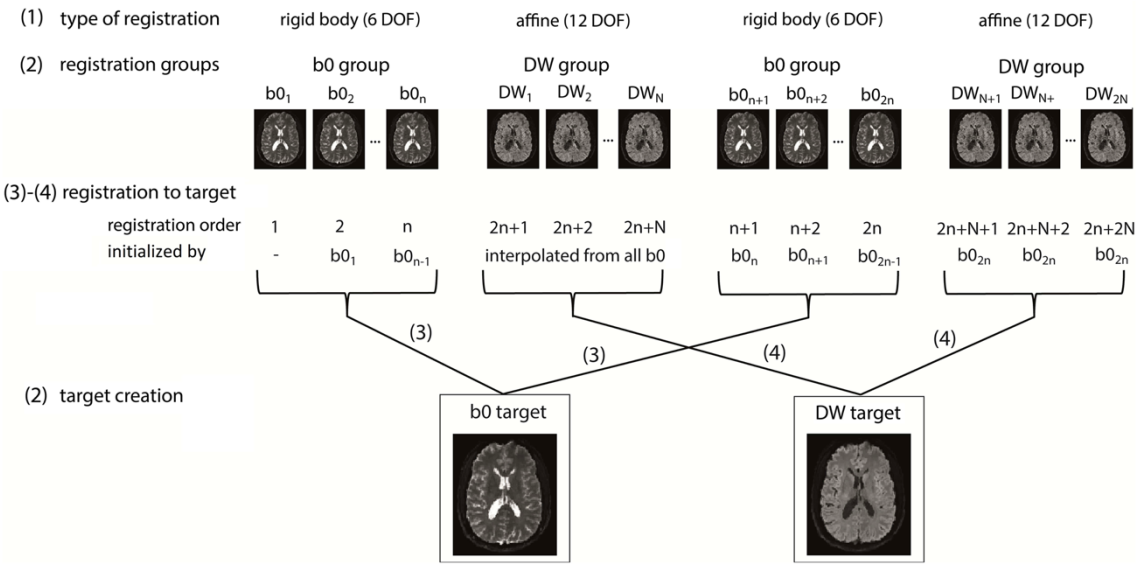


Figure 17: Registration scheme for an example dMRI dataset, which consists of two sets of non-diffusion-weighted (b0) volumes (n volumes each) and two sets of diffusion-

weighted (DW) volumes (N volumes each) interspersed with each other. The b0 and DW volumes form separate registration groups and are registered to their corresponding target volumes. First, the b0 volumes are registered using the rigid-body components of the specified degrees of freedom (DOF), followed by the registration of the DW volumes using all specified DOF. The parameter iteration for a given b0 or DW can be initialized using previously obtained transformation parameters (initialized registration). Source: Figure and caption reproduced from (David et al., 2024), published under CC BY 4.0 license.

The eddy current artefacts are corrected for first-order displacements. The correction is normally performed for the whole volume (3D, "volume wise").

To address the special requirements for spinal cord datasets (e.g., lower number of voxels, low SNR), an initialized registration and exclusion mode is implemented in ACID.

The initialized registration uses the $b_0$ images first to obtain the start parameters for the rigid body registration for the interspersed DW images. This is done by interpolating the rigid-body parameters of the $b_0$ images. These images are used due to their high SNR. This method can improve the correction because slow spatial drifts can be identified, and the rigid body start parameters for low SNR DW volumes are therefore more accurate.

An exclusion option provides the possibility to exclude volumes which are not possible to register due, e.g., artefacts or a too low SNR (see section 5.6.7 for details). These images are corrected with the use of the rigid body parameters of the preceding non-excluded volume.

For spinal cord dMRI datasets, the subject movement is mostly along the rostro-caudal axis (Yiannakas et al., 2012). For this spinal cord specific behavior, ACID has a slice wise (2D) registration mode implemented. This additional correction aligns each slice independently and therefore corrects displacements on a slice level (Mohammadi et al., 2013).

For ex vivo data, no subject movement can be assumed but the presence of eddy currents. To address this behavior, ACID provides an option to correct a dataset only for the effects of eddy currents without performing a rigid body registration.

### 5.2.2 Noise estimation

A correct estimation of the noise standard deviation (σ) is crucial for the proper working of several preprocessing modules like denoising (see section 5.2.3) or Rician bias correction (see section 5.2.4). For this, ACID contains a noise estimation module. Two approaches are integrated in the module:

An approach named "Standard Method" calculating the noise standard deviation based on the formula $\sigma = \sqrt{\sum_{i \in mask} \frac{S_i^2}{2 \cdot L \cdot n}}$, where $S_i$ is the voxel intensity within a background mask defined outside the body, $L$ is the number of voxels within the background mask, and $n$ is the effective number of coil elements that contributed to the measured signal (Constantinides et al., 1997).

The second approach named "Repeated measures method" is based on (Dietrich et al., 2007) and calculates the noise standard deviation in the dimension of repetitions and voxels. The therefore used formula is: $\sigma = mean_{i\ in\ ROI}(std_k(S(i,k)))$, where $S(i,k)$ is the voxel intensity at voxel $i$ in the $k$th repeated image (Dietrich et al., 2007). For this, either the $b_0$ images or the images with the highest b-value ($b_{max}$) can be used for the $k$ dimension (repeated images). The decision should be made based on the analyzed tissue type. For in vivo datasets, a physiological noise has to be assumed and therefore the use of the $b_{max}$ images is recommended. The region should be mostly outside the tissue (no signal, only noise floor) but as next to the image center as possible to avoid an influence of the g-factor on the noise estimation. For brain datasets, the ventricle can be used as an estimation region because both recommendations are fulfilled. ACID creates a ventricle mask automatically within the brain mask creation module (see section 5.6.5 for details). For spinal cord datasets,

cerebro spinal fluid compartments can be used as noise estimation region. For ex vivo datasets, where the absence of physiological noise can be assumed, the recommendation is to use the $b_0$ images and the use of the entire tissue as noise estimation region. To be able to use this option, a measurement of multiple $b_0$ images is required which is has to be considered as it requires possibly the acquisition of additional images. Figure 18 shows example tissues and recommended noise estimation regions for the three discussed tissue types.

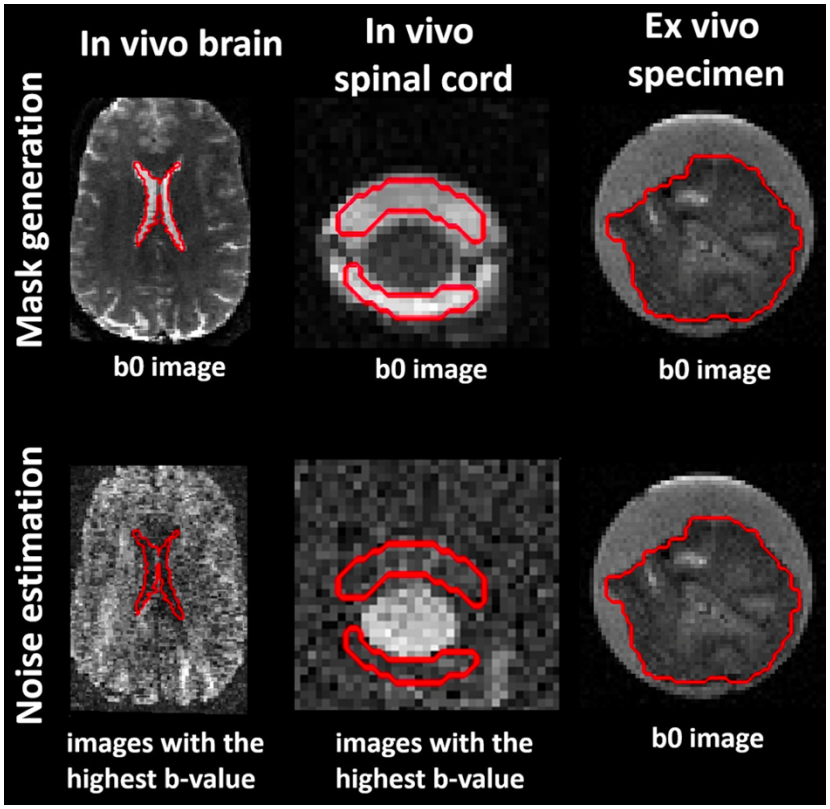


Figure 18: Definition of noise regions of interest (ROI) for the repeated measures noise estimation method. Binary noise ROIs are outlined in red. For in vivo brain and spinal cord dMRI, we recommend creating a noise ROI within the cerebrospinal fluid (CSF), such as the lateral ventricles in the brain and the subarachnoid space in the spinal cord, on the $b_0$ images. Subsequently, we recommend estimating the noise on the images with the highest $b$-value (ideally above 1500 $\frac{s}{\mathrm{mm}^2}$) within the CSF mask. For ex vivo dMRI, the noise ROI is recommended to encompass the specimen itself, but noise estimation should be applied only on the $b_0$ images. Since ex vivo dMRI is not affected by

physiological artifacts, signal variations across the $b_0$ images are considered noise. Source: Figure and modified caption reproduced from (David et al., 2024), published under CC BY 4.0 license.

For the tissue types “In vivo brain”, “In vivo spinal cord” or “Ex vivo specimen”, the recommendation is to use the “repeated measures” method because the “Standard Method” uses a background mask which is usually outside the tissue at the image edges. These regions can be influenced by e.g. ghost artefacts which can corrupt the noise estimation in background regions through their additional ghost signal. It is highly recommended to use the raw dMRI volumes for noise estimation to avoid a corruption of the true noise value through, e.g., interpolations introduced from preprocessing modules.

### 5.2.3 Denoising (msPOAS)

Denoising is necessary for precise diffusion parameter estimation. For this, the multi-shell Position-Orientation Adaptive Smoothing (msPOAS (Becker et al., 2014, 2012; Tabelow et al., 2015)) denoising algorithm is implemented in ACID. The algorithm uses the information provided by the distance in spherical space of the diffusion directions in addition to the information provided by the voxel space. This enables denoising only in homogeneous regions of the dataset, without blurring tissue boundaries. As msPOAS requires only the raw dMRI data, and b-values/vectors as inputs, it is compatible with all diffusion models.

For a correct performance of msPOAS, a precise estimation of the noise ($\sigma$) is necessary (see Section 5.2.2 for details of noise estimation). When the noise estimation is correct, msPOAS should work without any further parameter changes. However, if the denoising result is not sufficient, there are three parameters that can be adjusted. First, the parameter *kstar*, which is the number of iterations performed for denoising. A higher *kstar* results in a stronger denoising/smoothing in areas identified from the algorithm as homogeneous. If the adaptation of the tissue edges is not sufficient, the parameter *lambda* can be adjusted. A lower *lambda* results in a stronger adaptation. Also, the parameter *kappa* can be adjusted

according to the number of diffusion directions, which defines the initial ratio of smoothing between the local space of neighboring voxels and the spherical space of diffusion gradients (Tabelow et al., 2015).

An example of the performance of msPOAS for an example ex vivo dataset is provided in Figure 19.

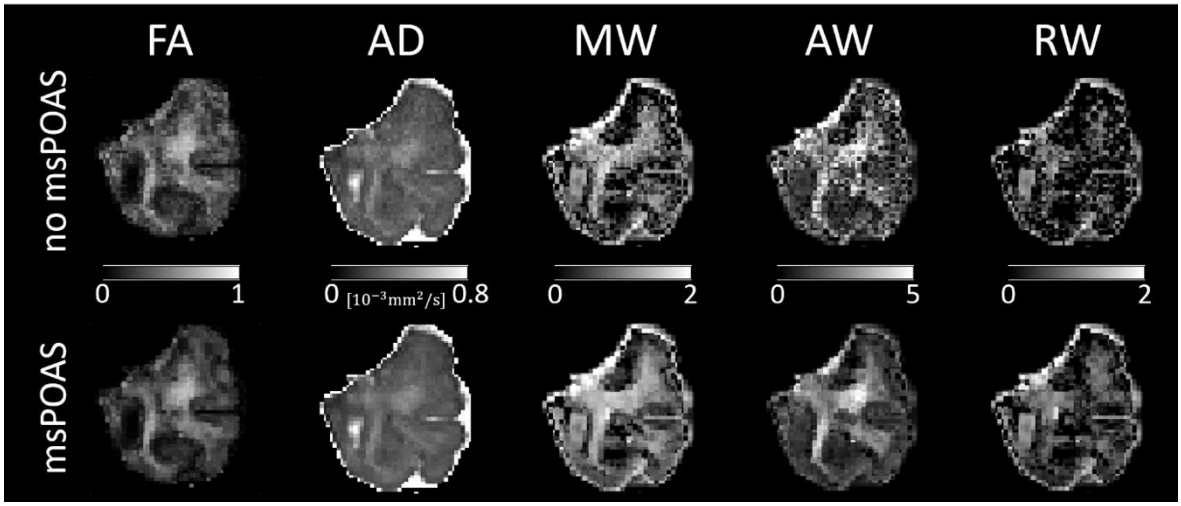


Figure 19: Comparison of maps obtained from fitting the diffusion kurtosis model (ex vivo dataset; refer to Table 2 for details on the dataset), including fractional anisotropy ($FA$), axial diffusivity ($AD$), mean kurtosis tensor ($MW$), axial kurtosis tensor ($AW$), and radial kurtosis tensor ($RW$) with and without applying adaptive denoising (msPOAS). The msPOAS-corrected maps appear less noisy while preserving tissue edges. Source: Figure and caption reproduced from (David et al., 2024), published under CC BY 4.0 license.

### 5.2.4 Rician Bias correction (RBC)

To eliminate the Rician bias in dMRI datasets, two approaches are implemented in ACID. Both methods require an accurate estimation of the noise (σ) (see section 5.2.2 for details). The first approach, named "M2", developed by (Miller and Joseph, 1993), was first applicable only for single receiver coil datasets and later extended to be compatible with multichannel receiver coils (André et al., 2014). The algorithm works on the dMRI dataset providing the measured intensities and uses the estimated noise (σ) for calculating the real voxel intensities by the use of the second moment of the noncentral χ distribution.

The second approach operates on the model fitting level and adjusts the parameter estimation by accounting for the predicted noncentral $\chi$ distribution for the Rican bias (Oeschger et al., 2023a; Polzehl and Tabelow, 2016).

### 5.2.5 Susceptibility-Induced artifact correction (HySCO)

To correct susceptibility artifacts, ACID features the Hyperelastic Susceptibility Artifact COrrection (HySCO) (Ruthotto et al., 2012, 2013; Macdonald and Ruthotto, 2018). To perform this artefact correction, HySCO requires at least one image measured with the reversed phase encoding (blip) direction. This provides two complementary data types named "blip-up" and "blip-down," which can be used in HySCO to estimate a bias field map including the spatial information of the geometric distortions. This map is then applied to the whole dMRI dataset, which results in the correction of the geometric distortions in the outcoming dataset.

When full datasets of both blip directions are acquired, they can be combined additionally via the "HySCO: combine blip-up and blip-down images" module which can provide a more precise susceptibility artifacts correction (Clark et al., 2021).

## 5.3 Diffusion signal models

To estimate diffusion parameters out of a dMRI dataset, ACID has the two most popular mathematical fitting models implemented, which are Diffusion Tensor Imaging (DTI (Basser et al., 1994), section 5.3.1) and Diffusion Kurtosis Imaging (DKI (Hansen et al., 2016; Jensen et al., 2005), section 5.3.2).

### 5.3.1 Diffusion Tensor Imaging (DTI)

Diffusion tensor imaging (DTI) estimates the anisotropic water diffusion in the white matter (Basser et al., 1994). This is done by a diffusion tensor consisting of six independent diffusion parameters. From the eigenvalues of this tensor, the rotationally invariant DTI scalar metrics can be estimated, which are axial ($AD$), radial ($RD$), and mean ($MD$)

diffusivities as well as the fractional anisotropy ($FA$). See Figure 22 for example DTI maps. However, the approach of DTI assumes that the direction of axial diffusivity aligns with the white matter tracts, which is not valid for, e.g., crossing fibers.

There are different model fitting approaches to fit this diffusion tensor. The ACID toolbox features four of them: The ordinary least squares (OLS) (Koay et al., 2006) algorithm minimizes the sum of squares model fit error to obtain the diffusion tensor. The weighted least squares (WLS) algorithm is an extension of the OLS method, adding a weight which takes distortion in the noise distribution in the logarithmic data into account (Basser et al., 1994; Koay et al., 2006; Salvador et al., 2005; Veraart et al., 2013b). The third model fitting algorithm is Robust fitting (Mangin et al., 2002). The method is a similar extension like WLS but categorizes the weights for local and slice-specific artefacts and also for outliers, which can occur especially in spinal cord data (Mohammadi et al., 2013). The in ACID implemented version of robust fitting is based on the "Patching ArTefacts from Cardiac and Head motion" (PATCH) processing method (Zwiers, 2010). A visualization of how the robust fitting algorithm improves the model fit quality is shown in Figure 20.

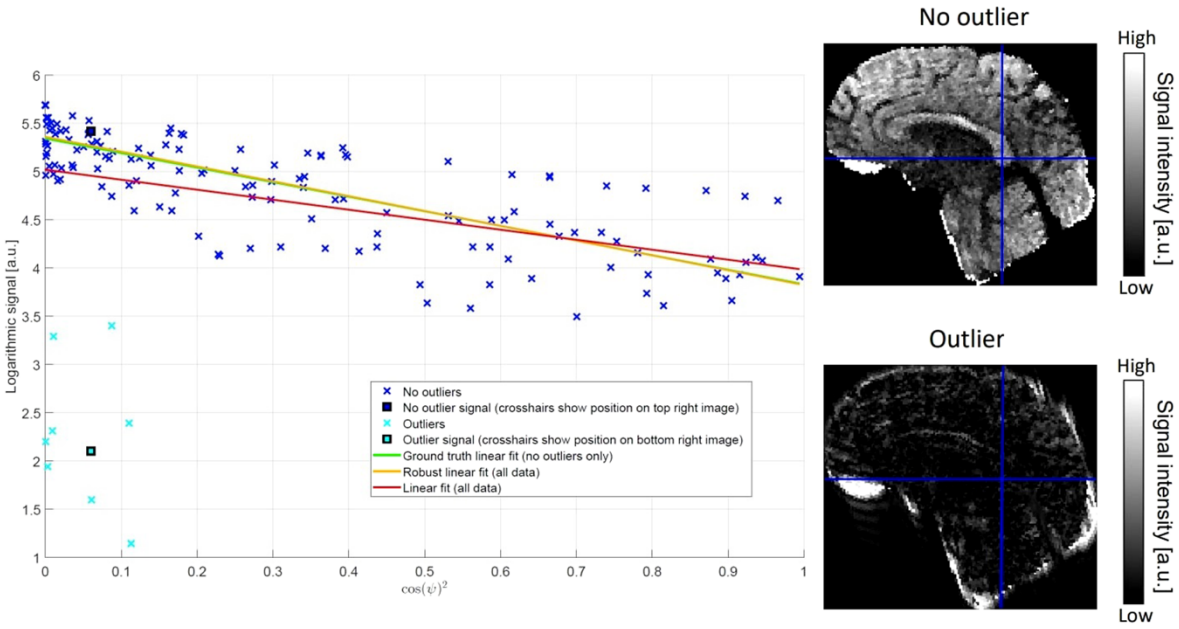


Figure 20: Schematic illustration of how robust fitting down-weights outliers in the model fit. The scatter plot shows the logarithm of diffusion-weighted voxel intensities against

the squared cosine of the angle ψ between the diffusion gradient direction (bvec) and the direction of the first eigenvector in a corpus callosum voxel (see blue crosshairs for location). Blue crosses in the scatter plot indicate data points not affected by artifacts ("No outliers"), while cyan crosses indicate data points affected by strong artifacts ("Outliers"). Outliers were generated by removing the center of the k-space of the original image to illustrate the effect of strong motion artifacts. Two example images corresponding to a nonartifactual ("No outlier," top image) and an artifactual data point ("Outlier," bottom image) are shown on the right. During the model fit, a linear curve is fitted to the logarithmic voxel intensities. The presence of outlier data points leads to a biased model fit (red line) and consequently biased tensor estimates when using ordinary least squares (OLS) model fitting. In contrast, robust fitting down-weights the influence of outliers, leading to a more accurate model fit (orange line) which is closer to the ground truth (green line) obtained by an OLS fit to the nonartifactual data points (blue crosses) only. Source: Figure and caption reproduced from (David et al., 2024), published under CC BY 4.0 license.

Additional to these three linearized models, a nonlinear least squared (NLLS) algorithm based on an implementation (Modersitzki, 2009) of the Gauss-Newton algorithm is implemented in ACID. This method works on the nonlogarithmic data and avoids, therefore, the distortion of the noise distribution.

### 5.3.2 Diffusion Kurtosis Imaging (DKI)

An expansion of DTI is Diffusion Kurtosis Imaging (DKI) (Hansen et al., 2016; Jensen et al., 2005). This approach uses a fourth-order tensor (kurtosis tensor) consisting of 15 independent parameters. This enables the consideration of non-Gaussian water diffusion. DKI allows a more accurate estimation of diffusion parameters as higher shells ($b_{max} > 1000$) can be used. An example of the otherwise (e.g., when a DTI fit is performed) possibly existent kurtosis bias (Edwards et al., 2017) and the reduction through the use of DKI is shown in Figure 21.

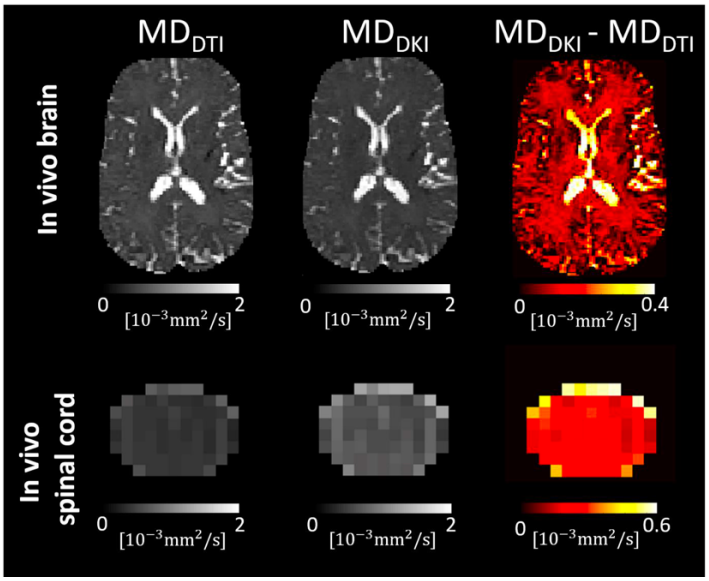


Figure 21: Kurtosis bias in the mean diffusivity ($MD$) maps in an in vivo brain and in vivo spinal cord dataset (refer to Table 2 for details on the dataset). This bias, shown in the right column, refers to the difference in the estimated diffusivity values when using the lower diffusion shells only ($MD_{DTI}$, tensor model, left column) or both the lower and higher diffusion shells ($MD_{DKI}$, kurtosis model, middle column). On average, the kurtosis bias was 12% and 54% within the brain white matter and the whole spinal cord, respectively. Source: Figure and modified caption reproduced from (David et al., 2024), published under CC BY 4.0 license.

The output includes the DTI maps but consists additionally of the axial kurtosis ($AK$), radial kurtosis ($RK$), and mean kurtosis ($MK$). Also, the kurtosis tensor maps ($AW$, $RW$, $MW$) can be computed optionally (Tabesh et al., 2011). See Figure 22 for example DKI maps.

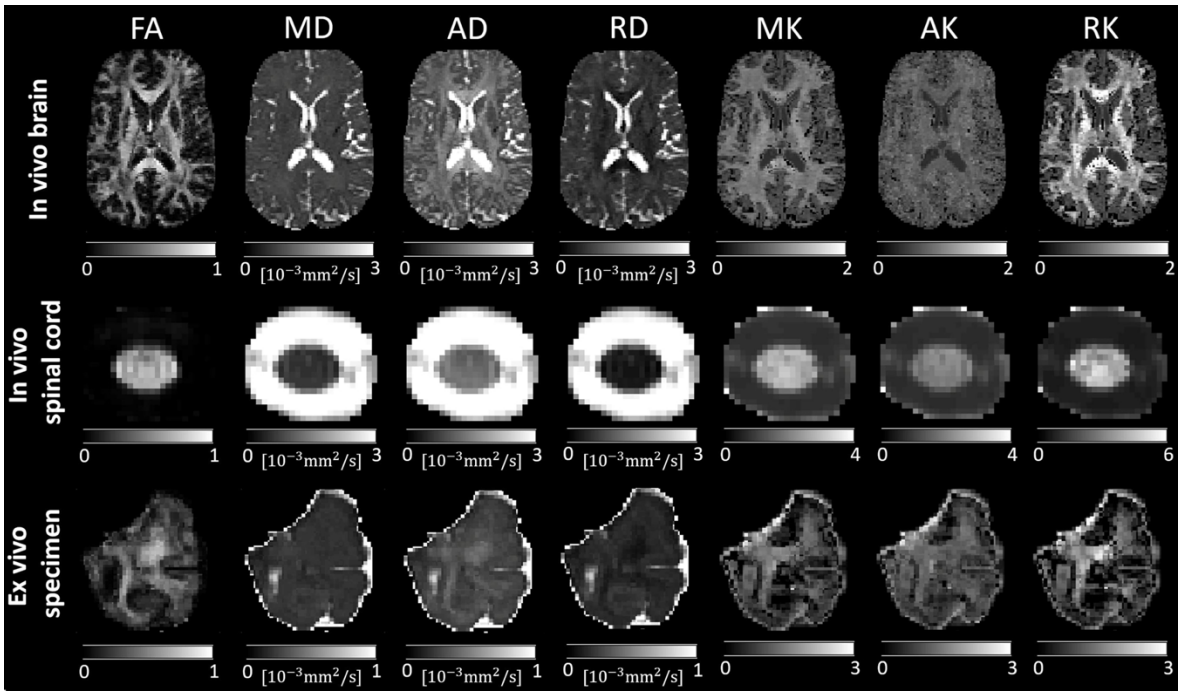


Figure 22: Selected maps derived from diffusion kurtosis imaging (DKI) using an in vivo brain, in vivo spinal cord, and ex vivo dMRI dataset (refer to Table 2 for details on the dataset). Shown are maps of fractional anisotropy ($FA$), mean diffusivity ($MD$), axial diffusivity ($AD$), radial diffusivity ($RD$), mean kurtosis ($MK$), axial kurtosis ($AK$), and radial kurtosis ($RK$). Source: Figure and modified caption reproduced from (David et al., 2024), published under CC BY 4.0 license.

In addition to the DKI model, ACID features the axisymmetric DKI model. This approach uses 8 independent parameters and reduces the number of free parameters compared to DKI (15 parameters) (Hansen et al., 2016).

To perform the model fit, the OLS and NLLS algorithms are implemented for DKI, and the NLLS algorithm for performing an axisymmetric DKI fit (Oeschger et al., 2023b).

## 5.4 Biophysical modeling

In ACID, two biophysical models for white matter are implemented (NODDI-DTI (section 5.4.1) and WMIT-Watson (section 5.4.2).

### 5.4.1 NODDI-DTI

The NODDI-DTI (Edwards et al., 2017) approach implemented in ACID assumes fixed diffusivities ($D_a, D_{iso}$) and neglect CSF volume fractions for white matter. As fixed ex vivo tissue at room temperature has a reduced diffusivity compared to in vivo tissue (Schilling et al., 2025), two different fixed value sets can be selected in the NODDI-DTI module for in vivo ($D_a = 1.7 \cdot 10^{-3}\ \frac{\mathrm{mm}^2}{\mathrm{s}}$, $D_{iso} = 3.0 \cdot 10^{-3}\ \frac{\mathrm{mm}^2}{\mathrm{s}}$) or ex vivo ($D_a = 0.6 \cdot 10^{-3}\ \frac{\mathrm{mm}^2}{\mathrm{s}}$, $D_{iso} = 2.0 \cdot 10^{-3}\ \frac{\mathrm{mm}^2}{\mathrm{s}}$) datasets. For tissues with different diffusivities, the value can be set by the user manually. For example, in (West et al., 2018) a $D_a$ of $0.35 \cdot 10^{-3}\ \frac{\mathrm{mm}^2}{\mathrm{s}}$ and a $D_{iso}$ of $2.0 \cdot 10^{-3}\ \frac{\mathrm{mm}^2}{\mathrm{s}}$ was estimated. In contrast to WMTI-Watson (see section 5.4.2), NODDI-DTI can be used on DTI results (e.g., single shell datasets or if $b_{max} < 1000$). To correct for the kurtosis bias, a correction can be performed for DTI datasets within the module.

The output parameters are the intraneurite ($f$) and extraneurite signal fraction ($1 - f$), the Watson concentration parameter $\kappa$, and the mathematically related anisotropy parameter $p_2$ (Jespersen et al., 2018). For consistency, also the orientation dispersion index ($ODI$) is calculated, which is mathematically related to $\kappa$ (Mollink et al., 2017).

### 5.4.2 WMTI-Watson

The white matter tract integrity (WMTI)-Watson model assumes two no exchanging water compartments (intra- and extra axonal tissue water) (Alexander et al., 2019; Novikov et al., 2019). The outputs created by ACID for WMTI-Watson are the intra-axonal diffusivity ($D_a$), for parallel ($D_{e,par}$) and perpendicular ($D_{e,perp}$) extra-axonal diffusivity. In addition, the axonal water fraction ($f$), the Watson concentration parameter $\kappa$ and, respectively, the mathematically related $ODI$ (Mollink et al., 2017) and anisotropy parameter ($p_2$) (Jespersen et al., 2018) are calculated. See Figure 23 for example WMTI-Watson maps. As WMTI-Watson is based on the Standard Model, the results are degenerated, which results in two

solutions where $D_a < D_{e,par}$ (Plus-Branch) or $D_a > D_{e,par}$ (Minus-Branch). In accordance with the literature (Jelescu et al., 2020; Jespersen et al., 2018), the plus branch is set as the default in ACID as the minus branch is typically the physically invalid solution.

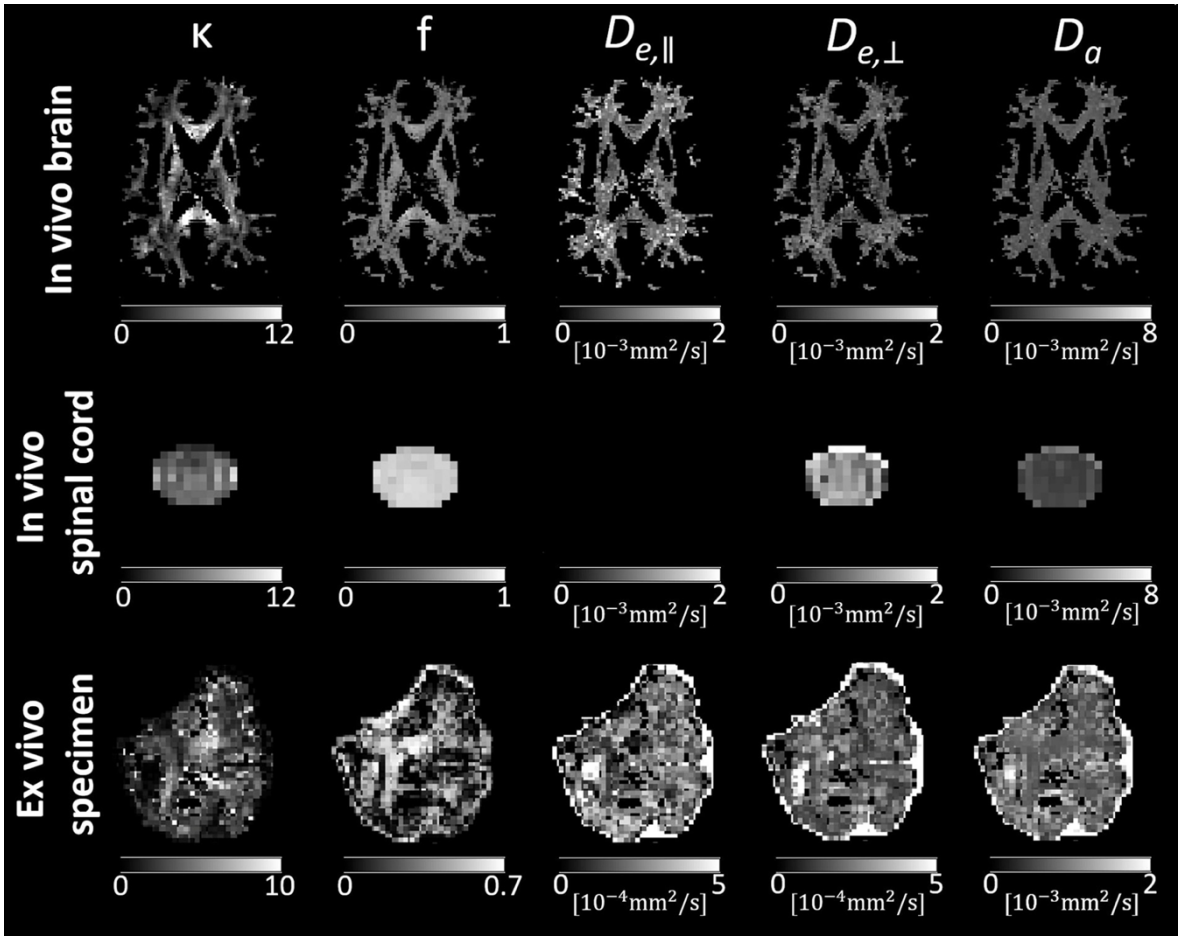


Figure 23: Maps of biophysical parameters derived from the WMTI-Watson model using an in vivo brain, in vivo spinal cord, and ex vivo dMRI dataset (refer to Table 2 for details on the dataset). Shown are maps of Watson concentration parameter ($\kappa$), axonal water fraction ($f$), parallel and perpendicular extra-axonal diffusivities ($D_{e,par}$ and $D_{e,perp}$), and intra-axonal diffusivity ($D_a$). Note that for the in vivo spinal cord dataset, the maximum $b$-value ($b$ = 1500 $\frac{s}{\mathrm{mm}^2}$)) was probably too low for an accurate estimation of $D_{e,par}$, resulting in voxels with negative (hence unphysical) values within the spinal cord. Since WMTI-Watson is a white matter biophysical model, the parameter maps were masked for the white matter in the brain dataset. For the spinal cord and ex vivo specimen, we refrained from masking for the white matter due to the difficulty of obtaining an accurate white

matter mask. Source: Figure and modified caption reproduced from (David et al., 2024), published under CC BY 4.0 license.

## 5.5 External modules

As one of the strengths of ACID is the modularized code structure, external tools can be easily implemented, and several external methods and tools are integrated so far. They are fully integrated in the batch system and therefore use the same GUI, which makes it possible to integrate them in pipelines via dependencies or use them for their own in scripts for processing multiple datasets in one execution step. Actually, several external modules are integrated in ACID. FSL modules: eddy[17] (Andersson and Sotiropoulos, 2016), topup[18] (Smith et al., 2004), applytopup[19], mrdegibbs[20] (implementation of MRtrix) (Kellner et al., 2016), dwidenoise[21] (MPPCA implementation of MRtrix) (Veraart et al., 2016), LPCA denoising[22] (implementation of the DWI Denoising software) (Manjón et al., 2013), Koays Rician bias correction[23] (Koay and Basser, 2006), Real Diffusion Reconstruction[24] (Eichner et al., 2015), SMI[25] (Coelho et al., 2022; Novikov et al., 2018; Reisert et al., 2017), and the wmti[26] (Fieremans et al., 2011) implementation of the DESIGNER toolbox.

---

[17] https://fsl.fmrib.ox.ac.uk/fsl/fslwiki/eddy

[18] https://fsl.fmrib.ox.ac.uk/fsl/fslwiki/topup

[19]https://ftp.nmr.mgh.harvard.edu/pub/dist/freesurfer/tutorial_packages/centos6/fsl_507/doc/wiki/topup(2f)ApplyTopupUsersGuide.html

[20] https://mrtrix.readthedocs.io/en/dev/reference/commands/mrdegibbs.html

[21] https://mrtrix.readthedocs.io/en/dev/dwi_preprocessing/denoising.html

[22] https://sites.google.com/site/pierrickcoupe/softwares/denoising/dwi-denoising/dwi-denoising-software

[23] https://github.com/jan-martin-mri/koays-inversion

[24] https://github.com/cornelius-eichner/real-diffusion

[25] https://github.com/NYU-DiffusionMRI/SMI

[26] https://github.com/NYU-DiffusionMRI/DESIGNER-v1

The modules based on FSL, MRtrix, and DESIGNER require a dedicated installation of the tools on a Unix-based system (e.g., Linux or Mac), as ACID calls the thereby installed functions, which is not possible on Windows-based systems. In addition, it is necessary to start MATLAB within a terminal because only then the environment variables are set correctly, and ACID can call the external required functions.

## 5.6 Utility tools

ACID features several utility tools which offer additional functionalities to improve or simplify the analysis. This includes modules for masking, quality assessment, or manual correction of data.

### 5.6.1 Cropping

To improve the performance of, e.g., motion correction for spinal cord data, it is helpful to crop the image to reduce the fraction of background regions which can lead the motion correction algorithm to wrong results if, e.g., background artifacts are included in the correction.

For this, ACID includes a cropping module. As inputs, the images to be cropped as well as the new matrix size and the voxel coordinate of the new center of the image have to be provided by the user. If no center coordinate is provided, the center can be selected manually via a pop-up window which appears after executing the module in this case. For reproducibility, the cropping parameters are provided as well as the cropped images as outputs.

### 5.6.2 Resampling

For situations where it is necessary to bring two datasets to the same resolution (e.g., voxel-wise analysis), ACID includes a resampling module which allows the user to resample datasets to a desired resolution. The interpolation type can be selected by the user and is the same as defined in spm_slice_vol because the resampling module is based on this function.

The default value is -7, which represents a 7$^{th}$-order sinc interpolation. The sinc order can be selected from 1 to 127 (in the module, the variable has to be selected from -1 to 127). Other interpolation types are nearest neighbor (0), trilinear (1), and high-order Lagrange polynomial (2 to 127).

### 5.6.3 Slice-wise realignment

When performing motion correction for spinal cord, the slice-wise functionality is recommended in ECMOCO (see section 5.2.1 for details). However, a possibility of misalignment of single slices in single volumes can occur. To correct them, ACID offers a slice-wise realignment module in which the user can search for misaligned slices and correct them manually in a GUI framework. The correction for each slice can be done by translation in the x- and y-directions. To visualize the alignment quality, the contour lines of the target image are displayed on the source images.

### 5.6.4 Fusion

The fusion module enables the possibility to merge two images acquired in different regions (e.g., brain, spinal cord). Figure 24 shows an example application. This can be helpful if a warping field is obtained from a structural image acquired with a large field of view containing both merged regions.

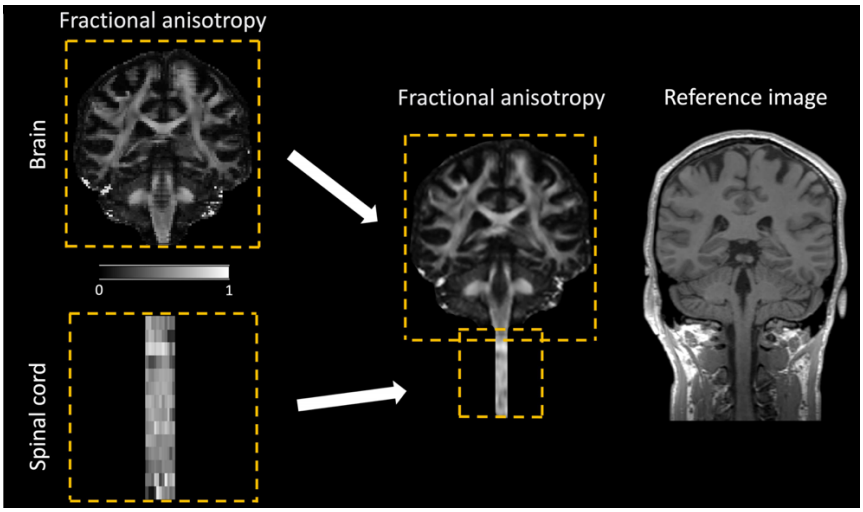


Figure 24: Merging of two fractional anisotropy ($FA$) maps, covering the brain and cervical cord, respectively, into a unified $FA$ map using the Fusion utility function. The two images should ideally share an overlapping region, but they may have different geometric properties such as resolution and number of slices. In the overlapping region, the voxel intensity values are computed as the average of the intensity values from the two images. The merging process requires a structural image as the registration target. The combined $FA$ map is resampled onto the higher resolution structural image, resulting in a smoother appearance. Source: Figure and modified caption reproduced from (David et al., 2024), published under CC BY 4.0 license.

### 5.6.5 Create brain mask

For brain datasets, it is recommended to use a brain mask. This improves the visibility of the results (e.g., parameter maps which only contain the brain and no background). In addition, the computation time can be reduced drastically, as for example, only voxels within the brain are model fitted. The module implemented in ACID uses SPM12's segmentation function (Ashburner and Friston, 2005) and thresholds the tissue probability maps (TPMs) provided by the segmentation. The TPMs of white- and gray-matter as well as CSF are summed up, which results in a binary mask of the entire brain. The threshold for the TPMs can be changed by the user in the defaults.

ACID uses its own TPM template based on the TPM of the hMRI toolbox. The TPM is extended by a ventricle TPM. This allows the automated segmentation of the ventricle and the generation of a binary ventricle mask, which can then be used for noise estimation (see section 5.2.2).

### 5.6.6 Reliability masking

To identify voxels which are irreversible corrupted by, e.g., artefacts, ACID features a reliability masking module. The module uses the root-mean-square model-fit error rms(ε) map (David et al., 2017) which can be estimated by the model fitting modules. Combined with a threshold, a map of unreliable voxels is generated. To estimate the optimal threshold, a submodule named "Determine threshold" is provided. For datasets with many corrupted voxels, e.g., spinal cord datasets, this module can be used to generate a reliability mask which can be used in a region of interest (ROI) analysis as the mask identifies the voxels which contain reliable tensor estimates (David et al., 2017).

### 5.6.7 DWI series browser/movie

For quality assessments, two modules for visual inspection are implemented.

First, a series browser module with which the user can browse through the slices of dMRI data. Slices with artefacts or a too low SNR can be labeled and then skipped in ECMOCO to make the motion correction more stable and based on true signals. This is done by creating a list as output which contains the labeled slice numbers. The list can then be loaded into ECMOCO, and the defined slices are skipped for processing.

Second, to compare multiple datasets, a series movie module is implemented. As inputs, a reference image and up to three dMRI datasets can be loaded in the module. A movie will be created which contains all volumes of the selected datasets.

### 5.6.8 Rician bias simulation module

To estimate the required SNR for a measurement and to decide which RBC method should be used, a Rician bias simulation module is implemented which offers the opportunity to use one of 27 predefined voxels (details are described in (Oeschger et al., 2023a) and the repository[27]) to simulate different SNRs for the selected voxel by contaminating it with noise. This noise-contaminated voxel is then Rician bias corrected (details are described in (Oeschger et al., 2023a)), and the result is compared to the initial voxel without noise as ground truth. This allows an estimation of the performance of the Rician bias methods for different SNRs. As noise contamination is a statistical process, the selected voxel is contaminated multiple times with noise and analyzed to ensure reproducibility.

### 5.6.9 ROI analysis

For ROI-based analysis a ROI analysis, module is integrated. This module offers the calculation of mean and standard deviation for global or subject-specific voxels. Also, a reliability mask (see section 5.6.6 for details on how to generate a reliability mask) can be specified to avoid the influence of corrupted voxels on the calculated metrics.

[27]https://github.com/quantitative-mri-and-in-vivo-histology/axisymmetric_dki_with_rician_bias_correction_simulation_study

# 6 Results

This section shows various examples of the use of ACID. The sections 6.1 to 6.5 provide a demonstration of possibilities ACID features based on three exemplary datasets and were publicized in the ACID toolbox paper (David et al., 2024), published under CC BY 4.0 license. First, the three used datasets are introduced, and the acquisition parameters are presented (section 6.1). In section 0 the processing pipelines for each dataset are presented and discussed. Section 6.3 provides a comparison of NODDI-DTI and WMTI-Watson and gives recommendations which methods should be selected for a specific dataset. The effect of Rician bias correction on biophysical parameters is presented in section 6.4. A comparison of the in ACID implemented denoising methods is shown in section 6.5. The section 6.6 demonstrates how a group analysis in ACID can be performed and how the processed data would be stored BIDS compliant. Furthermore, a comparison of different biophysical modelling methods is investigated.

## 6.1 Experimental datasets (in vivo Brain, in vivo Spinal Cord, ex vivo Specimen)

The ACID modules depend on specific parameters. The optimal choice depends on the acquired dataset (e.g., tissue type). ACID has pre-defined optimal settings for the tissue types of in vivo brain, in vivo spinal cord, and ex vivo specimen.

For a demonstration of the performance of ACID, datasets of the three mentioned tissue types were used and processed. Table 2 shows the acquisition parameters of the three datasets. The distribution of the diffusion directions ($b$-vectors) for the MRI acquisition were defined using the configuration proposed in (Caruyer et al., 2013)[28].

[28] http://www.emmanuelcaruyer.com/q-space-sampling.php

Table 2: Scan parameters of the in vivo brain, in vivo spinal cord, and ex vivo dMRI datasets. Source: Table and caption based on (David et al., 2024), published under CC BY 4.0 license.

| **Dataset** | **In vivo brain** | **In vivo spinal cord** | **Ex vivo specimen** |
|---|---|---|---|
| *Imaged body part or tissue* | entire brain (including cerebellum) of a 34-year-old healthy volunteer | upper cervical cord (appr. C1-C4) of a 43-year-old healthy volunteer | ex vivo specimen of the temporal lobe from a 46-year-old patient diagnosed with drug-resistant temporal lobe epilepsy; specimen embedded in glucose for 2 h and fixed with 4% paraformaldehyde for 12 h before measurement |
| *Scanner* | 3T Siemens Prisma Fit | 3T Siemens Prisma Fit | 3T Siemens Prisma Fit |
| *Receive coils* | 64-channel Head/Neck | 64-channel Head/Neck | 16-channel Hand/Wrist |
| *Sequence* | 2D single-shot spin-echo EPI | 2D single-shot spin-echo EPI | pulse gradient spin echo |
| *Volumes and b-values [s/mm$^2$] (number of gradient directions)* | b = 0 (18); b = 600 (30); b = 1100 (45); b = 2500 (60) | b = 0 (11); b = 500 (30); b = 1000 (30); b = 1500 (30) | b = 0 (36); b = 550 (30); b = 1100 (75); b = 2200 (45); b = 2500 (60); b = 5000 (60) |
| *Cardiac gating* | -- | 2 slices per cardiac cycle, trigger delay of 260 ms | - |
| *Number of slices* | 100 (interleaved, no gap) | 14 (interleaved, no gap) | 160 |
| *Resolution [mm$^3$]* | 1.7 x 1.7 x 1.7 | 1.0 x 1.0 x 5.0 | 0.8 x 0.8 x 0.8 |
| *Field of view [mm$^3$]* | 204 x 170 x 201 | 128 x 36 x 70 | 128 x 48 x 48 |
| *Echo time* | 75 ms | 73 ms | 99 ms |
| *Repetition time* | 5800 ms | pulse-dependent (cardiac gated) | 8700 ms |
| *Parallel imaging* | 2x (GRAPPA) | - | - |
| *Multi-band imaging* | - | - | - |
| *Phase partial Fourier* | 7/8 | - | 7/8 |
| *Phase-encoding dir.* | A-P | A-P | A-P |
| *Readout bandwidth* | 1842 Hz/pixel | 1396 Hz/pixel | 802 Hz/pixel |
| *EPI spacing* | 0.77 ms | 0.93 ms | 1.37 ms |
| *EPI factor* | 120 | 36 | 60 |
| *Acquisition time [min:sec]* | 17:46 | 06:51 (nominal) | 93:10 |
| *Additional data with reversed phase-encoding direction* | a single b0 volume acquired with reversed phase-encoding direction | full blip-reversed acquisition (reversed phase-encoding available for each volume) | full blip-reversed acquisition (reversed phase-encoding available for each volume) |

## 6.2 Application of the ACID Toolbox on three datasets

Figure 25 visualizes the capabilities and expectable results for three exemplary datasets which represent the three tissue types for which ACID offers dedicated processing options (in vivo brain, in vivo spinal cord, and ex vivo specimen). The pipeline for each tissue type has a similar structure, but the settings differ for several processing steps.

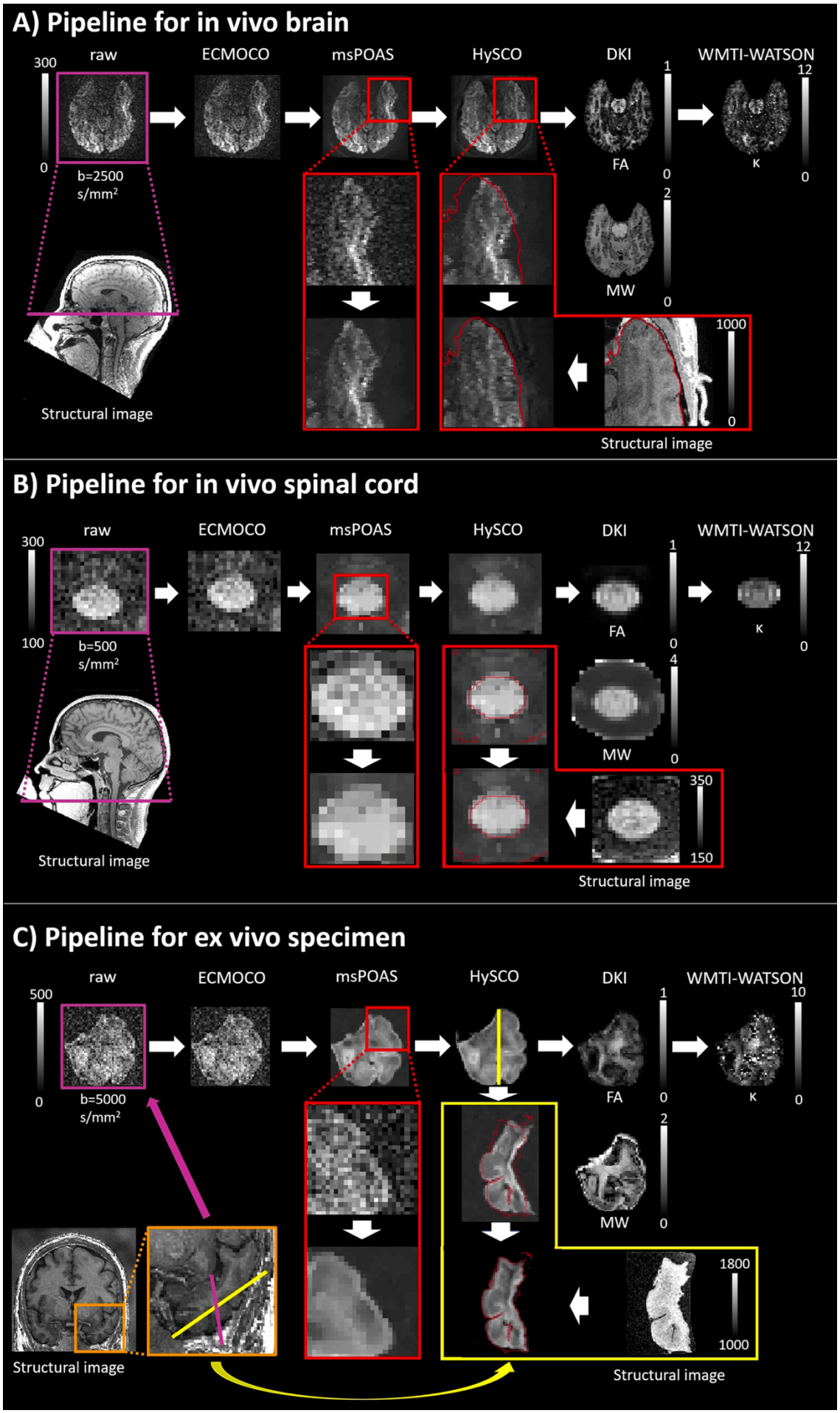
A) Pipeline for in vivo brain
raw
ECMOCO
msPOAS
HySCO
DKI
WMTI-WATSON
300
0
b=2500 s/mm²
FA
1
0
K
12
0
MW
2
0
1000
0
Structural image
Structural image
B) Pipeline for in vivo spinal cord
raw
ECMOCO
msPOAS
HySCO
DKI
WMTI-WATSON
300
100
b=500 s/mm²
FA
1
0
K
12
0
MW
4
0
350
150
Structural image
Structural image
C) Pipeline for ex vivo specimen
raw
ECMOCO
msPOAS
HySCO
DKI
WMTI-WATSON
500
0
b=5000 s/mm²
FA
1
0
K
10
0
MW
2
0
1800
1000
Structural image
Structural image

Figure 25: Standard processing pipelines for typical (A) in vivo brain, (B) in vivo spinal cord, and (C) ex vivo dMRI datasets (refer to Table 2 for details on the datasets and Table 3 for details on the pipeline settings). Example batches for each type of dMRI data are stored in the Example_Batches folder of the toolbox. The positions of the displayed slices of the dMRI data are indicated in purple on the corresponding structural images. For the ex vivo specimen (C), the brain region from which the sample was extracted is highlighted in an orange box. Although not explicitly shown here, noise estimation should be performed on the unprocessed data (see Appendix C), which serves as input for msPOAS, Rician bias correction, and diffusion tensor fitting (for fitting methods WLS and robust fitting). However, in case of substantial misalignments across volumes, and when using the repeated measures noise estimation method, it might be beneficial to perform this step after ECMOCO to prevent an overestimation of noise. For msPOAS, a zoomed-in visual comparison is shown between a diffusion-weighted (DW) image before (middle row) and after applying msPOAS (bottom row); the msPOAS-corrected image appears less noisy while preserving tissue edges. For HySCO, contour lines of the corresponding structural image (displayed as red lines) are overlaid on a zoomed-in DW image both before (middle row) and after applying HySCO (bottom row). HySCO improves the alignment between the DW and the structural image. For the in vivo brain dMRI dataset (A), an inferior slice is shown that presents high susceptibility-related distortions, making the effect of HySCO more visible. For the ex vivo dMRI dataset (C), the effect of HySCO is shown in a slice (illustrated in yellow) orthogonal to the original one (illustrated in purple) to better visualize susceptibility-related distortions and their correction. Note that HySCO is applied as the final preprocessing step, that is, after applying msPOAS; however, the HySCO field map used for “unwarping” the diffusion-weighted images is estimated on the ECMOCO-corrected datasets, that is, before applying msPOAS. Rician bias correction (not explicitly shown here) should be applied either before (recommended: between msPOAS and HySCO, using the RBC module) or during model fitting (using the Rician bias correction option in NLLS). Diffusion signal models are fitted on the processed dataset; here, we display the maps of fractional

anisotropy ($FA$) and mean kurtosis tensor ($MW$) from diffusion kurtosis imaging (DKI). The output from DKI can be used to compute biophysical parameters of the white matter; shown here is the map of Watson concentration parameter ($\kappa$) from the WMTI-Watson biophysical model. Note that for the in vivo brain dMRI dataset, the inferior slice displayed contains relatively little white matter; hence, we refrained from using a white matter mask. The less smooth appearance of the κ map is due to the low values in the gray matter. Source: Figure and modified caption reproduced from (David et al., 2024), published under CC BY 4.0 license.

The tissue type-specific individual settings are listed in Table 3.

Table 3: Settings of selected modules for in vivo brain, in vivo spinal cord, and ex vivo dMRI datasets. Source: Figure and caption reproduced from (David et al., 2024), published under CC BY 4.0 license.

| Module | Adjustable parameter | In vivo brain dMRI | In vivo spinal cord dMRI | Ex vivo dMRI |
|---|---|---|---|---|
| **ECMOCO** | *type of registration degrees of freedom* | volume-wise<br>9 [transl. x, y, z ; rotation x, y, z ; scaling y; shearing x-y, y-z] | volume- and slice-wise<br>*volume-wise*: 4 [transl. x, y, z; scaling y]<br>*slice-wise*: 3 per slice [transl. x, y; scaling y] | volume-wise<br>4 [transl. y; scaling y; shearing x-y, y-z] |
| | *mask* | - | mask around the spinal cord | - |
| **msPOAS** | *kappa* | automatically determined | increase default for low SNR data (e.g., +20%) | automatically determined |
| **RBC** | | defaults | defaults | defaults |
| **HySCO** | | defaults | defaults | defaults |
| **DTI** | *Fitting algorithm* | robust fitting or NLLS | robust fitting or NLLS | NLLS |
| **DKI/axDKI** | *Fitting algorithm* | NLLS | NLLS | NLLS |
| **NODDI-DTI** | *Fixed diffusivities* | In vivo parameters | In vivo parameters | Ex vivo parameters |
| **WMTI-Watson** | | defaults | defaults | defaults |

In this section, the preprocessing steps (Motion- and Eddy Current Correction in section 6.2.1, denoising in section 6.2.2, and susceptibility artefact correction in section 6.2.3), the physical diffusion models (section 6.2.4), and the application to biophysical diffusion models (section 6.2.5) are explained.

### 6.2.1 Preprocessing I: Motion- and eddy current correction

The motion- and eddy current correction are performed for all tissue types as the first step because the following modules like msPOAS or HySCO assume the absence of, e.g., motion artefacts. For this the ACID module ECMOCO can be used (see section 5.2.1 for details) The type of motion that can be assumed is different for each tissue type:

For in vivo brain datasets, the motion is possible in 6 different directions (translation and rotation along $x$-, $y$-, $z$-direction). In addition, eddy currents, which occur often during the measurement, can be corrected by ACID using a first-order approximation. This is performed as a translation and scaling along the phase-encoding direction as well as in-plane and through-plane shearing (Mohammadi et al., 2010). Therefore, 9 degrees of freedom are recommended (the translation along the phase-encoding direction for eddy currents correction is the same degree of freedom for the algorithm as for the translation correction). For spinal cord datasets, ACID features an additional slice-wise correction in which the correction is performed on a 2D (slice) level. This improves the correction of artefacts occurring from e.g., cardiac pulsation which are not sufficiently corrected via a volume-wise correction (Mohammadi et al., 2013). Due to the smaller field of view and the location next to the scanner isocenter, eddy-current artifacts are less strong compared to brain datasets. Therefore, the first-order approximation for correction of eddy currents, that ACID features, is generally sufficient. The recommendation is therefore to perform a volume-wise correction with four degrees of freedom ($x$-, $y$-, $z$-translation and scaling in y-direction) to correct displacements of the whole spine through e.g., subject movement followed by a slice-wise correction with 3 degrees of freedom ($x$-, $y$-translation and scaling in $y$-direction). The combined correction techniques result in a higher SNR as well as in a better test-retest variability in DTI maps (Mohammadi et al., 2013). Other degrees of freedom like shearing or rotation can be omitted as the expected misalignment is very small. The correction of these artefacts leads to the risk of overcompensation and a less accurate result compared to

no correction. As the structures around the spinal cord (e.g., bones) are also often part of the DWI image and have a different motion profile, it is recommended to use a mask defining the spinal cord region which is then only used to estimate the motion correction parameter. To ensure that the correction of slice-wise motion artefacts is sufficient, the slice-wise realignment module (see section 5.6.3) can be used to check and, if necessary, correct displacements manually.

For ex vivo datasets, subject movement can be neglected if the specimen is spatially fixed (e.g., paraffin embedded (Absinta et al., 2014)). As a result of this approach, only the eddy currents are recommended to be corrected along the phase encoding direction (in most cases the y-direction (y-scaling/translation and $x$-$y$- and $z$-$y$-shearing)). Similar to spinal cord datasets, the first-order correction of eddy currents is sufficient for small specimens which are next to the scanner isocenter.

### 6.2.2 Preprocessing II: Denoising and RBC correction

For the denoising performed by msPOAS (see section 5.2.3 for details), no special tissue-related settings are needed to be set. However, the denoising is a crucial step for the estimation of accurate DTI/DKI parameter maps (see Figure 19 for an example of ex vivo parameter maps). The default settings can be used for in vivo brain/spinal cord as well as ex vivo datasets. If the SNR of the dataset is generally high, denoising can lead to an additional error and can be omitted in this case (see section 6.5 for details). In low SNR situations, the denoising results could be insufficient due to still existing noise in the denoised data. In this case, the parameter kappa can be increased manually for a stronger denoising. In addition, Rician Bias correction (RBC) is recommended for low-SNR datasets (see section 6.4 for an example demonstration). ACID features two implemented RBC approaches (see section 5.2.4 for details). The required noise value can be estimated via the noise estimation module (see section 5.2.2 for details).

### 6.2.3 Preprocessing III: Susceptibility artefact correction

The correction of susceptibility artefacts is recommended for datasets acquired via, e.g., multiband EPI sequences or when a structural image needs to be combined with an acquired EPI image (e.g., the dMRI axonal water fraction parameter map and the magnetization transfer saturation maps can be used for g-ratio mapping (Mohammadi and Callaghan, 2021)). For this, HySCO (see section 5.2.5 for details) can be used in ACID as it is demonstrated for the three exemplary datasets in Figure 25. HySCO uses two images with different phase encoding directions and assumes them as registered. Therefore, it is recommended to acquire both images in close successive order. The default settings should provide sufficient results for all three tissue types.

### 6.2.4 Physical diffusion models

ACID includes the two physical diffusion models DTI (see section 5.3.1 for details) and DKI (see section 5.3.2 for details). The selection of the recommended approach depends normally on the acquired b-values. For both models, several fitting algorithms are implemented. In general, the NLLS algorithm is recommended for each tissue type if the acquired SNR is sufficiently high (see (Oeschger et al., 2023a) for the recommended minimum SNR).

For DTI datasets, such as spinal cord datasets where high b-values are challenging to be measured for DKI analyses and often lack a significant number of outliers, the robust fitting algorithm is recommended. This algorithm downweights voxels identified as outliers, thereby enhancing the robustness of the diffusion model fit. A visualized example of this is provided in Figure 20.

For situations where the SNR is low and the number of outliers is high, msPOAS and RBC can reach their limits, and in this situation, the use of reliability masking (see section 5.6.6 for details) might be useful to extract the reliable voxels out of the dataset (David et al., 2017).

It is also recommended to use a mask (e.g., by using the create brain mask module (section 5.6.5)) as well as the multicore option, if possible, to reduce the computation time.

### 6.2.5 Biophysical diffusion models

The selection of most precise biophysical diffusion model for a given dataset depends on several characteristics. If a multi-shell dataset was performed and the b-values are high enough to perform a DKI fit, the WMTI-Watson approach is recommended as the number of assumptions is lower compared to NODDI-DTI (e.g., no fixed diffusivities) and therefore the algorithm has more flexibility in fitting the biophysical parameter out of the DKI parameter maps. However, the higher flexibility and lower number of assumptions increase the need for a proper estimation of the diffusion parameters via DKI. This can be difficult to achieve for e.g., spinal cord datasets where the SNR is typically lower, especially for higher diffusion shells which are needed for DKI. In this case, the NODDI-DTI approach could provide better results as it requires a DTI fit and therefore lower acquired b-values. But this approach can lead to additional problems as the in NODDI-DTI assumed fixed diffusivities are estimated for brain datasets. Therefore, they might not be valid for e.g., spinal cord datasets and require manual adjustment or investigation to estimate proper values. For ex vivo datasets where e.g., diffusivity in white matter is described in literature as 85% lower compared to in vivo (Roebroeck et al., 2019), a dedicated fixed diffusivity set can be selected in ACID providing these values.

Also, due to the DTI fit, a kurtosis bias could be introduced, which could corrupt the parameter estimation, e.g., for the MD map, and result in not realistic values which are not usable for NODDI-DTI estimations (see Figure 21 for an example).

An analysis demonstrating the performance of WMTI-Watson compared to NODDI-DTI is shown in section 6.3, and an analysis of the impact of Rician bias correction on biophysical parameter estimation for WMTI-Watson and NODDI-DTI is shown in section 6.4.

A third option is the as external tool integrated white matter tract integrity (WMTI) model, which assumes highly aligned fibers (idealized as infinitely long cylinders) but has no fixed diffusivity assumptions (Fieremans et al., 2011).

## 6.3 Comparison of NODDI-DTI and WMTI-Watson

For a comparison of ACIDs implemented biophysical parameter estimation methods, the Watson concentration parameter ($\kappa$) and axonal water fraction ($AWF$) were estimated for the exemplary brain and spinal cord dMRI datasets (see section 6.1 for details). As discussed in section 6.2.5, the selection of the best biophysical estimation method can be different depending on the given dataset and data quality. To show that the choice of the most precise biophysical model can depend on the acquired dataset, both parameters were estimated via NODDI-DTI and WMTI-Watson (see Figure 26). For the brain dataset, both estimated values were more consistent with the literature values if they were estimated via WMTI-Watson. In contrast, for the spinal cord dataset, the via WMTI-Watson estimated parameters were highly overestimated, and for NODDI-DTI only $\kappa$ could be estimated but within correspondence to the literature values.

The numerical values of the estimated parameters and literature values can be found in the figure caption of Figure 26, and the reasons for the different results of the biophysical modules are discussed in section 6.2.5.

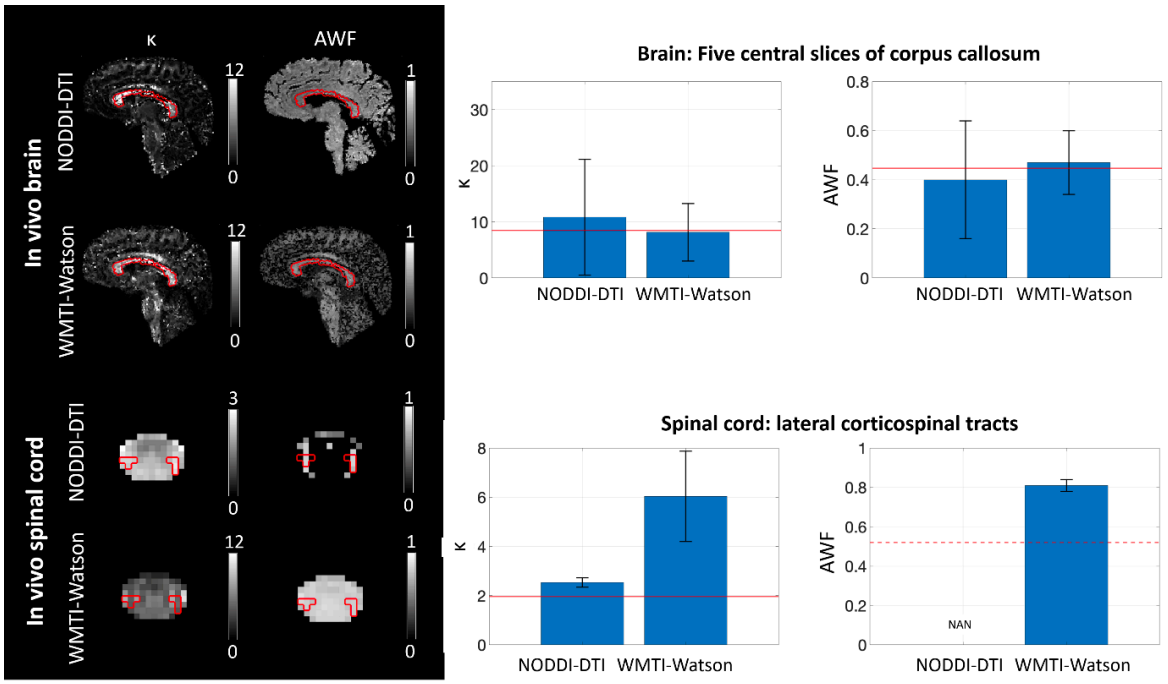


Figure 26: Bar plots displaying the Watson concentration parameter ($\kappa$) and axonal water fraction ($AWF$) within the five central slices of the corpus callosum and the lateral corticospinal tracts in the spinal cord (refer to Table 2 for details on the datasets). The corpus callosum was manually segmented, while the lateral corticospinal tracts were segmented using the PAM50 spinal cord white matter atlas. The regions of interest are highlighted as red segmentation lines on the images. In the box plots, red horizontal lines represent literature values obtained from histology, while the red dotted line represents a literature value from the brain due to the absence of a corresponding value for the spinal cord. Values of orientation dispersion index reported in the literature were converted to $\kappa$ using Equation (1) in (Mollink et al., 2017). Within the corpus callosum, $\kappa$ values were (mean ± std) 10.82 ± 10.31 and 8.14 ± 5.13 when derived from the NODDI-DTI (single shell) and WMTI-Watson model (two shells), respectively. These values fall within the range of literature values obtained post-mortem using polarized light imaging (Mollink et al., 2017). $AWF$ values derived from NODDI-DTI (0.40 ± 0.24) and WMTI-Watson model (0.47 ± 0.13) were similar to literature values obtained using electron microscopy in a cynomolgus macaque (Stikov et al., 2015). Within the lateral corticospinal tracts, $\kappa$ values derived from NODDI-DTI were notably lower than those derived from WMTI-Watson (2.53 ± 0.19 vs. 6.04 ± 1.84) and were consistent with

literature values obtained in a post-mortem specimen (Grussu et al., 2017). $AWF$ values derived from the WMTI-Watson model in the spinal cord were substantially higher (0.81 ± 0.03) compared to a literature value obtained in the brain (red dotted line). The estimation of $AWF$ for the spinal cord was not feasible using the NODDI-DTI model, as DTI-derived mean diffusivity ($MD$) values fell below the range where the NODDI-DTI model provides a valid representation (refer to Equation (4) in (Edwards et al., 2017)). This discrepancy could be attributed to either the underestimation of $MD$ due to kurtosis bias (Figure 21) or the invalidity of fixed compartmental diffusivities in the NODDI-DTI model. These results indicate that WMTI-Watson yields more accurate estimation of $\kappa$ and $AWF$ for the brain, while NODDI-DTI yields a more accurate estimation of $\kappa$ for the spinal cord. This could be a consequence of non-optimal $b$-values for kurtosis estimation in the spinal cord. Source: Figure and modified caption reproduced from (David et al., 2024), published under CC BY 4.0 license.

## 6.4 Effect of Rician bias correction on biophysical parameter estimates

To demonstrate the impact Rician bias correction can have on biophysical parameter maps, the exemplary in vivo brain and in vivo spinal cord datasets (see section 6.1 for details) were computed with the full recommended analysis pipeline (see section 0 for details) with and without the use of Rician bias correction. From these results, the biophysical parameters Watson concentration parameter ($\kappa$) and axonal water fraction ($AWF$) were estimated via WMTI-Watson and NODDI-DTI. For the estimation via NODDI-DTI, only the lower shell was used as this model assumes a DTI dataset. WMTI-Watson was performed with all available diffusion shells as this model assumes a DKI dataset.

As RBC slightly decreased the mean of the kurtosis tensor in the brain and spinal cord DKI maps, the Watson concentration parameter is increased. The estimation of $AWF$ using the NODDI-DTI model was not feasible in the spinal cord, as the mean diffusivity ($MD$) values derived from DTI fell below the range where the NODDI-DTI model provides a valid representation (Edwards et al., 2017). This discrepancy could be attributed to either the

underestimation of $MD$ due to kurtosis bias (see Figure 21 for an example) or the invalidity of fixed compartmental diffusivities in the NODDI-DTI model (see section 6.2.5).

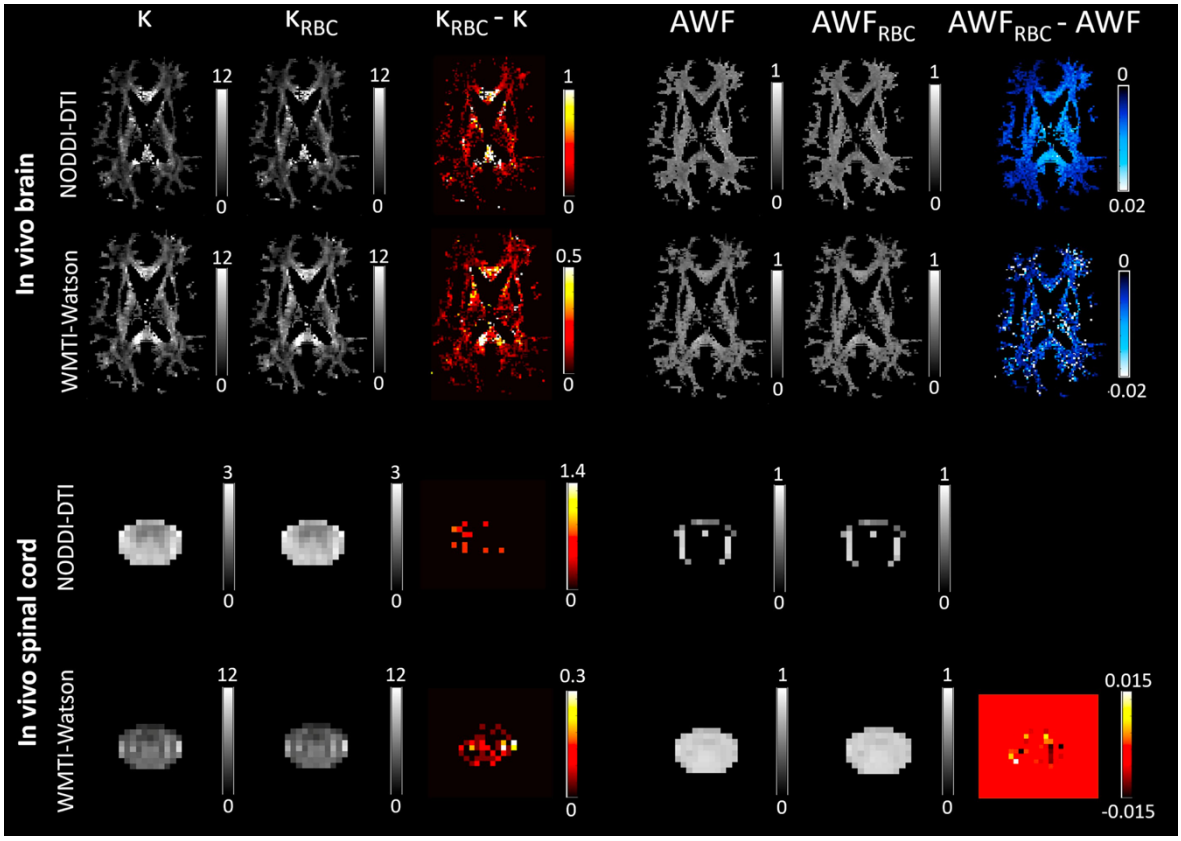


Figure 27: The impact of Rician bias correction (RBC) on maps of biophysical parameter estimates, derived from the NODDI-DTI and WMTI-Watson models, including Watson concentration parameter ($\kappa$) and axonal water fraction ($AWF$), in an in vivo brain and spinal cord dataset (refer to Table 2 for details on the datasets). Being derived from white matter biophysical models, the parameter maps were masked for the white matter in the brain dataset. For the spinal cord, we refrained from masking due to the difficulty of obtaining an accurate white matter mask. These maps were computed both without (left column) and with (middle column) RBC; their voxel-wise difference, referred to as the Rician bias, is shown in the right column. RBC slightly decreased the mean of the kurtosis tensor in both the brain and spinal cord, which resulted in an increase in $\kappa$. The estimation of $AWF$ using the NODDI-DTI model was not feasible in the spinal cord, as the mean diffusivity ($MD$) values derived from DTI fell below the range where the NODDI-DTI model provides a valid representation (refer to Equation (4) in (Edwards et al., 2017)).

This discrepancy could be attributed to either the underestimation of MD due to kurtosis bias (Figure 21) or the invalidity of fixed compartmental diffusivities in the NODDI-DTI model. Source: Figure and modified caption reproduced from (David et al., 2024), published under CC BY 4.0 license.

## 6.5 Comparison of different denoising methods

ACID provides the denoising method msPOAS (Becker et al., 2014), which was used for the processing of the example datasets (see section 0 for details). Due to the in ACID implemented modular organization, it was possible to integrate additional denoising methods from external sources into ACID. Two popular denoising approaches are now additionally integrated into the ACID toolbox, named local principal component analysis (LPCA) (Manjón et al., 2013) and the Marchenko-Pastur principal component analysis (MPPCA) (Veraart et al., 2016) (see section 5.5 for the specific requirements for the operating system).

To compare the performance of these three denoising methods, an analysis based on simulated data were performed. The estimated kurtosis parameters (Figure 22 shows the parameter maps) for the in vivo brain dataset (see Table 2 for details) were used to generate a synthetic dMRI dataset which was used as a quasi-noise-free ground truth. This dataset was then contaminated with synthetic noise taken out of a circularly symmetric complex normal distribution $CN(0, \sigma^2)$, where $\sigma = \frac{S_0}{SNR}$ and several $SNR = 5, 15, 30, 39, 52, 100$ which are the values that were used also in (Oeschger et al., 2023b). For these different SNR datasets, the denoising was performed for each method followed by a kurtosis fit using the NLLS algorithm. In addition, the DKI fit was performed without the previous use of denoising. Figure 28 shows exemplary slices of the axial diffusivity ($AD$), radial diffusivity ($RD$), mean kurtosis tensor ($MW$), axial kurtosis tensor ($AW$), and radial kurtosis tensor ($RW$) which were calculated using the SNR 5 (highest noise contamination) dataset. To

quantify the denoising performance, the normalized root-mean-square error (NRMSE) was calculated to quantify the deviation of the estimated DKI parameters (one noise realization) from the ground truth (see Figure 29 for the visualization of the results). The NRMSE can be defined as:

$$NRMSE = \frac{\sqrt{\frac{1}{N}\sum_{i=1}^{N}(\rho_i - p_i)^2}}{\frac{1}{N}\sum_{i=1}^{N}\rho_i}, \tag{32}$$

where $\rho_i$ is the ground truth and $p_i$ the estimated parameter per voxel. The values were calculated within a ROI containing the white matter voxels (see red circled area in Figure 28 first line). The results show that the NRMSE is reduced by using denoising in general if the SNR is low but not for all parameters in the same way: The NRMSE was reduced for RD and RW clearly visible for SNRs of 15 and lower. For $AW$, this effect was visible for SNRs below 30. In contrast, the parameters the NRMSE of $AD$ was not reduced and for the $MW$ the trend is unstable. Another outcome of this analysis was that the NRMSE is increased if the SNR is higher (30-40) for all estimated DKI parameters compared to the dataset that was processed without denoising. The only exception was the MPPCA processed data, meaning that there is no "denoising" bias introduced when using MPPCA and the results are mostly similar to the not-denoised data. For a further interpretation of the results, the relative difference between the DKI parameters that are obtained with the use of denoising to the parameters estimated without denoising was calculated and visualized in Figure 30. The results imply that denoising is only beneficial when used for low SNR datasets. For high SNRs, denoising has no benefit for the dataset (MPPCA) or introduces an additional bias (msPOAS and LPCA) which can also be seen for the NRMSE results (see Figure 29).

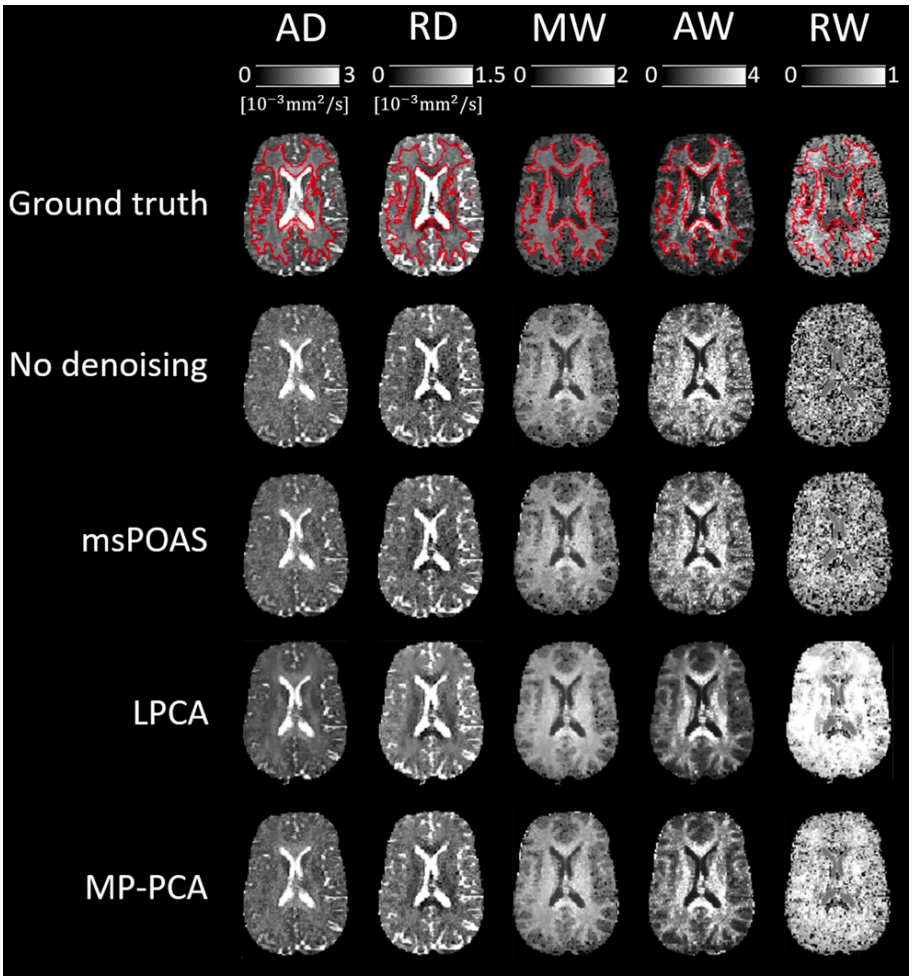


Figure 28: Qualitative illustration of the effect of denoising on maps derived from diffusion kurtosis imaging (DKI). Shown are maps of axial diffusivity ($AD$), radial diffusivity ($RD$), mean kurtosis tensor ($MW$), axial kurtosis tensor ($AW$), and radial kurtosis tensor ($RW$). The maps were obtained by fitting the kurtosis model to simulated noisy dMRI data (signal + noise) with a signal-to-noise ratio (SNR) of 5, both before (no denoising) and after employing different denoising methods (msPOAS, LPCA, MP-PCA). The DKI metric maps obtained from the simulated noise-free dMRI data (signal only) are also shown for comparison (ground truth). The white matter mask used for calculating the normalized root-mean-square error (NRMSE) between the obtained DKI metrics and the ground truth is overlaid as a red segmentation line on the ground truth maps. Source: Figure and modified caption reproduced from (David et al., 2024), published under CC BY 4.0 license.

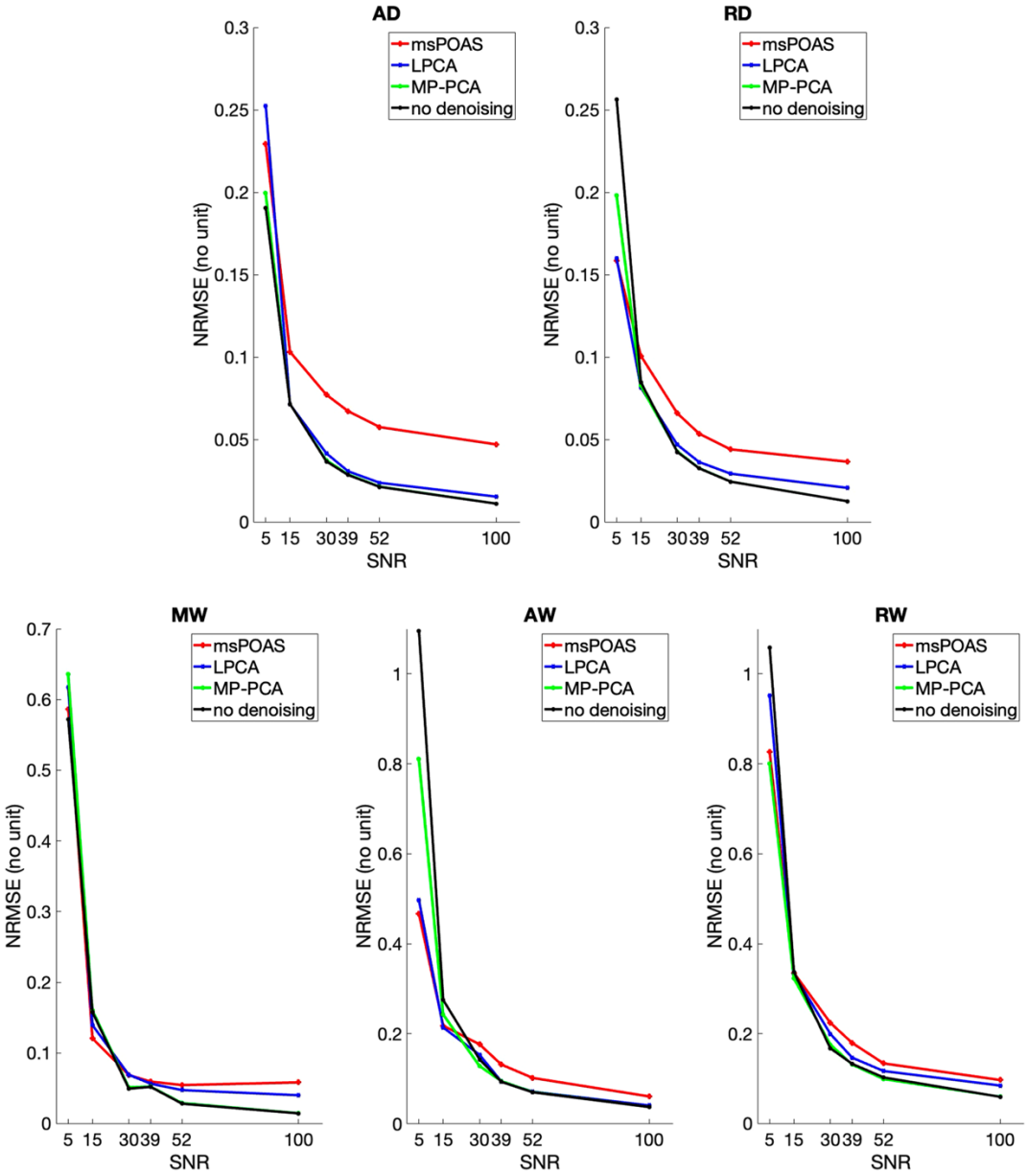


Figure 29: Quantitative illustration of the effect of denoising on maps derived from diffusion kurtosis imaging (DKI) (one noise realization). The plots show the normalized root-mean-square error (NRMSE) between (i) DKI metrics obtained from simulated noisy dMRI data (signal + noise) with varying signal-to-noise ratios (SNR), both before (no denoising) and after employing different denoising methods (msPOAS, LPCA, MP-PCA), and (ii) DKI metrics obtained from noise-free dMRI data (signal only). NRMSE was computed across white matter voxels (see Figure 28 for the white matter mask) for the following DKI metrics: axial diffusivity ($AD$), radial diffusivity ($RD$), mean kurtosis tensor ($MW$), axial kurtosis tensor ($AW$), and radial kurtosis tensor ($RW$). Denoising methods reduced NRMSE from the ground truth compared with the "no denoising" scenario only

in the low-SNR domain, although not consistently for all DKI metrics. At high SNRs (above 30–40), denoising increased NRMSE for all DKI metrics, except for the MP-PCA method, which yielded results comparable with the “no denoising” scenario. Source: Figure and modified caption reproduced from (David et al., 2024), published under CC BY 4.0 license.

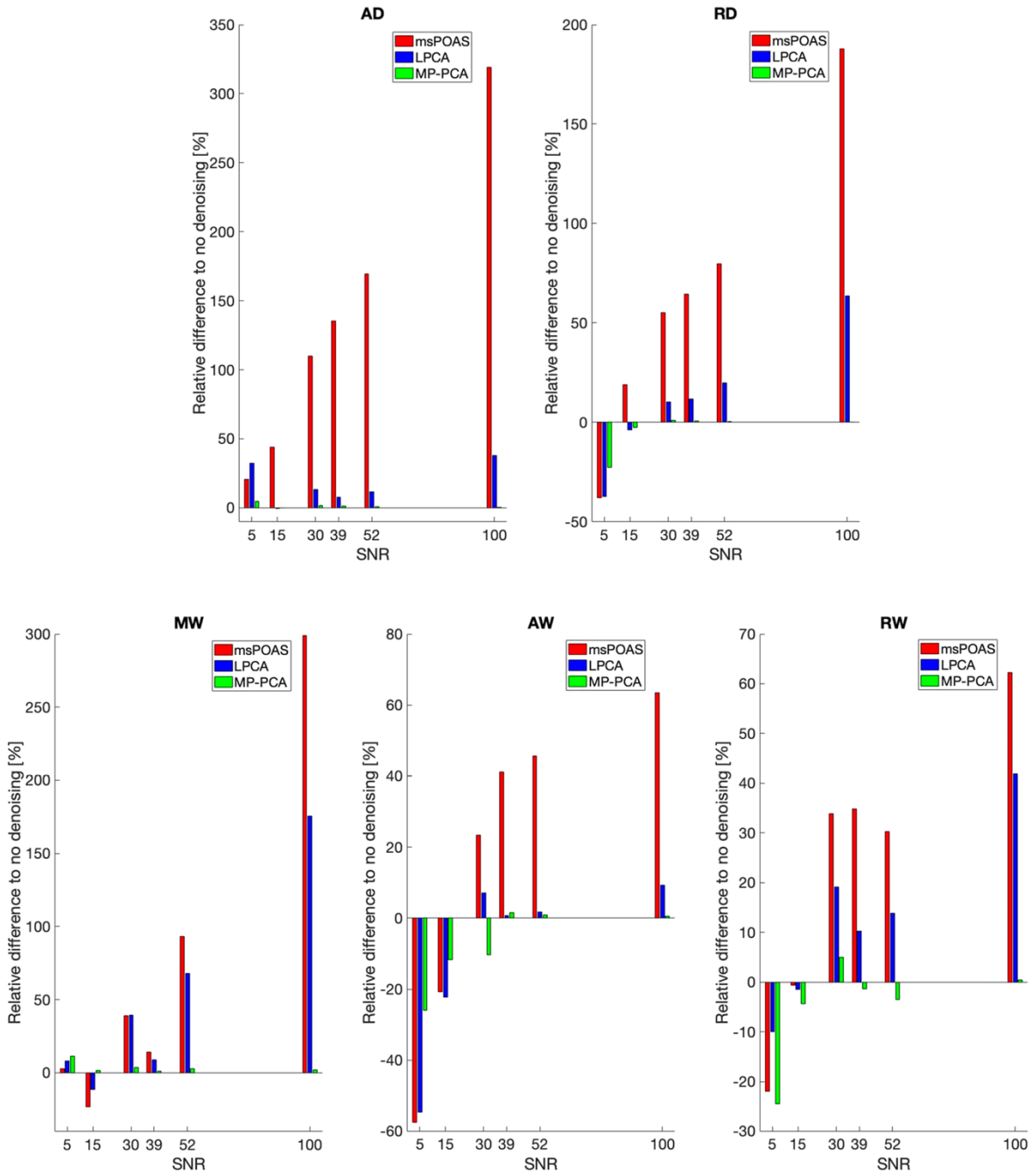


Figure 30: Quantitative illustration of the effect of denoising on maps derived from diffusion kurtosis imaging (DKI). The plots show the relative difference in DKI metrics obtained from simulated noisy dMRI data (signal + noise) with varying signal-to-noise

ratios (SNR) after employing different denoising methods (msPOAS, LPCA, MP-PCA) to those obtained without denoising (one noise realization). The relative difference was computed across white matter voxels (see Figure 28 for the white matter mask) for the following DKI metrics: axial diffusivity ($AD$), radial diffusivity ($RD$), mean kurtosis tensor ($MW$), axial kurtosis tensor ($AW$), and radial kurtosis tensor ($RW$). Denoising introduced substantial improvements in the investigated DKI metrics only in the low-SNR domain, although not consistently across all DKI metrics. When using msPOAS and LPCA, the relative differences were greater compared with using MP-PCA, with msPOAS introducing the highest bias. At high SNRs (above 30–40), the relative difference to the "no denoising" scenario was negligible for MP-PCA. Source: Figure and modified caption reproduced from (David et al., 2024), published under CC BY 4.0 license.

## 6.6 Example group analysis

To show the benefits of the in ACID implemented BIDS compliant storage system and workflow for group analyses, an analysis of four brain dMRI datasets was done beginning from the raw DICOM data. For acquisition details see Table 4.

Table 4: Scan parameters for the four in vivo brain dMRI datasets.

| Parameter | | Parameter | |
|---|---|---|---|
| *Imaged body part or tissue* | entire brain (including cerebellum) of four healthy volunteer | *Multi-band imaging* | 3 |
| *Scanner* | 3T Siemens Prisma Fit | *Phase partial Fourier* | 7/8 |
| *Receive coils* | 64-channel Head/Neck | *Phase-encoding dir.* | A-P |
| *Sequence* | 2D single-shot spin-echo EPI | *Readout bandwidth [Hz/pixel]* | 1934 |
| *Volumes and b-values [s/mm$^2$] (number of gradient directions)* | b = 0 (11); b = 500 (7); b = 1000 (29); b = 2000 (64) | *EPI spacing [ms]* | 0.64 |
| *Number of slices* | 81 (interleaved, no gap) | *EPI factor* | 134 |
| *Resolution [mm$^3$]* | 1.7 x 1.7 x 1.7 | *Acquisition time [min:sec]* | 7:58 |
| *Field of view [mm$^3$]* | 232 x 138 x 229 | *Additional data with reversed phase-encoding direction* | a single b0 volume acquired with reversed phase-encoding direction |

| | |
|---|---|
| *Echo time [ms]* | 74,60 |
| *Repetition time [ms]* | 3100 |
| *Parallel imaging* | 2x (GRAPPA) |

To convert the raw DICOM data to BIDS-compliant NIfTI data, the open available conversion software BIDSCOIN[29] (Zwiers et al., 2022) was used. However, any other software which provides BIDS-compliant NIfTI output should be sufficient. The converted dMRI datasets were then processed via an overall four subject scripted analysis pipeline (see section 0 for details), including all recommended processing steps for in vivo brain dMRI datasets (ECMOCO, MPPCA, RBC, HySCO). For the generation of parameter maps, the modules DKI, SMI, WMTI-Watson, WMTI, and NODDI-DTI were used. The structure of the BIDS-compatible ACID-storage system during the processing steps is visualized in Figure 31.

[29] https://bidscoin.readthedocs.io/en/latest/

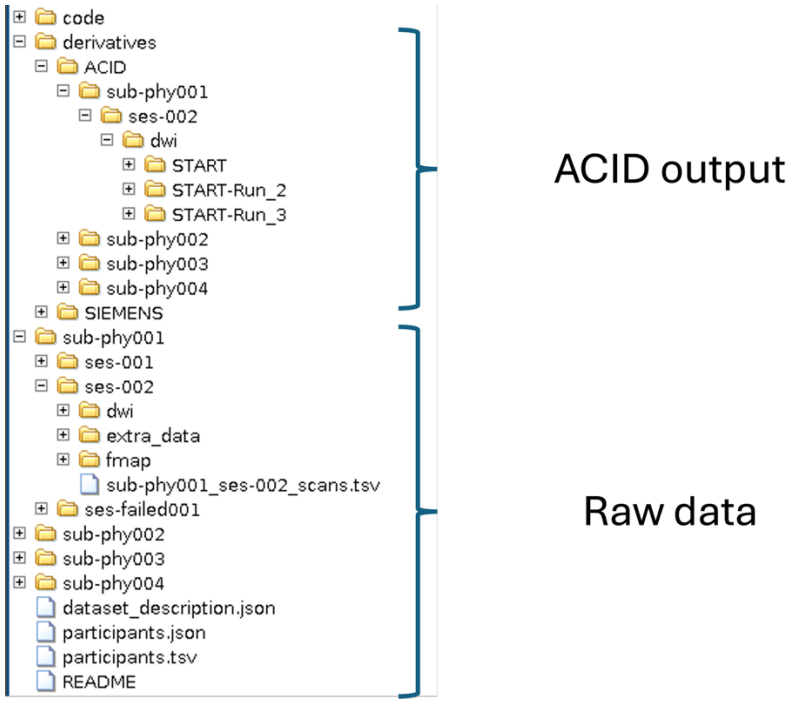


Figure 31: Visualization of the BIDS-compliant folder structure ACID generates for BIDS-compliant input datasets. The BIDS storage structure of the raw data is recreated within the derivatives/ACID folder. This ensures a clear and easy-to-script data storage of the processed dMRI data or parameter maps.

ACID generates a BIDS-compliant derivatives structure in which a dedicated folder is created for each subject, session, modality (here "dwi"), and in addition a "START" folder which separates each pipeline run. This makes it possible to analyze the results of all subjects easily in one script as only the subject number and/or session number has to be modified, which can be done via a "for" loop.

To generate the coefficient of variation (COV) and group mean maps across all four subjects together, a registration was performed via SPM (Penny et al., 2011). The shoot modules (Ashburner and Friston, 2011) were used as they provide nonlinear registration to the MNI space with high precision and less additional smoothing. This is important to avoid partial volume effects across and within tissue classes (i.e., white matter, grey matter, and CSF). For the template creation of shoot, the segment function of SPM was used. After registering all computed parameter maps and segments, these were transformed to the MNI space.

Figure 32 shows the generated white and gray matter masks for each subject in native space.

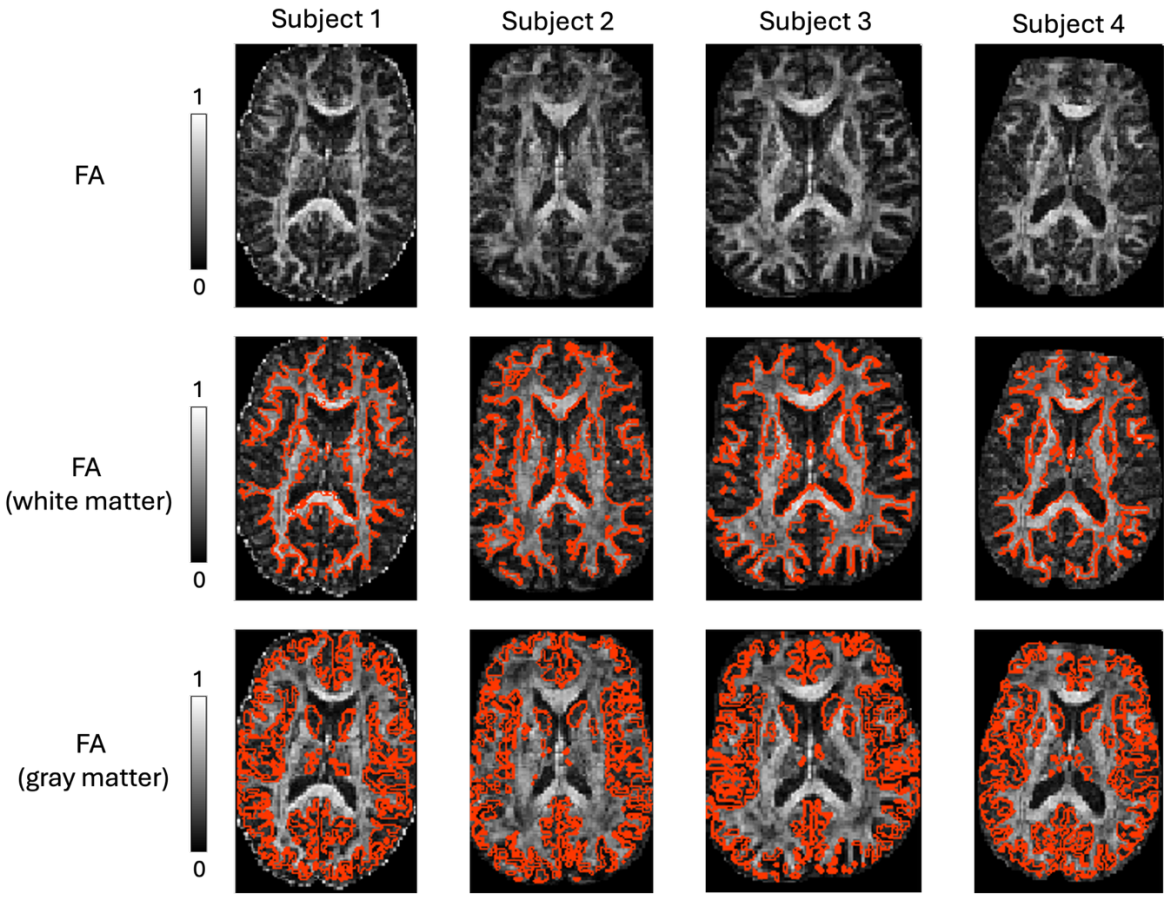


Figure 32: Visualization of the white and gray matter masks which were used for the further analysis. The fractional anisotropy ($FA$) map of all subjects is shown on the upper row. The red circled area displays the analyzed white matter region (middle row) and gray matter region (bottom row) for each subject.

For the results of each parameter estimation method within the white matter mask, the mean and standard deviation over the four subjects in subject space were plotted, and the across-subject COV was calculated. For DKI, the gray matter region was analyzed as well. The results are displayed in Figure 33 (white matter) and Figure 34 (gray matter) for DKI, Figure 37 for SMI, Figure 40 for NODDI-DTI, Figure 43 for WMTI-Watson, and Figure 46 for WMTI.

The calculated COV maps in MNI space are shown in Figure 35 for DKI, Figure 38 for SMI, Figure 41 for NODDI-DTI, Figure 44 for WMTI-Watson, and Figure 47 for WMTI.

The group mean maps in MNI space were calculated and are shown in Figure 36 for DKI, Figure 39 for SMI, Figure 42 for NODDI-DTI, Figure 45 for WMTI-Watson, and Figure 48 for WMTI.

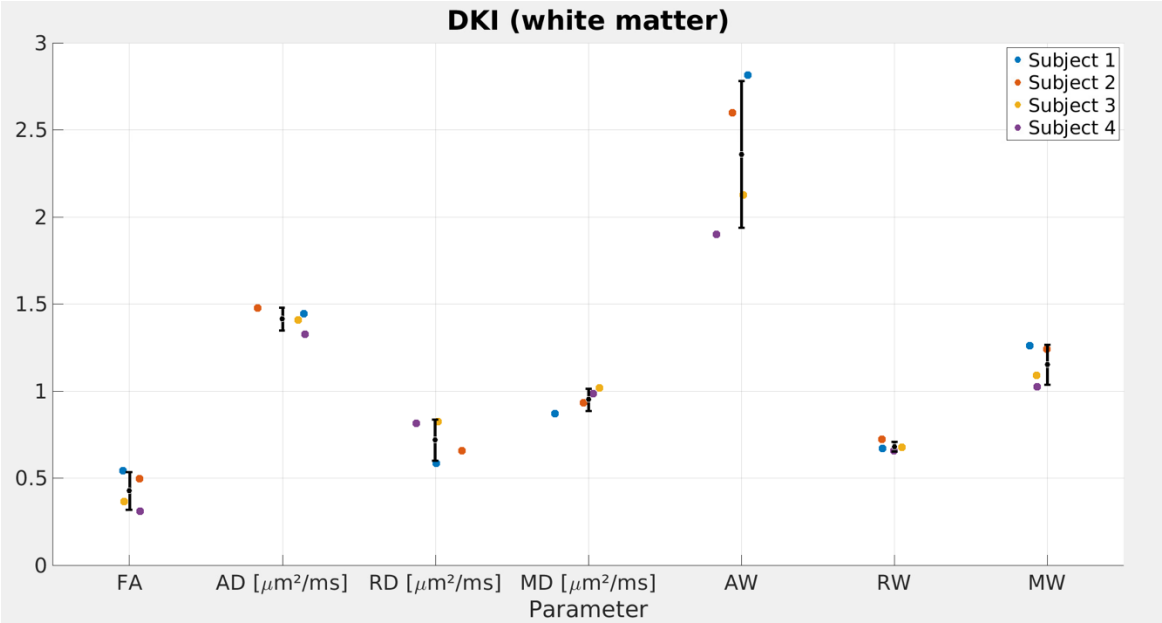


Figure 33: Quantitative illustration of the statistical analysis of the four via DKI in white matter analyzed subjects. The mean and standard deviation (black) as well as the subject-specific values (colored dots) were computed across white matter voxels (see Figure 32 for the white matter mask) for the following DKI metrics: axial diffusivity ($AD$), radial diffusivity ($RD$), mean diffusivity ($MD$), axial kurtosis tensor ($AW$), radial kurtosis tensor ($RW$), mean kurtosis tensor ($MW$), and fractional anisotropy ($FA$). The across-subject COV was estimated for $FA$ (25.3%), $AD$ (4.6%), $RD$ (16.5%), $MD$ (6.8%), $AW$ (17.8%), $RW$ (4.1%), and $MW$ (10.0%).

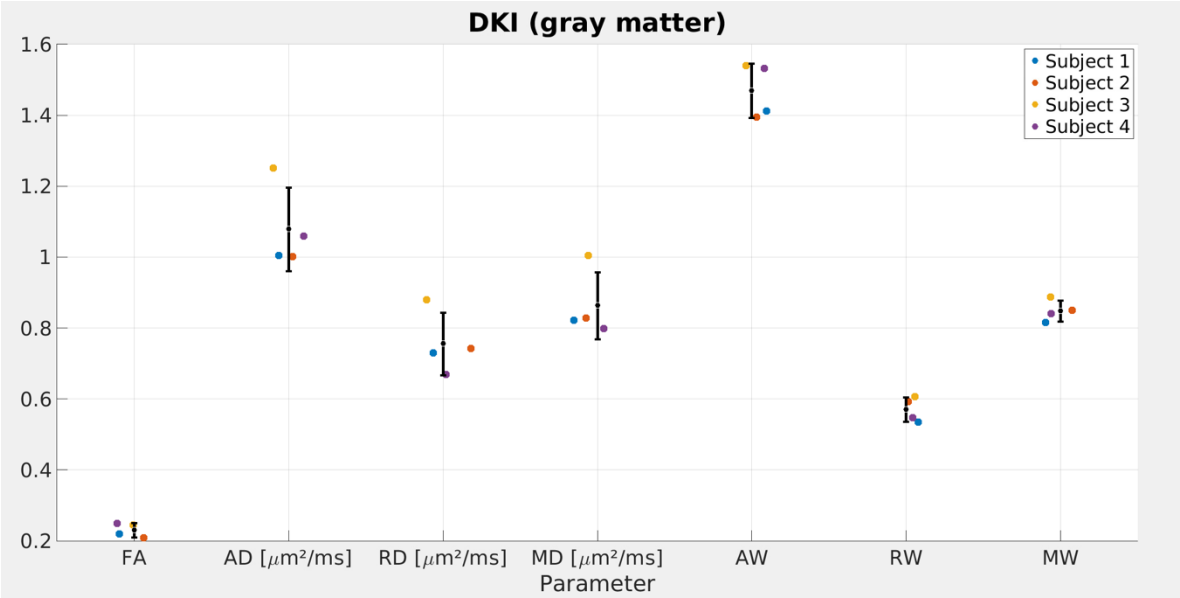


Figure 34: Quantitative illustration of the statistical analysis of the four via DKI in gray matter analyzed subjects. The mean and standard deviation (black) as well as the subject-specific values (colored dots) were computed across gray matter voxels (see Figure 32 for the gray matter mask) for the following DKI metrics: fractional anisotropy ($FA$), axial diffusivity ($AD$), radial diffusivity ($RD$), mean diffusivity ($MD$), axial kurtosis tensor ($AW$), radial kurtosis tensor ($RW$), and mean kurtosis tensor ($MW$). The results showed a relatively high consistency over all DKI parameters; the across-subject COV was estimated for $FA$ (8.6%), $AD$ (10.9%), $RD$ (11.8%), $MD$ (10.9%), $AW$ (5.2%), $RW$ (6.0%), and $MW$ (3.5%).

The DKI parameter results showed an across-subject COV up to 25.3% ($FA$) for white matter (see Figure 33) and up to 11.8% ($RD$) for gray matter (see Figure 34) over all parameters. The highest non-fraction across-subject COV was estimated in white matter for $AW$ (17.8%) and in gray matter for $RD$ (11.8%). The lowest across-subject COV value was estimated for white matter for $RW$ (4.1%) and for gray matter for $MW$ (3.5%).

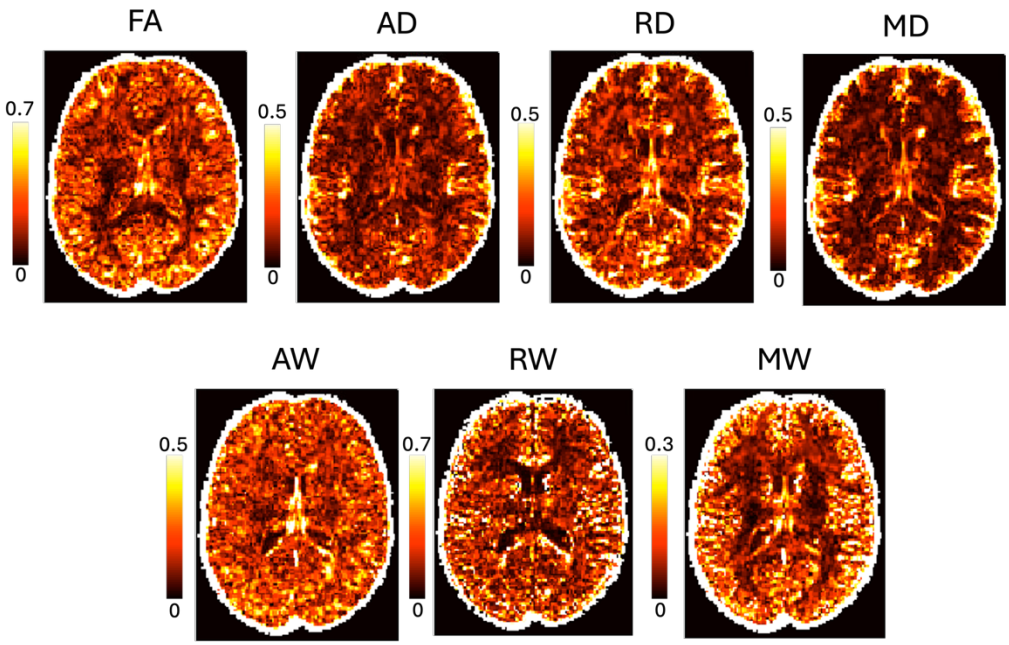


Figure 35: Across-subject coefficient of variation maps of the DKI parameter for the four subjects. Upper row: fractional anisotropy ($FA$), axial diffusivity ($AD$), radial diffusivity ($RD$), and mean diffusivity ($MD$). Lower row: axial kurtosis tensor ($AW$), radial kurtosis tensor ($RW$), and mean kurtosis tensor ($MW$). The maps are mostly homogeneous; however, for $RD$ and $RW$, the values are higher in the corpus callosum, which indicates a higher variability in this area.

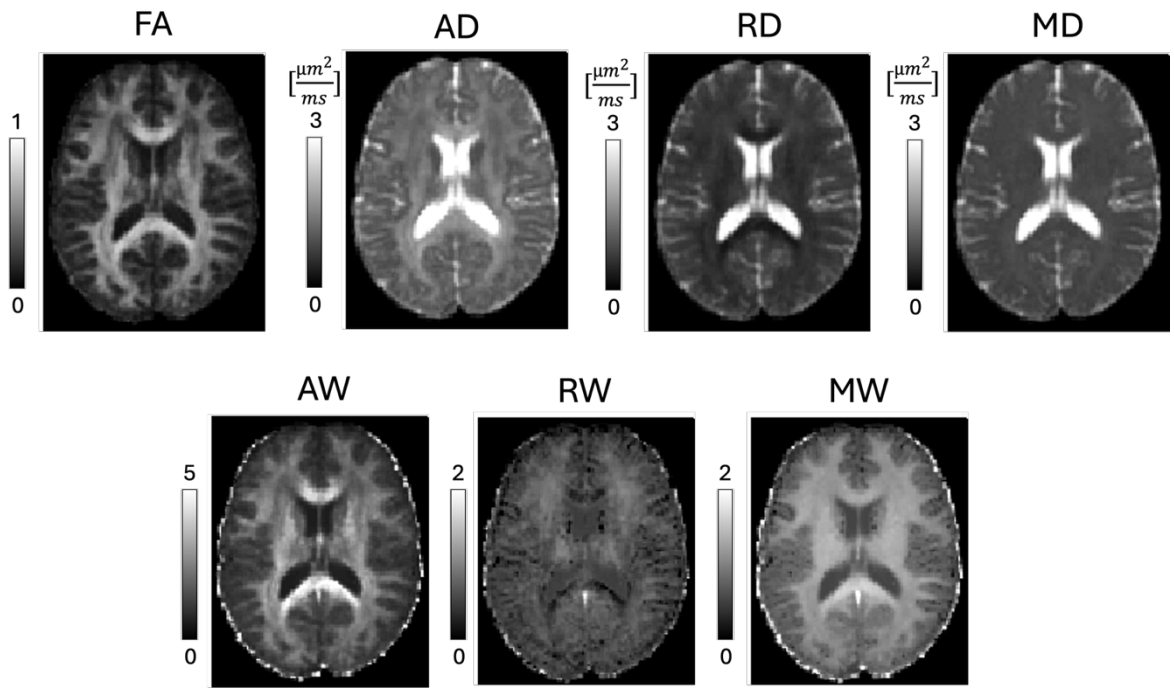


Figure 36: : Group mean maps of the DKI parameter for the four subjects. Upper row: fractional anisotropy ($FA$), axial diffusivity ($AD$), radial diffusivity ($RD$), and mean diffusivity ($MD$). Lower row: axial kurtosis tensor ($AW$), radial kurtosis tensor ($RW$), and mean kurtosis tensor ($MW$). The maps are mostly homogeneous; however, for $AW$, the values are higher in the corpus callosum, which could indicate an overestimation in this area.

The across-subject COV (see Figure 35) and group mean maps (see Figure 36) are mostly homogeneous; however, for $AW$, the values are higher in the corpus callosum group mean map, which could indicate an overestimation in this area. For $RD$ and $RW$, the values are higher in the corpus callosum across-subject COV map, which indicates a higher variability in this area.

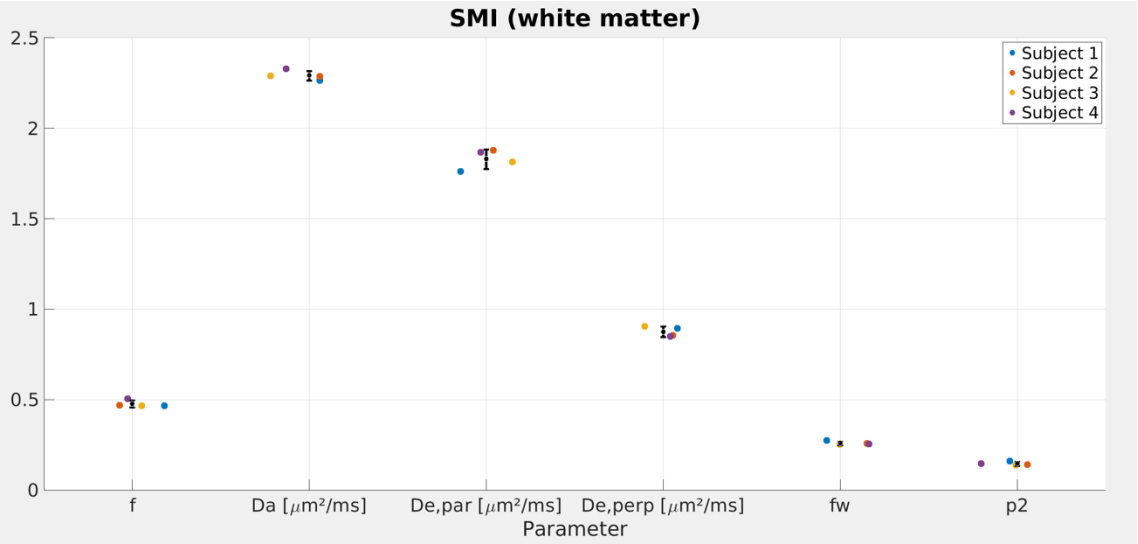


Figure 37: Quantitative illustration of the statistical analysis of the four via SMI analyzed subjects. The mean and standard deviation (black) as well as the subject-specific values (colored dots) were computed across white matter voxels (see Figure 32 for the white matter mask) for the following SMI metrics: axonal water fraction (AWF/$f$), intra-axonal diffusivity ($D_a$), parallel and perpendicular extra-axonal diffusivities ($D_{e,par}$ and $D_{e,perp}$), free water volume fraction ($f_w$), and anisotropy ($p_2$). The results show a relatively high consistency across all subjects for all SMI parameters; the across-subject COV was estimated for $f$ (4.0%), $D_a$ (1.1%), $D_{e,par}$ (2.9%), $D_{e,perp}$ (3.3%), $f_w$ (3.6%), and $p_2$ (6.9%).

The SMI parameter results show a relatively low across-subject COV ($< 7\%$) over all parameters estimated in white matter (see Figure 37). The highest across-subject COVs were estimated for anisotropy $p_2$ (6.9%) and diffusivity $D_{e,perp}$ (3.3%). The lowest across-subject COVs were estimated for fraction $f_w$ (3.6%) and diffusivity $D_a$ (1.1%).

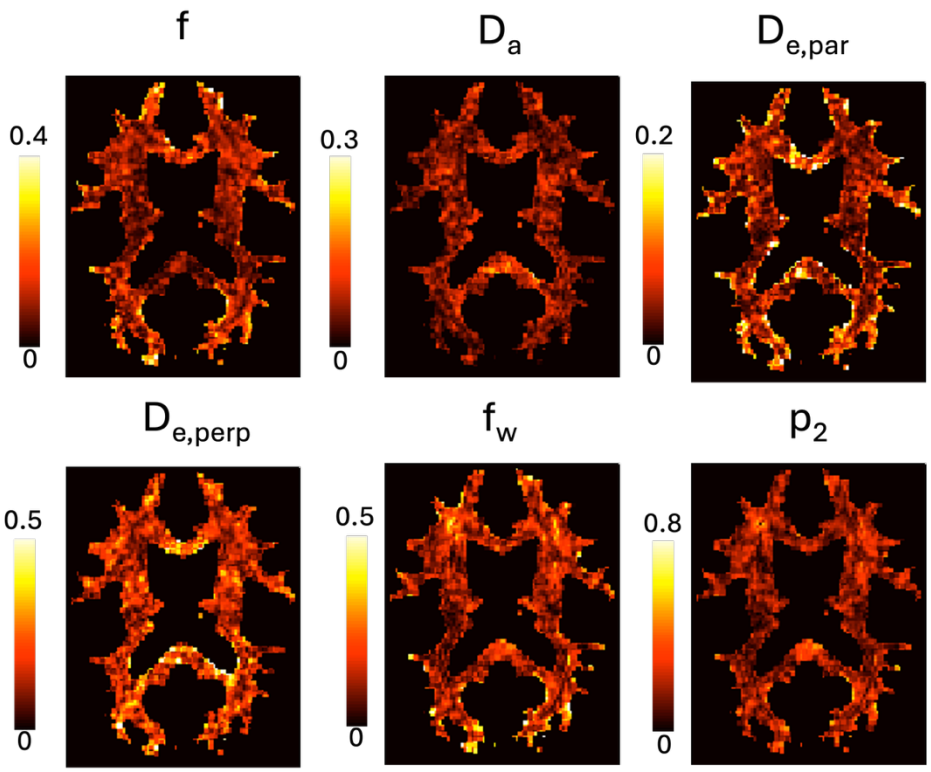


Figure 38: Across-subject coefficient of variation maps for the estimated SMI parameter for the four subjects. Upper row: axonal water fraction (AWF/$f$), intra-axonal diffusivity ($D_a$), and parallel extra-axonal diffusivity ($D_{e,par}$). Lower row: perpendicular extra-axonal diffusivity $D_{e,perp}$, free water volume fraction ($f_w$), and anisotropy ($p_2$). The maps are mostly homogeneous; however, for $D_{e,par}$, the values are higher in the corpus callosum, which indicates a higher variability in this area.

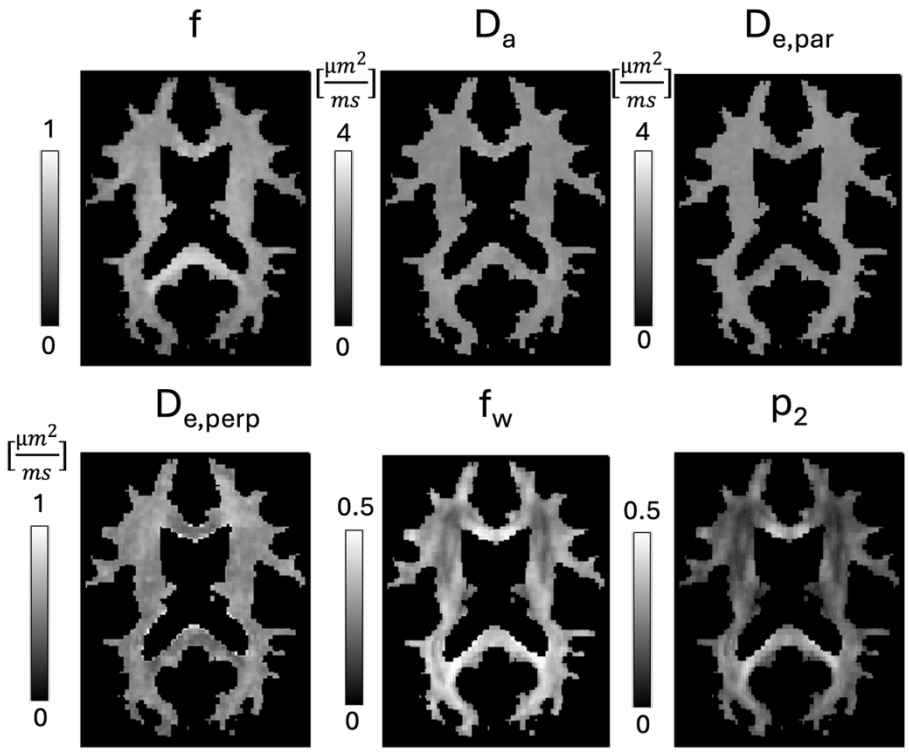


Figure 39: Group mean maps for the estimated SMI parameter for the four subjects. Upper row: axonal water fraction (AWF/$f$), intra-axonal diffusivity ($D_a$), and parallel extra-axonal diffusivity ($D_{e,par}$). Lower row: perpendicular extra-axonal diffusivity $D_{e,perp}$, free water volume fraction ($f_w$), and anisotropy ($p_2$). The maps are mostly homogeneous.

The across-subject COV (see Figure 38) and group mean maps (see Figure 39) are mostly homogeneous. However, for $D_{e,par}$, the across-subject COV values are higher in the corpus callosum, which indicates a higher variability in this area.

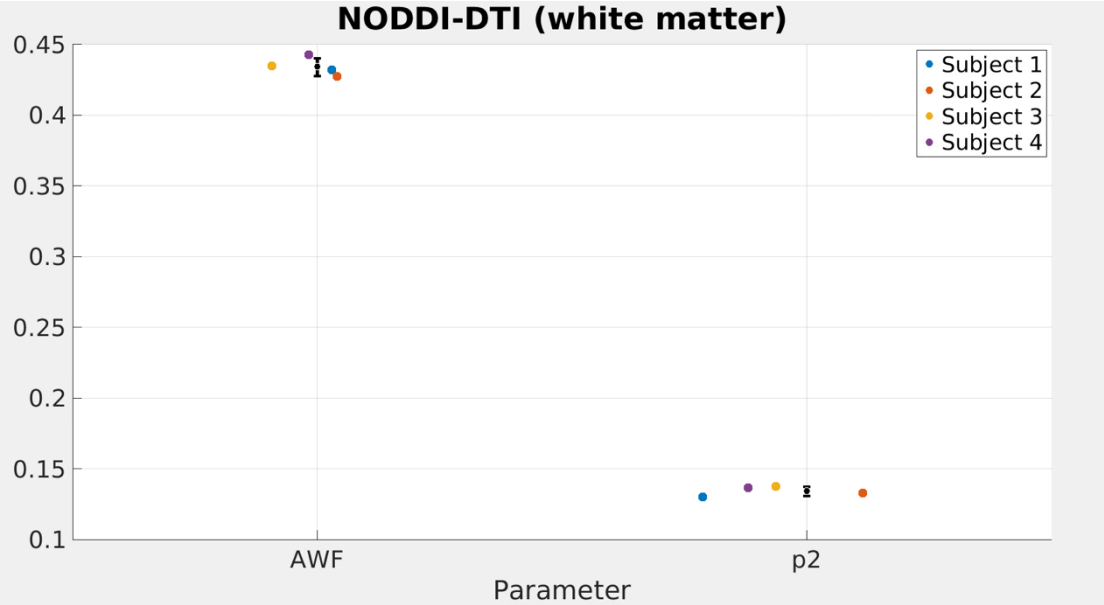


Figure 40: Quantitative illustration of the statistical analysis of the four via NODDI-DTI analyzed subjects. The mean and standard deviation (black) as well as the subject-specific values (colored dots) were computed across white matter voxels (see Figure 32 for the white matter mask) for the following NODDI-DTI metrics: axonal water fraction ($AWF/f$) and anisotropy ($p_2$). The results show a high consistency over both NODDI-DTI parameters; the across-subject COV was estimated for $AWF/f$ (1.5%) and $p_2$ (2.5%).

The NODDI-DTI parameter results showed a relatively low across-subject COV ($<$ 2.5%) over both parameters estimated in white matter (see Figure 40); the higher across-subject COV was estimated for $p_2$ (2.5%).

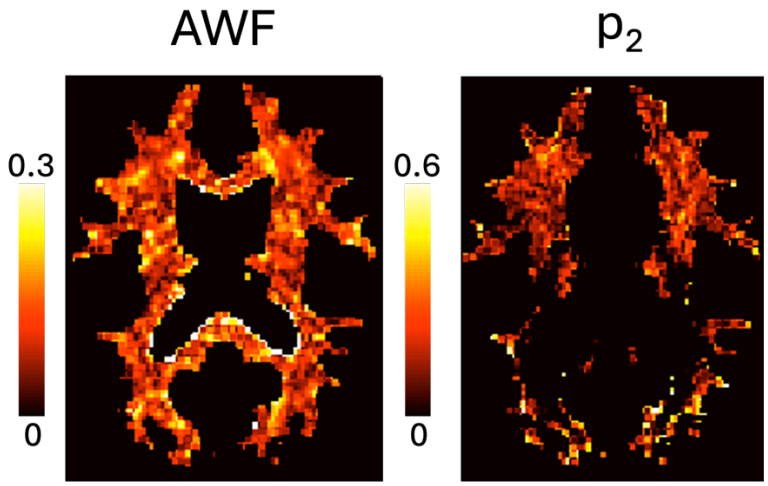


Figure 41: Across-subject coefficient of variation (COV) maps for the estimated NODDI-DTI parameters for the four subjects. Shown are the COV maps: axonal water fraction ($AWF/f$), and anisotropy ($p_2$). The $AWF/f$ map is mostly homogeneous; however, for $p_2$, many voxels (especially in the corpus callosum) are missing, and the values in the region where the fit was able to estimate values are relatively high, which indicates a higher variability in this area. A reason for the missing values could be the invalidity of fixed compartmental diffusivities in the NODDI-DTI model (see section 5.2.5).

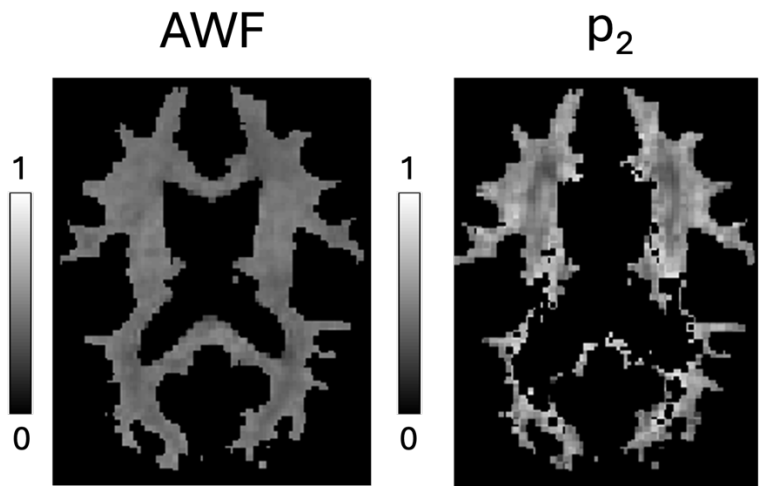


Figure 42: Group mean maps for the estimated NODDI-DTI parameters for the four subjects. Shown are the group mean maps: axonal water fraction ($AWF/f$), and anisotropy ($p_2$). The $AWF/f$ map is mostly homogeneous; however, for $p_2$, many voxels (especially in the corpus callosum) are missing. A reason for the missing values could

be the invalidity of fixed compartmental diffusivities in the NODDI-DTI model (see section 5.2.5).

The $AWF/f$ across-subject COV (see Figure 41) and group mean maps (see Figure 42) are mostly homogeneous; however, for $p_2$, many voxels (especially in the corpus callosum) are missing, and the COV values in the region where the fit was able to estimate values are relatively high, which indicates a higher variability in this area. A reason for the missing values could be the invalidity of fixed diffusivities in the NODDI-DTI model (see section 5.2.5 for details).

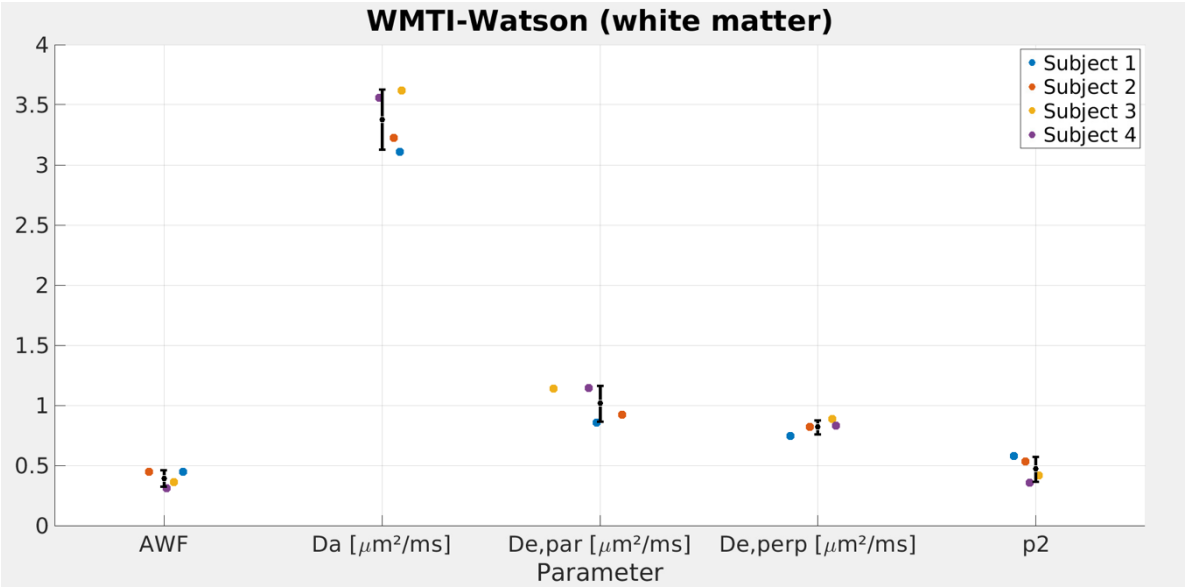


Figure 43: Quantitative illustration of the statistical analysis of the four via WMTI-Watson analyzed subjects. The mean and standard deviation (black) as well as the subject-specific values (colored dots) were computed across white matter voxels (see Figure 32 for the white matter mask) for the following WMTI-Watson metrics: axonal water fraction ($AWF/f$), intra-axonal diffusivity ($D_a$), parallel and perpendicular extra-axonal diffusivities ($D_{e,par}$ and $D_{e,perp}$), and anisotropy ($p_2$). The results show a relatively high consistency across all WMTI-Watson parameters; the across-subject COV was estimated for AWF/$f$ (17.2%), $D_a$ (7.4%), $D_{e,par}$ (14.6%), $D_{e,perp}$ (7.0%), and $p_2$ (21.9%).

The WMTI-Watson parameter results show a COV up to 22% over all parameters estimated in white matter (see Figure 43). The highest across-subject COVs were estimated for

anisotropy $p_2$ (21.9%) and diffusivity $D_{e,par}$ (14.6%). The lowest COVs were estimated for fraction AWF/$f$ (17.2%) and diffusivity $D_{e,perp}$ (7.0%).

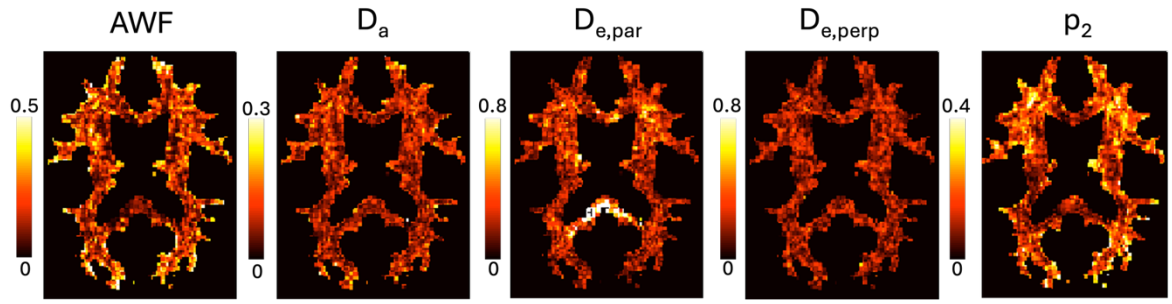


Figure 44: Across-subject coefficient of variation maps for the estimated WMTI-Watson parameter for the four subjects. Shown are the COV maps: axonal water fraction ($AWF$), intra-axonal diffusivity ($D_a$), parallel and perpendicular extra-axonal diffusivities ($D_{e,par}$ and $D_{e,perp}$), and anisotropy ($p_2$). The maps are mostly homogeneous; however, for $D_{e,par}$ the values are higher in the corpus callosum, which indicates a higher variability in this area.

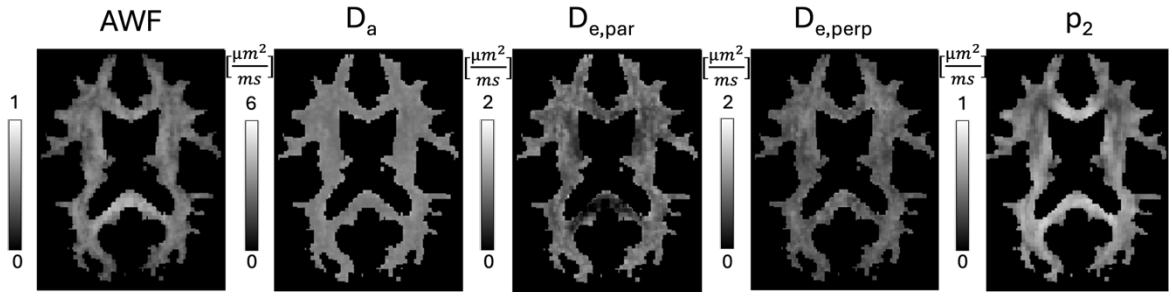


Figure 45: Group mean maps for the estimated WMTI-Watson parameter for the four subjects. Shown are the group mean maps: axonal water fraction ($AWF$), intra-axonal diffusivity ($D_a$), parallel and perpendicular extra-axonal diffusivities ($D_{e,par}$ and $D_{e,perp}$), and anisotropy ($p_2$). The maps are mostly homogeneous; however, for $D_{e,par}$ the values are lower in the corpus callosum, which could indicate a not sufficient parameter estimation in this area.

The across-subject COV (see Figure 44) and group mean maps (see Figure 45) are mostly homogeneous; however, for $D_{e,par}$, the across-subject COV values are higher and the group

mean values are lower in the corpus callosum, which indicates a higher variability and a possible underestimation in this area.

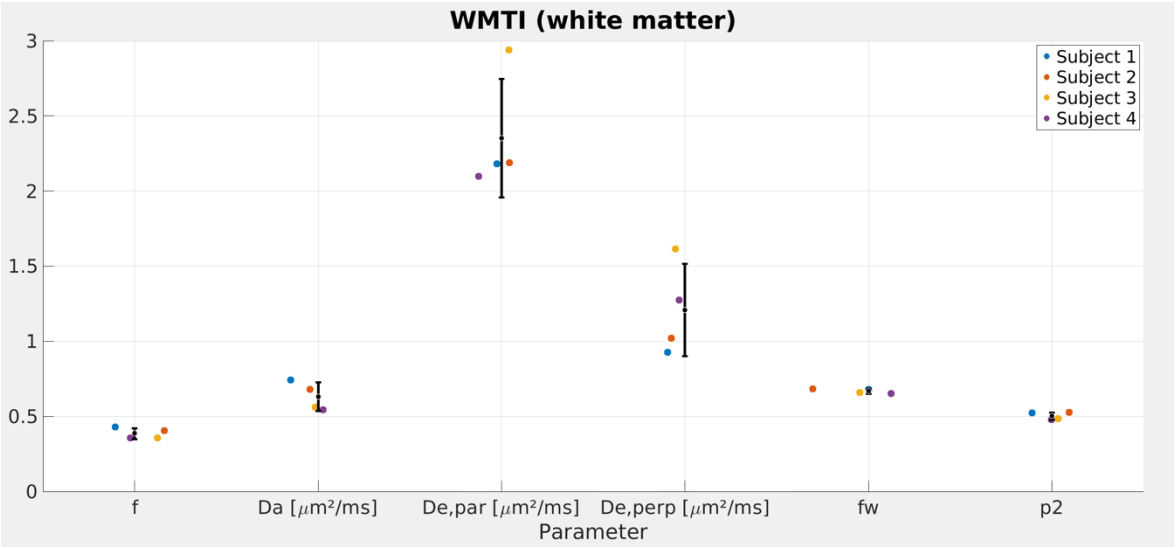


Figure 46: Quantitative illustration of the statistical analysis of the four via WMTI analyzed subjects. The mean and standard deviation (black) as well as the subject-specific values (colored dots) were computed across white matter voxels (see Figure 32 for the white matter mask) for the following WMTI metrics: axonal water fraction ($f$), intra-axonal diffusivity ($D_a$), parallel and perpendicular extra-axonal diffusivities ($D_{e,par}$ and $D_{e,perp}$), free water volume fraction ($f_w$), and anisotropy ($p_2$). The across-subject COV was estimated for $f$ (9.4%), $D_a$ (15.0%), $D_{e,par}$ (16.8%), $D_{e,perp}$ (25.5%), $f_w$ (2.5%), and $p_2$ (4.9%).

The WMTI parameter results show a relatively high consistency over all parameters estimated in white matter (see Figure 46). The highest across-subject COVs were estimated for fraction $f$ (9.4%) and diffusivity $D_{e,perp}$ (25.5%). The lowest across-subject COVs was estimated for fraction $f_w$ (2.5%) and diffusivity $D_a$ (15.0%).

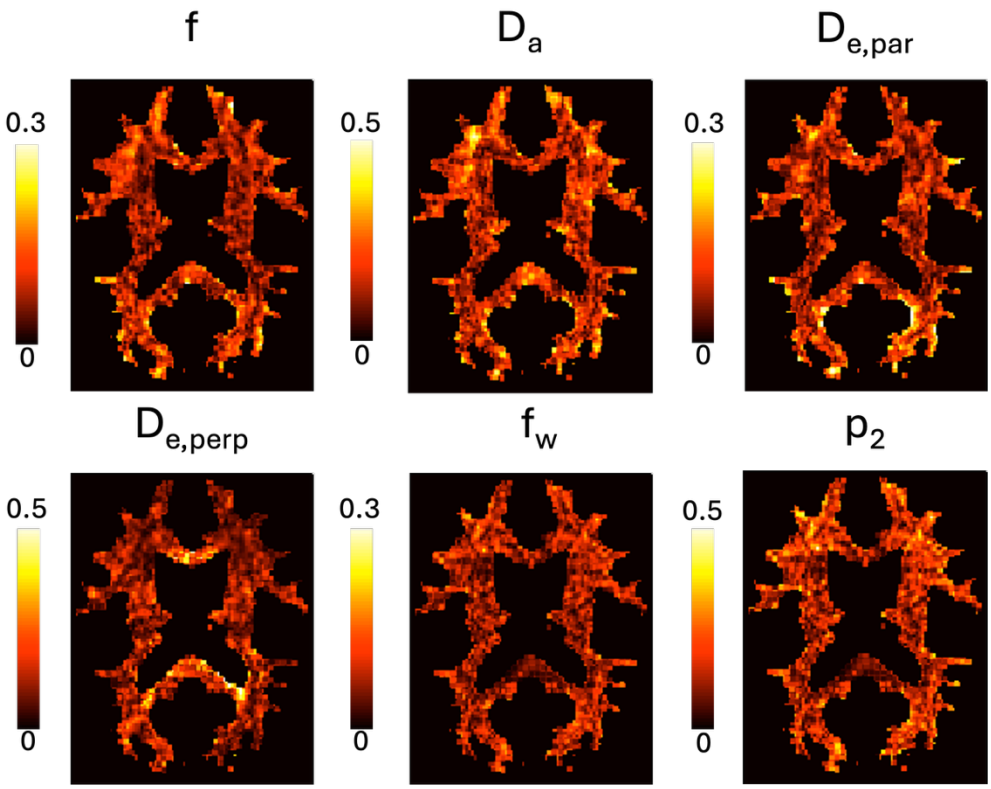


Figure 47: Across-subject coefficient of variation maps for the estimated WMTI parameter for the four subjects. Upper row: axonal water fraction ($f$), intra-axonal diffusivity ($D_a$), and parallel extra-axonal diffusivity ($D_{e,par}$). Lower row: perpendicular extra-axonal diffusivity $D_{e,perp}$, free water volume fraction ($f_w$), and anisotropy ($p_2$). The maps are mostly homogeneous; however, for $D_{e,perp}$, the values are higher in the corpus callosum, which indicates a higher variability in this area.

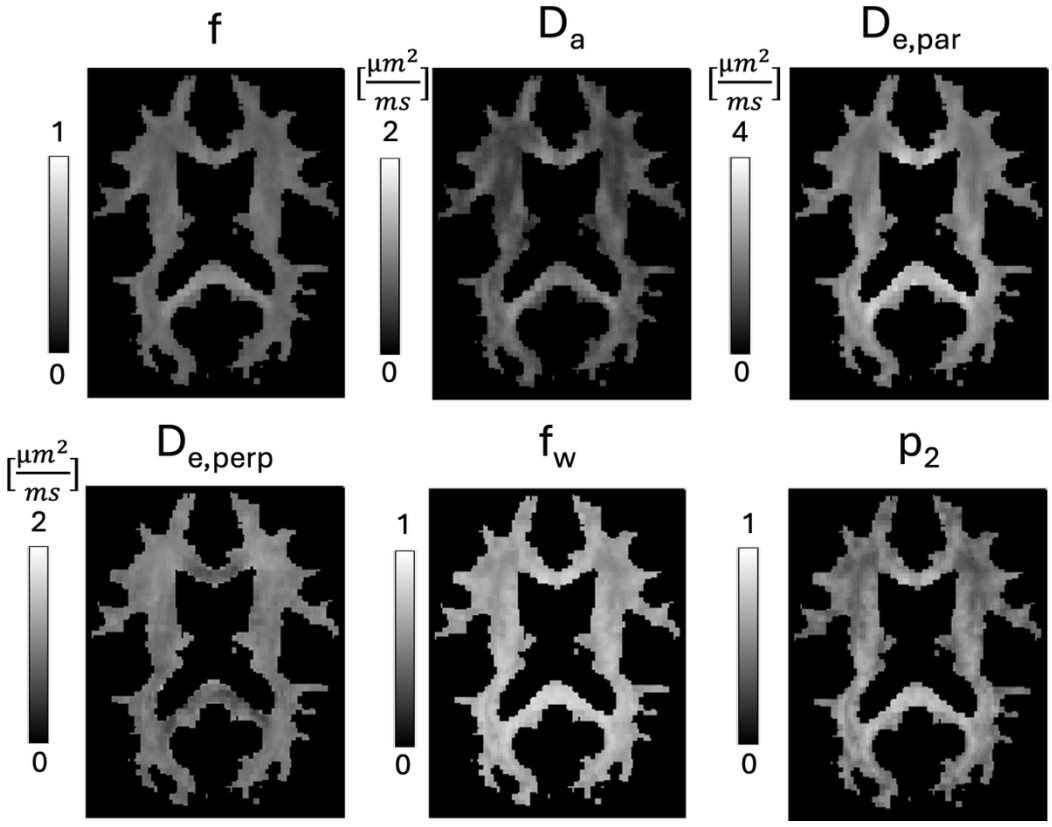


Figure 48: Group mean maps for the estimated WMTI parameter for the four subjects. Upper row: axonal water fraction ($f$), intra-axonal diffusivity ($D_a$), and parallel extra-axonal diffusivity ($D_{e,par}$). Lower row: perpendicular extra-axonal diffusivity $D_{e,perp}$, free water volume fraction ($f_w$), and anisotropy ($p_2$). The maps are mostly homogeneous with slightly higher values in the corpus callosum (except for $D_{e,perp}$).

The across-subject COV (see Figure 47) and group mean maps (see Figure 48) are mostly homogeneous; however, for $D_{e,perp}$, the across-subject COV values are higher and the group mean values are lower in the corpus callosum compared to the other parameter maps, which indicates a higher variability and a possible underestimation in this area.

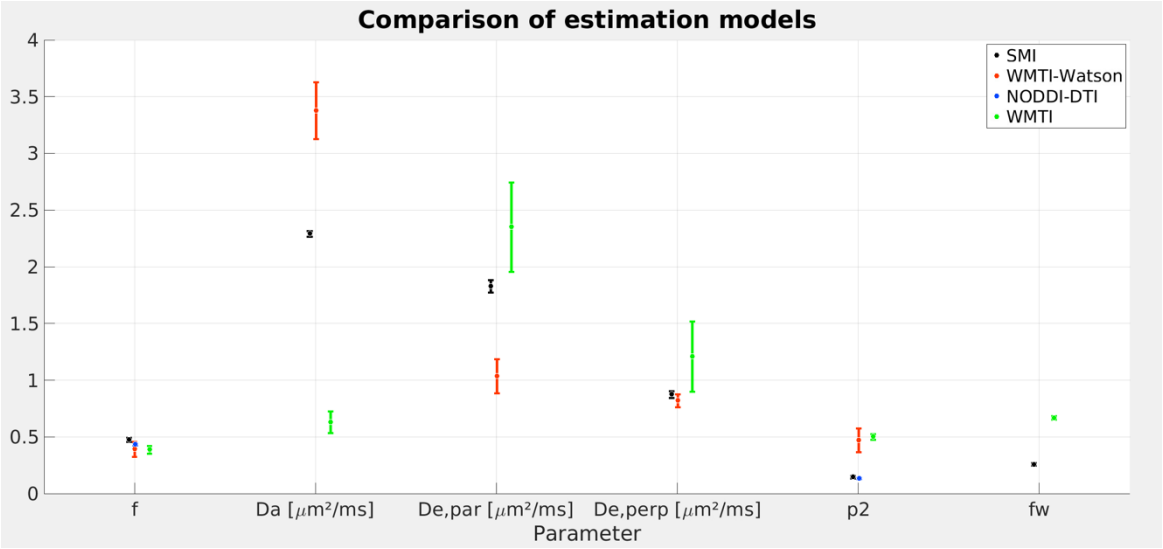


Figure 49: Comparison of the four biophysical parameter estimation models (black: SMI, red: WMTI-Watson, blue: NODDI-DTI, green: WMTI). The mean and standard deviation were computed across white matter voxels (see Figure 32 for the white matter mask) for the following biophysical metrics: axonal water fraction (AWF/$f$), intra-axonal diffusivity ($D_a$), parallel and perpendicular extra-axonal diffusivities ($D_{e,par}$ and $D_{e,perp}$), free water volume fraction ($f_w$), and anisotropy ($p_2$).

As a summary, the comparison of all biophysical parameters is shown in Figure 49. The results indicate parameter-specific dependencies of the biophysical parameters on the estimation method. For example, for the axonal water fraction (AWF/$f$), the estimations are mostly stable across all estimation methods and are similar to the values of WMTI-Watson and NODDI-DTI compared in section 6.3. For the diffusivity parameters, the results show a dependence on the parameter estimation method. The highest discrepancy was found for $D_a$ where WMTI-Watson estimated a diffusivity value of $3.38 \pm 0.25 \frac{\mu m^2}{ms}$ and WMTI a value of $0.63 \pm 0.09 \frac{\mu m^2}{ms}$. To improve the estimation stability for both methods, a solution could be to threshold the ROI for $FA$ values above 0.4 to restrict the analysis on voxels consisting of single fiber orientations, which was done, e.g., in (Benitez et al., 2014). For SMI, the estimated $D_a$ value of $2.29 \pm 0.03 \frac{\mu m^2}{ms}$ is in the range reported by literature for this method

of $2.13 \pm 0.15$ $\frac{\mu m^2}{ms}$ (Table S 1 in (Coelho et al., 2022); the mean over all ROIs was calculated). It has to be noted that the diffusivity estimations for SMI may be biased due to the supervised machine learning regression (Coelho et al., 2022), which might shift the results to the method-specified range/value (Coelho et al., 2021).

The across-subject COV maps indicate homogeneous variations for all subjects. However, for example, the COV was generally increased for the via SMI (Figure 38) estimated parameter $p_2$ and higher in the corpus callosum for the via WMTI-Watson (Figure 44) estimated parameter $D_{e,par}$. The reason for SMI could be that, due to the usage of a data-driven machine learning regression, SMI might not have the best conditions for this specific measurement protocol of this group analysis (Coelho et al., 2022). The WMTI-Watson model contains an additional dispersion parameter compared to WMTI (where this behavior in the corpus callosum was not visible; see Figure 47), which could indicate that the additional degree of freedom might introduce instabilities in this area. Also, a reason could be the influence of cardiac pulsation (resulting in brain motion) during the measurement for this specific region, which was found in (Skare and Andersson, 2001).

For the NODDI-DTI $p_2$ parameter (Figure 41), many voxels could not be estimated, especially in the corpus callosum, and the variance is high for the voxels where NODDI-DTI was able to generate values. A reason for the missing values could be the invalidity of fixed compartmental diffusivities in the NODDI-DTI model (see section 6.2.5).

The registration to the group space was performed using the SPM shoot modules, but there are also other processing pipelines for registration, including post-registration smoothing compensation approaches like “tissue-specific, smoothing-compensated” T-SPOON (Lee et al., 2009) and “voxel-based quantification” VBQ (Draganski et al., 2011), which can be used to compensate for smoothing and partial volume artefacts. These apply a tissue-aware smoothing compensation (T-SPOON), reduce partial volume effects by using tissue classes

(VBQ), and therefore try to reduce blurring/partial volume artefacts. However, as the shoot modules use multiple tissue channels to align the subjects, the inter-subject correspondence is typically high, which reduces the need for post-registration smoothing or partial volume effect correction.

# 7 Discussion

In this section the limitations of the ACID toolbox and possible solutions are discussed in section 7.1. Furthermore, the relevance of ACID for clinical applications and neuroscientific research is described in section 7.2.

## 7.1 Limitations and potential mitigations

The analysis of the three exemplary datasets shows the possibility of ACID to process and analyze in vivo brain, in vivo spinal cord, and ex vivo specimens. However, the performance of each module is dependent on the dataset, which is to be processed, and not in each case do the in-house modules of ACID provide the best result. For example, the first-order eddy currents approximation of ECMOCO was not sufficient for correcting them in the dMRI data of the Human Connectome Project (Van Essen et al., 2012). This limitation of eddy currents correction via ECMOCO was solved by integrating the FSL eddy current and motion correction method eddy. This method corrects dMRI datasets also for higher-order eddy currents (Andersson and Sotiropoulos, 2016), which can become relevant artefacts for dMRI datasets (Andersson and Sotiropoulos, 2016; Rohde et al., 2004). For datasets where HySCO provides not the best results compared to FSL topup (see (Clark et al., 2021) especially Figure 3 for details) and also the “HySCO: combine blip-up and blip-down images” module provides not sufficient results compared to FSL, the FSL method topup is implemented.

These examples show that a found limitation of an ACID module can be solved by implementing a method or approach from another toolbox (e.g., topup from FSL) which can be used to circumvent this limitation.

The mandatory usage of MATLAB and SPM can be seen as a limitation but the benefits of both predominate the disadvantages. So provides the integration in MATLAB and SPM a

whole software and statistical analysis framework. The need of a MATLAB license was made obsolete with the availability of a standalone version.

## 7.2 Relevance for clinical applications and neuroscientific research

The ACID toolbox is not certified and tested for diagnosis in clinical applications. However, there is a growing number of publications which use ACID for scientific studies for which ACID is made. For example, ACID was used in dMRI studies to investigate how multiple sclerosis affects changes in the cerebrum (Deppe et al., 2016a, 2016b; Dossi et al., 2018; Kugler and Deppe, 2018) and also for developments to improve, e.g., the NODDI model in white matter (Alsameen et al., 2023). For spinal cord dMRI analyses, ACID was also used in different studies to, e.g., examine the white matter of the spinal cord after a spinal cord injury (Büeler et al., 2024; David et al., 2022, 2021, 2019; Grabher et al., 2016; Huber et al., 2018; Seif et al., 2020; Vallotton et al., 2021). For an overview of the publicized studies which used ACID, a non-comprehensive list is available on the toolbox website[30]. It is evident that the number of studies using ACID for processing and analyzing dMRI data has increased in the last three years. This trend suggests that the refactoring and extending of ACID has proven its worth, as it is now more widely used by researchers.

[30] http://diffusiontools.com/sidebar/studies-using-acid.html

# 8 Conclusions and outlook

This section provides a summary of key findings that were outcome in this thesis. The findings are sorted regarding software developments (section 8.1), scientific research results (section 8.2), and suggestions and ideas for further investigations and developments (section 8.3).

## 8.1 Summary of key developments

ACID consists of many state-of-the-art preprocessing and modeling methods for dMRI data. Due to its integration into SPM, it benefits from, e.g., statistical analysis methods and a large user community. The now implemented modular organization of the ACID modules provides a flexible and easy-to-update framework. This also solves the possible limitations of ACID modules (see section 7.1 for examples). Also, completely new processing modules can now be integrated easily due to the modular organization, which enables new processing and analysis possibilities for existing ACID analysis pipelines (see section 8.3 for examples). This demonstrates that ACID has now the possibility to stay up to date permanently with the latest scientific findings and not only be state-of-the-art at the time of publication until new scientific methods and algorithms are developed. If limitations are identified, the implementation of alternative or new modules, even from external sources, provides a solution and completely flexible adjustment of pipelines.

The harmonization with the FAIR principles and the compliance with the BIDS standard provide a framework for large analysis studies with many datasets and also enable the comparability with other scientific toolboxes, which often require (especially for deep learning methods, e.g., Clinica) a BIDS-compliant data storage.

Also, new options for specific tissue types were implemented (e.g., new selectable fixed diffusivity values in NODDI-DTI for ex vivo specimens based on literature values, see section 5.4.1 for details) to enable the tissue-specific pipeline creation.

## 8.2 Summary of key findings

Alongside the development of the now reworked ACID toolbox, several analyses were performed. The three pipelines developed for the three tissue types of in vivo brain, in vivo spinal cord, and ex vivo specimen were tested on exemplary datasets and showed the different approaches which have to be implemented into the specific pipeline (e.g., appearance of motion and eddy currents).

Furthermore, for example, the comparison of NODDI-DTI and WMTI-Watson presented in section 6.3 demonstrated the different use cases for each method and how the performance depends on the given dataset. The results implied that the use of WMTI-Watson provided better quality parameter maps if a high SNR dataset (e.g., in vivo brain) was analyzed. In contrast, if a low-SNR dataset (e.g., a spinal cord dataset) was used, WMTI completely failed, whereas NODDI-DTI was able to estimate at least one biophysical parameter with reasonable accuracy.

In section 6.4, the influence of Rician Bias correction was investigated for the exemplary in vivo brain and in vivo spinal cord datasets, comparing the results of NODDI-DTI and WMTI-Watson with and without the use of RBC. The results demonstrate the influence of RBC for biophysical parameter estimation, especially for the Watson concentration parameter ($\kappa$), which was increased for both tissue types.

A comparison of the different denoising methods implemented into ACID was performed (section 6.5). The analysis showed the importance of denoising for low SNR datasets but also pointed out that some denoising methods can introduce a bias for high SNR datasets. Additionally, the results indicated that the parameters benefit not consistently through denoising.

A group analysis over four subjects was performed in section 6.6 to compare the parameter estimation when different analysis methods are used. In addition, it was demonstrated how ACID enables BIDS-compliant data processing and how group analyses benefit from this

advanced data handling. The results indicated a dependency of the estimated biophysical parameters on the different estimation methods. For example, $D_a$ seemed to be overestimated when it was estimated via WMTI-Watson, underestimated if it was estimated via WMTI, and most precisely estimated via SMI. The reason for this model-specific discrepancies could lie in the individual model-specific assumptions (e.g., different numbers of fitting parameters for WMTI and WMTI-Watson or an introduced bias due to the supervised machine learning regression).

## 8.3 Suggestions for future research and further development of ACID

The ACID toolbox now provides a complete framework to pre-process and analyze dMRI datasets. However, due to the modular organization, the implementation of new methods which involve, e.g., phase data could be an interesting opportunity. In ACID, for example, the Real Diffusion Reconstruction method is already implemented, which uses the phase data to extract the "real" part of the complex signal, e.g., to ensure Gaussian noise properties. Also, denoising has become relevant and an actual research topic in dMRI (e.g., (Manzano Patron et al., 2024)). Therefore, new denoising algorithms which use, for example, phase data (e.g., NORDIC (Moeller et al., 2021)) could become relevant and worth to be implemented into ACID.

From the code development side, a reimplementation of ACID from MATLAB to python could become an interesting future project as it would allow the use of ACID without any need for MATLAB. Alternatively, the standalone version of ACID can be used, although it does not allow a direct connection to the used code (compiled black box). However, this change would also require detaching from the SPM framework, which would lead to the loss of the SPM community and additional work for replicating the in ACID used SPM functions and GUI in python.

Another development project could be expanding the test system as it currently checks for the identity of test output and ground truth but not for all option combinations. However, implementing a system that checks all option combinations iteratively would require significant additional work. Before embarking on such an endeavor, it is crucial to determine if the current system is already sufficient, as it ensures general functionality.

# 9 Zusammenfassung auf Englisch

Diffusion MRI (dMRI) has emerged as a significant imaging technique in neuroscience, gaining increasing clinical relevance due to its ability to non-invasively detect diffusion changes in the microstructure. While most research still focuses on the brain, there is an increasing interest in utilizing dMRI to investigate the spinal cord and ex vivo tissue specimens. These types of measurements are particularly relevant for studying spinal cord injuries and validating biophysical models using ex vivo tissues. Also, the scientific use of big data and machine learning applications for investigating, for example, large numbers of dMRI datasets to estimate novel biomarkers by merging all tissue structure information, is becoming increasingly relevant.

In this thesis, a toolbox was developed that is the first to fulfill all these demands of analyzing brain, spinal cord, and ex vivo specimens in a way which is automatable and applicable for big data analyses. This was achieved by adding additional tissue type-specific preprocessing options via code extensions and new modules to an existing brain dMRI analysis toolbox named ACID. Analysis pipelines were created for each type of tissue to provide automated analyses for large numbers of datasets. Additional modules were implemented, which enable ACID to now cover the entire processing chain from raw DICOM data to group-level statistics within a single software package. To implement this in a standardized way, the Brain Imaging Data Structure (BIDS) was integrated into ACID. This ensures compatibility with other BIDS-compliant software and aligns with the growing availability of large databases utilizing the BIDS format. The code structure of ACID was completely reorganized, and the modules of ACID are now fully modularized to enable a flexible and easy-to-extend code framework. The FAIR principles are now harmonized with ACID to fulfill the standards for a valuable and reusable academic software.

Comparisons of several modules and methods (e.g., biophysical parameter estimation methods, influence of Rician bias correction (RBC) on parameter estimation, or denoising methods) were performed to analyze the best module selection in dependence on the acquired tissue type/SNR.

The comparison of the two biophysical models NODDI-DTI and WMTI-Watson showed that NODDI-DTI performs better for spinal cord and WMTI-Watson better for brain datasets, which indicates a SNR dependency for both methods.

The results for the influence of RBC on the estimation of biophysical parameters showed that RBC slightly decreases the mean kurtosis for the brain and spinal cord datasets, which resulted in an increase of the biophysical Watson concentration parameter $\kappa$.

Due to its now implemented modularity, several denoising methods, even from other toolboxes, could be integrated into ACID. Therefore, it was possible to perform a comparison of the now in ACID implemented denoising methods LPCA, MPPCA, and msPOAS, which indicated a general improvement through denoising for low SNR data but no improvement for high SNR data. For msPOAS, even an additional bias became noticeable for high SNR data.

To demonstrate the new in ACID implemented processing workflow starting from raw DICOM data to, e.g., statistical analysis via SPM, an exemplary group analysis of four brain dMRI datasets acquired on the same scanner was performed to compare the implemented

biophysical parameter estimation methods. The results showed that the biophysical parameter estimation is not stable over the different used estimation methods (SMI, NODDI-DTI, WMTI, and WMTI-Watson) in white matter for all parameters. This indicates that the biophysical estimates were dependent on the different model assumptions.

# 10 Zusammenfassung auf Deutsch

Diffusionsgewichtete Magnetresonanzspektroskopie (dMRI) hat sich als signifikante Bildgebungstechnik für Neurowissenschaften erwiesen, welche eine wachsende klinische Relevanz durch die Möglichkeit, nicht-invasiv Diffusionsänderungen in Mikrostrukturen zu detektieren, erhält. Während sich die meiste Forschung nur auf das Gehirn fokussiert, erfährt die Untersuchung von Rückenmark und ex vivo Proben mittels dMRI ein wachsendes Interesse. Diese Arten von Messungen sind insbesondere interessant, um Verletzungen des Rückenmarks zu untersuchen oder zur Validierung von biophysikalischen Modellen mittels ex vivo Gewebe. Auch der wissenschaftliche Nutzen für „Big Data“ und maschinelles Lernen zur Untersuchung von beispielsweise großen dMRI-Datensätzen zur Bestimmung von neuartigen Biomarkern durch das Kombinieren aller Gewebeinformationen erfährt eine zunehmende Relevanz.

In dieser Doktorarbeit wurde eine Toolbox entwickelt, welche als erste all diese Anforderungen zur automatisierbaren und für „Big Data“ nutzbaren Analyse von Gehirn, Rückenmark und ex vivo Proben erfüllt. Dies wurde erreicht durch das Hinzufügen von gewebetypspezifischen Vor-Verarbeitungsoptionen durch Erweiterungen des Codes und das Hinzufügen neuer Module in eine bereits existierende Gehirn dMRI Toolbox namens ACID. Analyse Pipelines wurden für jeden Gewebetyp generiert, um eine automatisierte Analyse von großen Datensätzen zu ermöglichen. Zusätzliche Module wurden integriert, damit ACID die vollständige Datenverarbeitungskette von DICOM Rohdaten zu Gruppenstatistik innerhalb eines einzigen Softwarepaketes anbieten kann. Um dies in einer standardisierten Weise zu ermöglichen, wurde die Brain Imaging Data Structure (BIDS) in ACID integriert. Dies stellt eine Kompatibilität zu anderer BIDS konformer Software sicher und ermöglicht, dass ACID damit zu der wachsenden Zahl an großen Datenbanken kompatibel ist, die den BIDS-Standard nutzen. Die Codestruktur von ACID wurde vollständig reorganisiert und die Module von ACID wurden vollständig modularisiert, um eine flexible und einfach zu erweiternde Codeumgebung zu ermöglichen. Die FAIR Prinzipien wurden mit ACID harmonisiert, um den Standard einer nützlichen und wiederverwendbaren akademischen Software zu erfüllen.

Es wurden Vergleiche verschiedener Module und Methoden durchgeführt (bspw. Methoden zur Bestimmung biophysikalischer Parameter, Einfluss der Rician-Bias-Korrektur (RBC) auf die Parameterbestimmung oder ein Vergleich von verschiedenen Entrauschungsmethoden), um zu analysieren, welches Modul die beste Wahl darstellt, in Abhängigkeit des Gewebetyps und/oder SNR.

Der Vergleich der beiden biophysikalischen Methoden NODDI-DTI und WMTI-Watson zeigte, dass NODDI-DTI bessere Ergebnisse für Rückenmarksdaten lieferte, während WMTI-Watson bessere Ergebnisse für Gehirndaten zeigte. Dies deutet auf eine SNR-Abhängigkeit beider Methoden hin.

Die Ergebnisse für den Einfluss der Rician-Bias-Korrektur (RBC) auf die Bestimmung von biophysikalischen Parametern zeigten, dass RBC die Werte der mittleren Kurtosis für Gehirn- und Rückenmarksdaten leicht senkte, was in einer Erhöhung des biophysikalischen Watson-Konzentrationsparameters $\kappa$ resultierte.

Aufgrund der nun implementierten Modularität konnten verschiedene Entrauschungsmethoden (sogar von anderen Toolboxen) in ACID integriert werden. Daher war es möglich, einen Vergleich aller nun in ACID integrierten Entrauschungsmethoden (LPCA, MPPCA und msPOAS) durchzuführen, welcher einen generellen Nutzen für Datensätze mit niedrigem SNR, aber keinen Nutzen für Datensätze mit hohem SNR aufzeigte. Für msPOAS wurde ein zusätzlicher Bias für Datensätze mit hohem SNR sichtbar. Um den in ACID neu implementierten Arbeitsablauf, beginnend bei den DICOM Rohdaten bis zu bspw. statistischen Analysen mittels SPM, zu demonstrieren, wurde eine beispielhafte Gruppenanalyse für vier Gehirn-dMRI Datensätze, welche am selben Scanner aufgenommen wurden, durchgeführt, um ein Vergleich der implementierten biophysikalischen Parameterbestimmungsmethoden durchzuführen. Die Ergebnisse zeigten, dass die biophysikalische Parameterbestimmung nicht stabil über alle untersuchten Methoden (DKI, SMI, NODDI-DTI, WMTI und WMTI-Watson) und Parameter in weißer Gehirnsubstanz war. Dies deutet darauf hin, dass die biophysikalischen Schätzungen in Abhängigkeit zu den verschiedenen Modellannahmen stehen.

# 11 List of abbreviations

- ACID A Comprehensive Toolbox for Image Processing and Modeling of Brain, Spinal Cord, and Ex Vivo Diffusion MRI Data
- $AD$ Axial Diffusivity
- $AK$ Axial Kurtosis
- $AW$ Axial Kurtosis Tensor
- $AWF/f$ Axonal Water Fraction
- BIDS Brain Imaging Data Structure
- COV coefficient of variation
- $D_a$ Intra-axonal Diffusivity
- $D_{e,par}$ Parallel Extra-axonal Diffusivity
- $D_{e,perp}$ Perpendicular Extra-axonal Diffusivity
- DKI Diffusion Kurtosis Imaging
- dMRI diffusion Magnetic Resonance Imaging
- DTI Diffusion Tensor Imaging
- DWI Diffusion Weighted Imaging
- EC Eddy Currents
- ECMOCO Eddy-Current and Motion Correction
- $FA$ Fractional Anisotropy
- FOV Field Of View
- FSL FMRIB Software Library
- GUI Graphical User Interface
- HF High frequency
- HySCO Hyperelastic Susceptibility Artifact Correction

- $\kappa$ Watson Concentration Parameter
- LPCA Local Principal Component Analysis
- $MD$ Mean Diffusivity
- $MK$ Mean Kurtosis
- MP-PCA Marchenko-Pastur Principal Component Analysis
- msPOAS Multi-shell Position-Orientation Adaptive Smoothing
- $MW$ Mean Kurtosis Tensor
- NLLS Non-linear Least Squares
- NODDI Neurite Orientation Dispersion and Density
- ODI Orientation Dispersion Index
- OLS Ordinary Least Squares
- $p_2$ Anisotropy
- RBC Rician Bias Correction
- $RD$ Radial Diffusivity
- RF Radio frequency
- $RK$ Radial Kurtosis
- ROI Region of interest
- $RW$ Radial Kurtosis Tensor
- SMI Standard Model Imaging
- SNR Signal-to-Noise Ratio
- SPM Statistical Parametric Mapping
- TE Echo Time
- WLS Weighted Least Squares
- WMTI-Watson White Matter Tract Integrity - Watson

## 12 Tools

DeepL, was used for the following purpose:

- Grammar and spelling checks

Apple Intelligence (MacBook M1), was used for the following purposes:

- Improving sentences and passages for their readability and flow
- Grammar and spelling checks

ChatGPT version 5, OpenAI (https://chatgpt.com), was used for the following purposes:

- Creating code and caption for Figure 7
- Literature search

## 13 References


Absinta, M., Nair, G., Filippi, M., Ray-Chaudhury, A., Reyes-Mantilla, M.I., Pardo, C.A., Reich, D.S., 2014. Postmortem Magnetic Resonance Imaging to Guide the Pathological Cut: Individualized, 3D-Printed Cutting Boxes for Fixed Brains. J. Neuropathol. Exp. Neurol. 73, 780–788. https://doi.org/10.1097/NEN.0000000000000096

Ades-Aron, B., Veraart, J., Kochunov, P., McGuire, S., Sherman, P., Kellner, E., Novikov, D.S., Fieremans, E., 2018. Evaluation of the accuracy and precision of the diffusion parameter EStImation with Gibbs and NoisE removal pipeline. NeuroImage 183, 532–543. https://doi.org/10.1016/j.neuroimage.2018.07.066

Aja-Fernández, S., Vegas-Sánchez-Ferrero, G., Tristán-Vega, A., 2014. Noise estimation in parallel MRI: GRAPPA and SENSE. Magn. Reson. Imaging 32, 281–290. https://doi.org/10.1016/j.mri.2013.12.001

Alexander, D.C., Dyrby, T.B., Nilsson, M., Zhang, H., 2019. Imaging brain microstructure with diffusion MRI: practicality and applications. NMR Biomed. 32, e3841. https://doi.org/10.1002/nbm.3841

Alsameen, M.H., Gong, Z., Qian, W., Kiely, M., Triebswetter, C., Bergeron, C.M., Cortina, L.E., Faulkner, M.E., Laporte, J.P., Bouhrara, M., 2023. C-NODDI: a constrained NODDI model for axonal density and orientation determinations in cerebral white matter. Front. Neurol. 14. https://doi.org/10.3389/fneur.2023.1205426

Andersson, J.L.R., Sotiropoulos, S.N., 2016. An integrated approach to correction for off-resonance effects and subject movement in diffusion MR imaging. NeuroImage 125, 1063–1078. https://doi.org/10.1016/j.neuroimage.2015.10.019

Andersson, M., Pizzolato, M., Kjer, H.M., Skodborg, K.F., Lundell, H., Dyrby, T.B., 2022. Does powder averaging remove dispersion bias in diffusion MRI diameter estimates within real 3D axonal architectures? NeuroImage 248, 118718. https://doi.org/10.1016/j.neuroimage.2021.118718

André, E.D., Grinberg, F., Farrher, E., Maximov, I.I., Shah, N.J., Meyer, C., Jaspar, M., Muto, V., Phillips, C., Balteau, E., 2014. Influence of Noise Correction on Intra- and

Inter-Subject Variability of Quantitative Metrics in Diffusion Kurtosis Imaging. PLoS ONE 9, e94531. https://doi.org/10.1371/journal.pone.0094531
Ashburner, J., Friston, K.J., 2011. Diffeomorphic registration using geodesic shooting and Gauss–Newton optimisation. NeuroImage 55, 954–967. https://doi.org/10.1016/j.neuroimage.2010.12.049
Ashburner, J., Friston, K.J., 2005. Unified segmentation. NeuroImage 26, 839–851. https://doi.org/10.1016/j.neuroimage.2005.02.018
Barazany, D., Basser, P.J., Assaf, Y., 2009. In vivo measurement of axon diameter distribution in the corpus callosum of rat brain. Brain 132, 1210–1220. https://doi.org/10.1093/brain/awp042
Barker, G.J., 2001. Diffusion-weighted imaging of the spinal cord and optic nerve. J. Neurol. Sci. 186, S45–S49. https://doi.org/10.1016/S0022-510X(01)00490-7
Barker, M., Chue Hong, N.P., Katz, D.S., Lamprecht, A.-L., Martinez-Ortiz, C., Psomopoulos, F., Harrow, J., Castro, L.J., Gruenpeter, M., Martinez, P.A., Honeyman, T., 2022. Introducing the FAIR Principles for research software. Sci. Data 9, 622. https://doi.org/10.1038/s41597-022-01710-x
Basser, P.J., Mattiello, J., Lebihan, D., 1994. Estimation of the Effective Self-Diffusion *Tensor* from the NMR Spin Echo. J. Magn. Reson. B 103, 247–254. https://doi.org/10.1006/jmrb.1994.1037
Basser, P.J., Pajevic, S., 2000. Statistical artifacts in diffusion tensor MRI (DT-MRI) caused by background noise. Magn. Reson. Med. 44, 41–50. https://doi.org/10.1002/1522-2594(200007)44:1%253C41::AID-MRM8%253E3.0.CO;2-O
Becker, S.M.A., Tabelow, K., Mohammadi, S., Weiskopf, N., Polzehl, J., 2014. Adaptive smoothing of multi-shell diffusion weighted magnetic resonance data by msPOAS. NeuroImage 95, 90–105. https://doi.org/10.1016/j.neuroimage.2014.03.053
Becker, S.M.A., Tabelow, K., Voss, H.U., Anwander, A., Heidemann, R.M., Polzehl, J., 2012. Position-orientation adaptive smoothing of diffusion weighted magnetic resonance data (POAS). Med. Image Anal. 16, 1142–1155. https://doi.org/10.1016/j.media.2012.05.007
Benitez, A., Fieremans, E., Jensen, J.H., Falangola, M.F., Tabesh, A., Ferris, S.H., Helpern, J.A., 2014. White matter tract integrity metrics reflect the vulnerability of late-myelinating tracts in Alzheimer's disease. NeuroImage Clin. 4, 64–71. https://doi.org/10.1016/j.nicl.2013.11.001
Büeler, S., Freund, P., Kessler, T.M., Liechti, M.D., David, G., 2024. Improved inter-subject alignment of the lumbosacral cord for group-level in vivo gray and white matter assessments: A scan-rescan MRI study at 3T. PLOS ONE 19, e0301449. https://doi.org/10.1371/journal.pone.0301449
Callaghan, P.T., Eccles, C.D., Xia, Y., 1988. NMR microscopy of dynamic displacements: k-space and q-space imaging. J. Phys. [E] 21, 820–822. https://doi.org/10.1088/0022-3735/21/8/017
Caruyer, E., Lenglet, C., Sapiro, G., Deriche, R., 2013. Design of multishell sampling schemes with uniform coverage in diffusion MRI. Magn. Reson. Med. 69, 1534–1540. https://doi.org/10.1002/mrm.24736
Clark, I.A., Callaghan, M.F., Weiskopf, N., Maguire, E.A., Mohammadi, S., 2021. Reducing Susceptibility Distortion Related Image Blurring in Diffusion MRI EPI Data. Front. Neurosci. 15, 706473. https://doi.org/10.3389/fnins.2021.706473
Coelho, S., Baete, S.H., Lemberskiy, G., Ades-Aron, B., Barrol, G., Veraart, J., Novikov, D.S., Fieremans, E., 2022. Reproducibility of the Standard Model of diffusion in white matter on clinical MRI systems. NeuroImage 257, 119290. https://doi.org/10.1016/j.neuroimage.2022.119290

Coelho, S., Fieremans, E., Novikov, D., 2021. How do we know we measure tissue parameters, not the prior?, in: ISMRM2021. Presented at the ISMRM2021.

Cohen, Y., Anaby, D., Morozov, D., 2017. Diffusion MRI of the spinal cord: from structural studies to pathology. NMR Biomed. 30, e3592. https://doi.org/10.1002/nbm.3592

Constantinides, C.D., Atalar, E., McVeigh, E., 1997. Signal-to-noise measurements in magnitude images from NMR phased arrays, in: Proceedings of the 19th Annual International Conference of the IEEE Engineering in Medicine and Biology Society. "Magnificent Milestones and Emerging Opportunities in Medical Engineering" (Cat. No.97CH36136). Presented at the the 19th Annual International Conference of the IEEE Engineering in Medicine and Biology Society. "Magnificent Milestones and Emerging Opportunities in Medical Engineering" (Cat. No.97CH36136), pp. 456–459 vol.1. https://doi.org/10.1109/IEMBS.1997.754578

David, G., Freund, P., Mohammadi, S., 2017. The efficiency of retrospective artifact correction methods in improving the statistical power of between-group differences in spinal cord DTI. NeuroImage 158, 296–307. https://doi.org/10.1016/j.neuroimage.2017.06.051

David, G., Fricke, B., Oeschger, J.M., Ruthotto, L., Fritz, F.J., Ohana, O., Mordhorst, L., Sauvigny, T., Freund, P., Tabelow, K., Mohammadi, S., 2024. ACID: A Comprehensive Toolbox for Image Processing and Modeling of Brain, Spinal Cord, and Ex Vivo Diffusion MRI Data. Imaging Neurosci. https://doi.org/10.1162/imag_a_00288

David, G., Pfyffer, D., Vallotton, K., Pfender, N., Thompson, A., Weiskopf, N., Mohammadi, S., Curt, A., Freund, P., 2021. Longitudinal changes of spinal cord grey and white matter following spinal cord injury. J. Neurol. Neurosurg. Psychiatry 92, 1222–1230. https://doi.org/10.1136/jnnp-2021-326337

David, G., Seif, M., Huber, E., Hupp, M., Rosner, J., Dietz, V., Weiskopf, N., Mohammadi, S., Freund, P., 2019. In vivo evidence of remote neural degeneration in the lumbar enlargement after cervical injury. Neurology 92. https://doi.org/10.1212/WNL.0000000000007137

David, G., Vallotton, K., Hupp, M., Curt, A., Freund, P., Seif, M., 2022. Extent of Cord Pathology in the Lumbosacral Enlargement in Non-Traumatic versus Traumatic Spinal Cord Injury. J. Neurotrauma 39, 639–650. https://doi.org/10.1089/neu.2021.0389

Deppe, M., Krämer, J., Tenberge, J.-G., Marinell, J., Schwindt, W., Deppe, K., Groppa, S., Wiendl, H., Meuth, S.G., 2016a. Early silent microstructural degeneration and atrophy of the thalamocortical network in multiple sclerosis. Hum. Brain Mapp. 37, 1866–1879. https://doi.org/10.1002/hbm.23144

Deppe, M., Tabelow, K., Krämer, J., Tenberge, J.-G., Schiffler, P., Bittner, S., Schwindt, W., Zipp, F., Wiendl, H., Meuth, S.G., 2016b. Evidence for early, non-lesional cerebellar damage in patients with multiple sclerosis: DTI measures correlate with disability, atrophy, and disease duration. Mult. Scler. J. 22, 73–84. https://doi.org/10.1177/1352458515579439

Dietrich, O., Raya, J.G., Reeder, S.B., Reiser, M.F., Schoenberg, S.O., 2007. Measurement of signal-to-noise ratios in MR images: Influence of multichannel coils, parallel imaging, and reconstruction filters. J. Magn. Reson. Imaging 26, 375–385. https://doi.org/10.1002/jmri.20969

Dössel, O., 2016. Bildgebende Verfahren in der Medizin. Springer Berlin Heidelberg, Berlin, Heidelberg. https://doi.org/10.1007/978-3-642-54407-1

Dossi, D.E., Chaves, H., Heck, E.S., Rodriguez Murúa, S., Ventrice, F., Bakshi, R., Quintana, F.J., Correale, J., Farez, M.F., 2018. Effects of Systolic Blood Pressure on

Brain Integrity in Multiple Sclerosis. Front. Neurol. 9. https://doi.org/10.3389/fneur.2018.00487
Draganski, B., Ashburner, J., Hutton, C., Kherif, F., Frackowiak, R.S.J., Helms, G., Weiskopf, N., 2011. Regional specificity of MRI contrast parameter changes in normal ageing revealed by voxel-based quantification (VBQ). NeuroImage 55, 1423–1434. https://doi.org/10.1016/j.neuroimage.2011.01.052
Dubois, J., Dehaene-Lambertz, G., Kulikova, S., Poupon, C., Hüppi, P.S., Hertz-Pannier, L., 2014. The early development of brain white matter: A review of imaging studies in fetuses, newborns and infants. Neuroscience 276, 48–71. https://doi.org/10.1016/j.neuroscience.2013.12.044
Edwards, L.J., Pine, K.J., Ellerbrock, I., Weiskopf, N., Mohammadi, S., 2017. NODDI-DTI: Estimating Neurite Orientation and Dispersion Parameters from a Diffusion Tensor in Healthy White Matter. Front. Neurosci. 11, 720. https://doi.org/10.3389/fnins.2017.00720
Eichner, C., Cauley, S.F., Cohen-Adad, J., Möller, H.E., Turner, R., Setsompop, K., Wald, L.L., 2015. Real diffusion-weighted MRI enabling true signal averaging and increased diffusion contrast. NeuroImage 122, 373–384. https://doi.org/10.1016/j.neuroimage.2015.07.074
Einstein, A., 1956. Investigations on the Theory of the Brownian Movement. Courier Corporation.
Fan, Q., Nummenmaa, A., Witzel, T., Ohringer, N., Tian, Q., Setsompop, K., Klawiter, E.C., Rosen, B.R., Wald, L.L., Huang, S.Y., 2020. Axon diameter index estimation independent of fiber orientation distribution using high-gradient diffusion MRI. NeuroImage 222, 117197. https://doi.org/10.1016/j.neuroimage.2020.117197
Fieremans, E., Jensen, J.H., Helpern, J.A., 2011. White matter characterization with diffusional kurtosis imaging. NeuroImage 58, 177–188. https://doi.org/10.1016/j.neuroimage.2011.06.006
Fricke, B., 2020. Chemical-Shift Imaging mit 2D-ortsselektiven Hochfrequenz-Anregungen (Masterarbeit). Universität Hamburg, Hamburg.
Gorgolewski, K.J., Auer, T., Calhoun, V.D., Craddock, R.C., Das, S., Duff, E.P., Flandin, G., Ghosh, S.S., Glatard, T., Halchenko, Y.O., Handwerker, D.A., Hanke, M., Keator, D., Li, X., Michael, Z., Maumet, C., Nichols, B.N., Nichols, T.E., Pellman, J., Poline, J.-B., Rokem, A., Schaefer, G., Sochat, V., Triplett, W., Turner, J.A., Varoquaux, G., Poldrack, R.A., 2016. The brain imaging data structure, a format for organizing and describing outputs of neuroimaging experiments. Sci. Data 3, 160044. https://doi.org/10.1038/sdata.2016.44
Grabher, P., Mohammadi, S., Trachsler, A., Friedl, S., David, G., Sutter, R., Weiskopf, N., Thompson, A.J., Curt, A., Freund, P., 2016. Voxel-based analysis of grey and white matter degeneration in cervical spondylotic myelopathy. Sci. Rep. 6, 24636. https://doi.org/10.1038/srep24636
Griffiths, D.J., 2013. Introduction to electrodynamics, 4. ed., international ed. ed, Always learning. Pearson, Boston.
Grussu, F., Schneider, T., Tur, C., Yates, R.L., Tachrount, M., Ianu, A., DeLuca, G.C., 2017. Neurite dispersion: a new marker of multiple sclerosis spinal cord pathology?
Gu, X., Eklund, A., 2019. Evaluation of Six Phase Encoding Based Susceptibility Distortion Correction Methods for Diffusion MRI. Front. Neuroinformatics 13. https://doi.org/10.3389/fninf.2019.00076
Gudbjartsson, H., Patz, S., 1995. The rician distribution of noisy mri data. Magn. Reson. Med. 34, 910–914. https://doi.org/10.1002/mrm.1910340618

Hansen, B., Shemesh, N., Jespersen, S.N., 2016. Fast imaging of mean, axial and radial diffusion kurtosis. NeuroImage 142, 381–393. https://doi.org/10.1016/j.neuroimage.2016.08.022

Haselgrove, J.C., Moore, J.R., 1996. Correction for distortion of echo-planar images used to calculate the apparent diffusion coefficient. Magn. Reson. Med. 36, 960–964. https://doi.org/10.1002/mrm.1910360620

Howard, A.F., Cottaar, M., Drakesmith, M., Fan, Q., Huang, S.Y., Jones, D.K., Lange, F.J., Mollink, J., Rudrapatna, S.U., Tian, Q., Miller, K.L., Jbabdi, S., 2022. Estimating axial diffusivity in the NODDI model. NeuroImage 262, 119535. https://doi.org/10.1016/j.neuroimage.2022.119535

Huber, E., David, G., Thompson, A.J., Weiskopf, N., Mohammadi, S., Freund, P., 2018. Dorsal and ventral horn atrophy is associated with clinical outcome after spinal cord injury. Neurology 90, e1510–e1522. https://doi.org/10.1212/WNL.0000000000005361

Jelescu, I.O., Palombo, M., Bagnato, F., Schilling, K.G., 2020. Challenges for biophysical modeling of microstructure. J. Neurosci. Methods 344, 108861. https://doi.org/10.1016/j.jneumeth.2020.108861

Jenkinson, M., Beckmann, C.F., Behrens, T.E.J., Woolrich, M.W., Smith, S.M., 2012. FSL. NeuroImage 62, 782–790. https://doi.org/10.1016/j.neuroimage.2011.09.015

Jensen, J.H., Helpern, J.A., Ramani, A., Lu, H., Kaczynski, K., 2005. Diffusional kurtosis imaging: The quantification of non-gaussian water diffusion by means of magnetic resonance imaging. Magn. Reson. Med. 53, 1432–1440. https://doi.org/10.1002/mrm.20508

Jespersen, S.N., Olesen, J.L., Hansen, B., Shemesh, N., 2018. Diffusion time dependence of microstructural parameters in fixed spinal cord. NeuroImage 182, 329–342. https://doi.org/10.1016/j.neuroimage.2017.08.039

Jezzard, P., Barnett, A.S., Pierpaoli, C., 1998. Characterization of and correction for eddy current artifacts in echo planar diffusion imaging. Magn. Reson. Med. 39, 801–812. https://doi.org/10.1002/mrm.1910390518

Jones, D.K., Basser, P.J., 2004. “Squashing peanuts and smashing pumpkins”: How noise distorts diffusion-weighted MR data. Magn. Reson. Med. 52, 979–993. https://doi.org/10.1002/mrm.20283

Karakuzu, A., Appelhoff, S., Auer, T., Boudreau, M., Feingold, F., Khan, A.R., Lazari, A., Markiewicz, C., Mulder, M., Phillips, C., Salo, T., Stikov, N., Whitaker, K., de Hollander, G., 2022. qMRI-BIDS: An extension to the brain imaging data structure for quantitative magnetic resonance imaging data. Sci. Data 9, 517. https://doi.org/10.1038/s41597-022-01571-4

Kellner, E., Dhital, B., Kiselev, V.G., Reisert, M., 2016. Gibbs-ringing artifact removal based on local subvoxel-shifts. Magn. Reson. Med. 76, 1574–1581. https://doi.org/10.1002/mrm.26054

Kelm, N.D., West, K.L., Carson, R.P., Gochberg, D.F., Ess, K.C., Does, M.D., 2016. Evaluation of diffusion kurtosis imaging in ex vivo hypomyelinated mouse brains. NeuroImage 124, 612–626. https://doi.org/10.1016/j.neuroimage.2015.09.028

Kiselev, V.G., 2017. Fundamentals of diffusion MRI physics: Fundamentals of Diffusion MRI Physics. NMR Biomed. 30, e3602. https://doi.org/10.1002/nbm.3602

Koay, C.G., Basser, P.J., 2006. Analytically exact correction scheme for signal extraction from noisy magnitude MR signals. J. Magn. Reson. 179, 317–322. https://doi.org/10.1016/j.jmr.2006.01.016

Koay, C.G., Chang, L.-C., Carew, J.D., Pierpaoli, C., Basser, P.J., 2006. A unifying theoretical and algorithmic framework for least squares methods of estimation in

diffusion tensor imaging. J. Magn. Reson. 182, 115–125. https://doi.org/10.1016/j.jmr.2006.06.020
Kugler, A.V., Deppe, M., 2018. Non-lesional cerebellar damage in patients with clinically isolated syndrome: DTI measures predict early conversion into clinically definite multiple sclerosis. NeuroImage Clin. 19, 633–639. https://doi.org/10.1016/j.nicl.2018.04.028
Le Bihan, D., Breton, E., Lallemand, D., Aubin, M.L., Vignaud, J., Laval-Jeantet, M., 1988. Separation of diffusion and perfusion in intravoxel incoherent motion MR imaging. Radiology 168, 497–505. https://doi.org/10.1148/radiology.168.2.3393671
Lee, J.E., Chung, M.K., Lazar, M., DuBray, M.B., Kim, J., Bigler, E.D., Lainhart, J.E., Alexander, A.L., 2009. A study of diffusion tensor imaging by tissue-specific, smoothing-compensated voxel-based analysis. NeuroImage 44, 870–883. https://doi.org/10.1016/j.neuroimage.2008.09.041
Li, Y., Edalati, M., Du, X., Wang, H., Cao, J.J., 2018. Self-calibrated correlation imaging with k-space variant correlation functions: Correlation Imaging. Magn. Reson. Med. 79, 1483–1494. https://doi.org/10.1002/mrm.26818
Liang, Z.-P., Lauterbur, P.C., 2000. Principles of Magnetic Resonance Imaging: A Signal Processing Perspective | IEEE eBooks | IEEE Xplore.
Macdonald, J., Ruthotto, L., 2018. Improved Susceptibility Artifact Correction of Echo-Planar MRI using the Alternating Direction Method of Multipliers. J. Math. Imaging Vis. 60, 268–282. https://doi.org/10.1007/s10851-017-0757-x
Mangin, J.-F., Poupon, C., Clark, C., Le Bihan, D., Bloch, I., 2002. Distortion correction and robust tensor estimation for MR diffusion imaging. Med. Image Anal. 6, 191–198. https://doi.org/10.1016/S1361-8415(02)00079-8
Manjón, J.V., Coupé, P., Concha, L., Buades, A., Collins, D.L., Robles, M., 2013. Diffusion Weighted Image Denoising Using Overcomplete Local PCA. PLoS ONE 8, e73021. https://doi.org/10.1371/journal.pone.0073021
Manzano Patron, J.P., Moeller, S., Andersson, J.L.R., Ugurbil, K., Yacoub, E., Sotiropoulos, S.N., 2024. Denoising diffusion MRI: Considerations and implications for analysis. Imaging Neurosci. 2, 1–29. https://doi.org/10.1162/imag_a_00060
Martin, A.R., Aleksanderek, I., Cohen-Adad, J., Tarmohamed, Z., Tetreault, L., Smith, N., Cadotte, D.W., Crawley, A., Ginsberg, H., Mikulis, D.J., Fehlings, M.G., 2016. Translating state-of-the-art spinal cord MRI techniques to clinical use: A systematic review of clinical studies utilizing DTI, MT, MWF, MRS, and fMRI. NeuroImage Clin. 10, 192–238. https://doi.org/10.1016/j.nicl.2015.11.019
Meschede, D. (Ed.), 2010. Gerthsen Physik, Springer-Lehrbuch. Springer Berlin Heidelberg, Berlin, Heidelberg. https://doi.org/10.1007/978-3-642-12894-3
Miller, A.J., Joseph, P.M., 1993. The use of power images to perform quantitative analysis on low SNR MR images. Magn. Reson. Imaging 11, 1051–1056. https://doi.org/10.1016/0730-725X(93)90225-3
Miller, S.P., Vigneron, D.B., Henry, R.G., Bohland, M.A., Ceppi-Cozzio, C., Hoffman, C., Newton, N., Partridge, J.C., Ferriero, D.M., Barkovich, A.J., 2002. Serial quantitative diffusion tensor MRI of the premature brain: Development in newborns with and without injury. J. Magn. Reson. Imaging 16, 621–632. https://doi.org/10.1002/jmri.10205
Modersitzki, J., 2009. FAIR. Society for Industrial and Applied Mathematics. https://doi.org/10.1137/1.9780898718843
Moeller, S., Pisharady, P.K., Ramanna, S., Lenglet, C., Wu, X., Dowdle, L., Yacoub, E., Uğurbil, K., Akçakaya, M., 2021. NOise reduction with DIstribution Corrected (NORDIC) PCA in dMRI with complex-valued parameter-free locally low-rank

processing. NeuroImage 226, 117539. https://doi.org/10.1016/j.neuroimage.2020.117539
Mohammadi, S., Callaghan, M.F., 2021. Towards in vivo g-ratio mapping using MRI: Unifying myelin and diffusion imaging. J. Neurosci. Methods 348, 108990. https://doi.org/10.1016/j.jneumeth.2020.108990
Mohammadi, S., Freund, P., Feiweier, T., Curt, A., Weiskopf, N., 2013. The impact of post-processing on spinal cord diffusion tensor imaging. NeuroImage 70, 377–385. https://doi.org/10.1016/j.neuroimage.2012.12.058
Mohammadi, S., Möller, H.E., Kugel, H., Müller, D.K., Deppe, M., 2010. Correcting eddy current and motion effects by affine whole-brain registrations: Evaluation of three-dimensional distortions and comparison with slicewise correction. Magn. Reson. Med. 64, 1047–1056. https://doi.org/10.1002/mrm.22501
Mohammadi, S., Tabelow, K., Ruthotto, L., Feiweier, T., Polzehl, J., Weiskopf, N., 2015. High-resolution diffusion kurtosis imaging at 3T enabled by advanced post-processing. Front. Neurosci. 8. https://doi.org/10.3389/fnins.2014.00427
Mollink, J., Kleinnijenhuis, M., Cappellen Van Walsum, A.-M.V., Sotiropoulos, S.N., Cottaar, M., Mirfin, C., Heinrich, M.P., Jenkinson, M., Pallebage-Gamarallage, M., Ansorge, O., Jbabdi, S., Miller, K.L., 2017. Evaluating fibre orientation dispersion in white matter: Comparison of diffusion MRI, histology and polarized light imaging. NeuroImage 157, 561–574. https://doi.org/10.1016/j.neuroimage.2017.06.001
Novikov, D.S., Fieremans, E., Jespersen, S.N., Kiselev, V.G., 2019. Quantifying brain microstructure with diffusion MRI: Theory and parameter estimation. NMR Biomed. 32, e3998. https://doi.org/10.1002/nbm.3998
Novikov, D.S., Veraart, J., Jelescu, I.O., Fieremans, E., 2018. Rotationally-invariant mapping of scalar and orientational metrics of neuronal microstructure with diffusion MRI. NeuroImage 174, 518–538. https://doi.org/10.1016/j.neuroimage.2018.03.006
Oeschger, J.M., Tabelow, K., Mohammadi, S., 2023a. Axisymmetric diffusion kurtosis imaging with Rician bias correction: A simulation study. Magn. Reson. Med. 89, 787–799. https://doi.org/10.1002/mrm.29474
Oeschger, J.M., Tabelow, K., Mohammadi, S., 2023b. Investigating apparent differences between standard DKI and axisymmetric DKI and its consequences for biophysical parameter estimates (preprint). Biophysics. https://doi.org/10.1101/2023.06.21.545891
Papazoglou, S., Ashtarayeh, M., Oeschger, J.M., Callaghan, M.F., Does, M.D., Mohammadi, S., 2024. Insights and improvements in correspondence between axonal volume fraction measured with diffusion-weighted MRI and electron microscopy. NMR Biomed. 37, e5070. https://doi.org/10.1002/nbm.5070
Penny, W.D., Friston, K.J., Ashburner, J.T., Kiebel, S.J., Nichols, T.E., 2011. Statistical Parametric Mapping: The Analysis of Functional Brain Images. Elsevier.
Polzehl, J., Tabelow, K., 2016. Low SNR in Diffusion MRI Models. J. Am. Stat. Assoc. 111, 1480–1490. https://doi.org/10.1080/01621459.2016.1222284
Reisert, M., Kellner, E., Dhital, B., Hennig, J., Kiselev, V.G., 2017. Disentangling micro from mesostructure by diffusion MRI: A Bayesian approach. NeuroImage 147, 964–975. https://doi.org/10.1016/j.neuroimage.2016.09.058
Ridgway, J.P., 2010. Cardiovascular magnetic resonance physics for clinicians: part I. J. Cardiovasc. Magn. Reson. 12, 71. https://doi.org/10.1186/1532-429X-12-71
Roebroeck, A., Miller, K.L., Aggarwal, M., 2019. Ex vivo diffusion MRI of the human brain: Technical challenges and recent advances. NMR Biomed. 32, e3941. https://doi.org/10.1002/nbm.3941

Rohde, G. k., Barnett, A. s., Basser, P. j., Marenco, S., Pierpaoli, C., 2004. Comprehensive approach for correction of motion and distortion in diffusion-weighted MRI. Magn. Reson. Med. 51, 103–114. https://doi.org/10.1002/mrm.10677

Routier, A., Burgos, N., Díaz, M., Bacci, M., Bottani, S., El-Rifai, O., Fontanella, S., Gori, P., Guillon, J., Guyot, A., Hassanaly, R., Jacquemont, T., Lu, P., Marcoux, A., Moreau, T., Samper-González, J., Teichmann, M., Thibeau-Sutre, E., Vaillant, G., Wen, J., Wild, A., Habert, M.-O., Durrleman, S., Colliot, O., 2021. Clinica: An Open-Source Software Platform for Reproducible Clinical Neuroscience Studies. Front. Neuroinformatics 15, 689675. https://doi.org/10.3389/fninf.2021.689675

Ruthotto, L., Kugel, H., Olesch, J., Fischer, B., Modersitzki, J., Burger, M., Wolters, C.H., 2012. Diffeomorphic susceptibility artifact correction of diffusion-weighted magnetic resonance images. Phys. Med. Biol. 57, 5715–5731. https://doi.org/10.1088/0031-9155/57/18/5715

Ruthotto, L., Mohammadi, S., Heck, C., Modersitzki, J., Weiskopf, N., 2013. Hyperelastic Susceptibility Artifact Correction of DTI in SPM, in: Meinzer, H.-P., Deserno, T.M., Handels, H., Tolxdorff, T. (Eds.), Bildverarbeitung Für Die Medizin 2013, Informatik Aktuell. Springer Berlin Heidelberg, Berlin, Heidelberg, pp. 344–349. https://doi.org/10.1007/978-3-642-36480-8_60

Salvador, R., Peña, A., Menon, D.K., Carpenter, T.A., Pickard, J.D., Bullmore, E.T., 2005. Formal characterization and extension of the linearized diffusion tensor model. Hum. Brain Mapp. 24, 144–155. https://doi.org/10.1002/hbm.20076

Schilling, K.G., Grussu, F., Ianus, A., Hansen, B., Howard, A.F.D., Barrett, R.L.C., Aggarwal, M., Michielse, S., Nasrallah, F., Syeda, W., Wang, N., Veraart, J., Roebroeck, A., Bagdasarian, A.F., Eichner, C., Sepehrband, F., Zimmermann, J., Soustelle, L., Bowman, C., Tendler, B.C., Hertanu, A., Jeurissen, B., Verhoye, M., Frydman, L., van de Looij, Y., Hike, D., Dunn, J.F., Miller, K., Landman, B.A., Shemesh, N., Anderson, A., McKinnon, E., Farquharson, S., Dell'Acqua, F., Pierpaoli, C., Drobnjak, I., Leemans, A., Harkins, K.D., Descoteaux, M., Xu, D., Huang, H., Santin, M.D., Grant, S.C., Obenaus, A., Kim, G.S., Wu, D., Le Bihan, D., Blackband, S.J., Ciobanu, L., Fieremans, E., Bai, R., Leergaard, T.B., Zhang, J., Dyrby, T.B., Johnson, G.A., Cohen-Adad, J., Budde, M.D., Jelescu, I.O., 2025. Considerations and recommendations from the ISMRM diffusion study group for preclinical diffusion MRI: Part 2—Ex vivo imaging: Added value and acquisition. Magn. Reson. Med. 93, 2535–2560. https://doi.org/10.1002/mrm.30435

Sébille, S.B., Rolland, A.-S., Welter, M.-L., Bardinet, E., Santin, M.D., 2019. Post mortem high resolution diffusion MRI for large specimen imaging at 11.7 T with 3D segmented echo-planar imaging. J. Neurosci. Methods 311, 222–234. https://doi.org/10.1016/j.jneumeth.2018.10.010

Seif, M., David, G., Huber, E., Vallotton, K., Curt, A., Freund, P., 2020. Cervical Cord Neurodegeneration in Traumatic and Non-Traumatic Spinal Cord Injury. J. Neurotrauma 37, 860–867. https://doi.org/10.1089/neu.2019.6694

Skare, S., Andersson, J.L.R., 2001. On the effects of gating in diffusion imaging of the brain using single shot EPI. Magn. Reson. Imaging 19, 1125–1128. https://doi.org/10.1016/S0730-725X(01)00415-5

Smith, S.M., Jenkinson, M., Woolrich, M.W., Beckmann, C.F., Behrens, T.E.J., Johansen-Berg, H., Bannister, P.R., De Luca, M., Drobnjak, I., Flitney, D.E., Niazy, R.K., Saunders, J., Vickers, J., Zhang, Y., De Stefano, N., Brady, J.M., Matthews, P.M., 2004. Advances in functional and structural MR image analysis and implementation as FSL. NeuroImage 23, S208–S219. https://doi.org/10.1016/j.neuroimage.2004.07.051

Stejskal, E.O., Tanner, J.E., 1965. Spin Diffusion Measurements: Spin Echoes in the Presence of a Time-Dependent Field Gradient. J. Chem. Phys. 42, 288–292. https://doi.org/10.1063/1.1695690

Stikov, N., Campbell, J.S.W., Stroh, T., Lavelée, M., Frey, S., Novek, J., Nuara, S., Ho, M.-K., Bedell, B.J., Dougherty, R.F., Leppert, I.R., Boudreau, M., Narayanan, S., Duval, T., Cohen-Adad, J., Picard, P.-A., Gasecka, A., Côté, D., Pike, G.B., 2015. In vivo histology of the myelin g-ratio with magnetic resonance imaging. NeuroImage 118, 397–405. https://doi.org/10.1016/j.neuroimage.2015.05.023

Stroman, P.W., Wheeler-Kingshott, C., Bacon, M., Schwab, J.M., Bosma, R., Brooks, J., Cadotte, D., Carlstedt, T., Ciccarelli, O., Cohen-Adad, J., Curt, A., Evangelou, N., Fehlings, M.G., Filippi, M., Kelley, B.J., Kollias, S., Mackay, A., Porro, C.A., Smith, S., Strittmatter, S.M., Summers, P., Tracey, I., 2014. The current state-of-the-art of spinal cord imaging: Methods. NeuroImage 84, 1070–1081. https://doi.org/10.1016/j.neuroimage.2013.04.124

Sullivan, E.V., Rohlfing, T., Pfefferbaum, A., 2010. Quantitative fiber tracking of lateral and interhemispheric white matter systems in normal aging: Relations to timed performance. Neurobiol. Aging 31, 464–481. https://doi.org/10.1016/j.neurobiolaging.2008.04.007

Tabelow, K., Balteau, E., Ashburner, J., Callaghan, M.F., Draganski, B., Helms, G., Kherif, F., Leutritz, T., Lutti, A., Phillips, C., Reimer, E., Ruthotto, L., Seif, M., Weiskopf, N., Ziegler, G., Mohammadi, S., 2019. hMRI – A toolbox for quantitative MRI in neuroscience and clinical research. Neuroimage 194, 191–210. https://doi.org/10.1016/j.neuroimage.2019.01.029

Tabelow, K., Mohammadi, S., Weiskopf, N., Polzehl, J., 2015. POAS4SPM: A Toolbox for SPM to Denoise Diffusion MRI Data. Neuroinformatics 13, 19–29. https://doi.org/10.1007/s12021-014-9228-3

Tabesh, A., Jensen, J.H., Ardekani, B.A., Helpern, J.A., 2011. Estimation of tensors and tensor-derived measures in diffusional kurtosis imaging. Magn. Reson. Med. 65, 823–836. https://doi.org/10.1002/mrm.22655

Tournier, J.-D., Smith, R., Raffelt, D., Tabbara, R., Dhollander, T., Pietsch, M., Christiaens, D., Jeurissen, B., Yeh, C.-H., Connelly, A., 2019. MRtrix3: A fast, flexible and open software framework for medical image processing and visualisation. NeuroImage 202, 116137. https://doi.org/10.1016/j.neuroimage.2019.116137

Vallotton, K., David, G., Hupp, M., Pfender, N., Cohen-Adad, J., Fehlings, M.G., Samson, R.S., Wheeler-Kingshott, C.A.M.G., Curt, A., Freund, P., Seif, M., 2021. Tracking White and Gray Matter Degeneration along the Spinal Cord Axis in Degenerative Cervical Myelopathy. J. Neurotrauma 38, 2978–2987. https://doi.org/10.1089/neu.2021.0148

Van Essen, D.C., Ugurbil, K., Auerbach, E., Barch, D., Behrens, T.E.J., Bucholz, R., Chang, A., Chen, L., Corbetta, M., Curtiss, S.W., Della Penna, S., Feinberg, D., Glasser, M.F., Harel, N., Heath, A.C., Larson-Prior, L., Marcus, D., Michalareas, G., Moeller, S., Oostenveld, R., Petersen, S.E., Prior, F., Schlaggar, B.L., Smith, S.M., Snyder, A.Z., Xu, J., Yacoub, E., 2012. The Human Connectome Project: A data acquisition perspective. NeuroImage 62, 2222–2231. https://doi.org/10.1016/j.neuroimage.2012.02.018

Veraart, J., Novikov, D.S., Christiaens, D., Ades-aron, B., Sijbers, J., Fieremans, E., 2016. Denoising of diffusion MRI using random matrix theory. NeuroImage 142, 394–406. https://doi.org/10.1016/j.neuroimage.2016.08.016

Veraart, J., Rajan, J., Peeters, R.R., Leemans, A., Sunaert, S., Sijbers, J., 2013a. Comprehensive framework for accurate diffusion MRI parameter estimation. Magn. Reson. Med. 70, 972–984. https://doi.org/10.1002/mrm.24529

Veraart, J., Sijbers, J., Sunaert, S., Leemans, A., Jeurissen, B., 2013b. Weighted linear least squares estimation of diffusion MRI parameters: Strengths, limitations, and pitfalls. NeuroImage 81, 335–346. https://doi.org/10.1016/j.neuroimage.2013.05.028

Veraart, J., Van Hecke, W., Sijbers, J., 2011. Constrained maximum likelihood estimation of the diffusion kurtosis tensor using a Rician noise model. Magn. Reson. Med. 66, 678–686. https://doi.org/10.1002/mrm.22835

West, K.L., Kelm, N.D., Carson, R.P., Alexander, D.C., Gochberg, D.F., Does, M.D., 2018. Experimental studies of g-ratio MRI in ex vivo mouse brain. NeuroImage 167, 366–371. https://doi.org/10.1016/j.neuroimage.2017.11.064

Wilkinson, M.D., Dumontier, M., Aalbersberg, Ij.J., Appleton, G., Axton, M., Baak, A., Blomberg, N., Boiten, J.-W., da Silva Santos, L.B., Bourne, P.E., Bouwman, J., Brookes, A.J., Clark, T., Crosas, M., Dillo, I., Dumon, O., Edmunds, S., Evelo, C.T., Finkers, R., Gonzalez-Beltran, A., Gray, A.J.G., Groth, P., Goble, C., Grethe, J.S., Heringa, J., 't Hoen, P.A.C., Hooft, R., Kuhn, T., Kok, R., Kok, J., Lusher, S.J., Martone, M.E., Mons, A., Packer, A.L., Persson, B., Rocca-Serra, P., Roos, M., van Schaik, R., Sansone, S.-A., Schultes, E., Sengstag, T., Slater, T., Strawn, G., Swertz, M.A., Thompson, M., van der Lei, J., van Mulligen, E., Velterop, J., Waagmeester, A., Wittenburg, P., Wolstencroft, K., Zhao, J., Mons, B., 2016. The FAIR Guiding Principles for scientific data management and stewardship. Sci. Data 3, 160018. https://doi.org/10.1038/sdata.2016.18

Yiannakas, M.C., Kearney, H., Samson, R.S., Chard, D.T., Ciccarelli, O., Miller, D.H., Wheeler-Kingshott, C.A.M., 2012. Feasibility of grey matter and white matter segmentation of the upper cervical cord in vivo: A pilot study with application to magnetisation transfer measurements. NeuroImage 63, 1054–1059. https://doi.org/10.1016/j.neuroimage.2012.07.048

Zeeman, P., 1897. The Effect of Magnetisation on the Nature of Light Emitted by a Substance. Nature 55, 347–347. https://doi.org/10.1038/055347a0

Zhang, H., Schneider, T., Wheeler-Kingshott, C.A., Alexander, D.C., 2012. NODDI: Practical in vivo neurite orientation dispersion and density imaging of the human brain. NeuroImage 61, 1000–1016. https://doi.org/10.1016/j.neuroimage.2012.03.072

Zwiers, M.P., 2010. Patching cardiac and head motion artefacts in diffusion-weighted images. NeuroImage 53, 565–575. https://doi.org/10.1016/j.neuroimage.2010.06.014

Zwiers, M.P., Moia, S., Oostenveld, R., 2022. BIDScoin: A User-Friendly Application to Convert Source Data to Brain Imaging Data Structure. Front. Neuroinformatics 15, 770608. https://doi.org/10.3389/fninf.2021.770608

# 14 Publikation im Rahmen der Promotion

David, G.*, **Fricke, B.***, Oeschger, J.M., Ruthotto, L., Fritz, F.J., Ohana, O., Mordhorst, L., Sauvigny, T., Freund, P., Tabelow, K., Mohammadi, S., 2024. ACID: A Comprehensive Toolbox for Image Processing and Modeling of Brain, Spinal Cord, and Ex Vivo Diffusion MRI Data. Imaging Neuroscience. https://doi.org/10.1162/imag_a_00288

*Shared first authors

Björn Fricke: Conceptualization, Data curation, Formal analysis, Investigation, Methodology, Software, Validation, Visualization, Writing - original draft, Writing - review & editing.

# 15 Table of figures

while preserving tissue edges. For HySCO, contour lines of the corresponding structural image (displayed as red lines) are overlaid on a zoomed-in DW image both before (middle row) and after applying HySCO (bottom row). HySCO improves the alignment between the DW and the structural image. For the in vivo brain dMRI dataset (A), an inferior slice is shown that presents high susceptibility-related distortions, making the effect of HySCO more visible. For the ex vivo dMRI dataset (C), the effect of HySCO is shown in a slice (illustrated in yellow) orthogonal to the original one (illustrated in purple) to better visualize susceptibility-related distortions and their correction. Note that HySCO is applied as the final preprocessing step, that is, after applying msPOAS; however, the HySCO field map used for "unwarping" the diffusion-weighted images is estimated on the ECMOCO-corrected datasets, that is, before applying msPOAS. Rician bias correction (not explicitly shown here) should be applied either before (recommended: between msPOAS and HySCO, using the RBC module) or during model fitting (using the Rician bias correction option in NLLS). Diffusion signal models are fitted on the processed dataset; here, we display the maps of fractional anisotropy ($FA$) and mean kurtosis tensor ($MW$) from diffusion kurtosis imaging (DKI). The output from DKI can be used to compute biophysical parameters of the white matter; shown here is the map of Watson concentration parameter ($\kappa$) from the WMTI-Watson biophysical model. Note that for the in vivo brain dMRI dataset, the inferior slice displayed contains relatively little white matter; hence, we refrained from using a white matter mask. The less smooth appearance of the κ map is due to the low values in the gray matter. Source: Figure and modified caption reproduced from (David et al., 2024), published under CC BY 4.0 license. ..... 82

Figure 26: Bar plots displaying the Watson concentration parameter ($\kappa$) and axonal water fraction ($AWF$) within the five central slices of the corpus callosum and the lateral corticospinal tracts in the spinal cord (refer to Table 2 for details on the datasets). The corpus callosum was manually segmented, while the lateral corticospinal tracts were segmented

using the PAM50 spinal cord white matter atlas. The regions of interest are highlighted as red segmentation lines on the images. In the box plots, red horizontal lines represent literature values obtained from histology, while the red dotted line represents a literature value from the brain due to the absence of a corresponding value for the spinal cord. Values of orientation dispersion index reported in the literature were converted to $\kappa$ using Equation (1) in (Mollink et al., 2017). Within the corpus callosum, $\kappa$ values were (mean ± std) 10.82 ± 10.31 and 8.14 ± 5.13 when derived from the NODDI-DTI (single shell) and WMTI-Watson model (two shells), respectively. These values fall within the range of literature values obtained post-mortem using polarized light imaging (Mollink et al., 2017). $AWF$ values derived from NODDI-DTI (0.40 ± 0.24) and WMTI-Watson model (0.47 ± 0.13) were similar to literature values obtained using electron microscopy in a cynomolgus macaque (Stikov et al., 2015). Within the lateral corticospinal tracts, $\kappa$ values derived from NODDI-DTI were notably lower than those derived from WMTI-Watson (2.53 ± 0.19 vs. 6.04 ± 1.84) and were consistent with literature values obtained in a post-mortem specimen (Grussu et al., 2017). $AWF$ values derived from the WMTI-Watson model in the spinal cord were substantially higher (0.81 ± 0.03) compared to a literature value obtained in the brain (red dotted line). The estimation of $AWF$ for the spinal cord was not feasible using the NODDI-DTI model, as DTI-derived mean diffusivity ($MD$) values fell below the range where the NODDI-DTI model provides a valid representation (refer to Equation (4) in (Edwards et al., 2017)). This discrepancy could be attributed to either the underestimation of $MD$ due to kurtosis bias (Figure 21) or the invalidity of fixed compartmental diffusivities in the NODDI-DTI model. These results indicate that WMTI-Watson yields more accurate estimation of $\kappa$ and $AWF$ for the brain, while NODDI-DTI yields a more accurate estimation of $\kappa$ for the spinal cord. This could be a consequence of non-optimal $b$-values for kurtosis

## 16 List of Tables

# 17 Danksagung

An dieser Stelle möchte ich ein großes Dankeschön an all jene aussprechen, die mich während der letzten Jahre unterstützt und begleitet haben.

Zunächst gilt ein großer Dank meinem Doktorvater Prof. Dr. Siawoosh Mohammadi. Vielen Dank, dass Du jederzeit bei Fragen und Problemen erreichbar warst, um mit Deinem Fachwissen zu helfen und gemeinsam nach Lösungen zu suchen. Herzlichen Dank auch für Deine Unterstützung und Verständnis während meiner gesundheitlich schwierigen Zeit, da dies auf keinen Fall selbstverständlich ist.

Ein besonderer Dank gilt ebenso Herrn Dr. Karsten Tabelow. Deine permanente Hilfsbereitschaft und angenehme Diskussionskultur haben mir während meiner Doktorarbeit sehr geholfen.

Sehr danken möchte ich auch Prof. Dr. Lars Ruthotto und Prof. Dr. René Werner für die freundliche Unterstützung und Begleitung im Rahmen meines PhD-Programms.

Ein weiterer Dank geht an Dr. Gergely David, der mir sehr viel über das wissenschaftliche Arbeiten und Schreiben von Publikationen beigebracht hat.

Außerdem möchte ich dem gesamten *qMRI and in vivo histology* Team danken. Insbesondere Dr. Jan Malte Oeschger, Dr. Francisco Javier Fritz, Laurin Mordhorst, Nina Lüthi, Tobias Streubel und Behnam Ashtarayeh haben mich mit ihrem Fachwissen immer unterstützt, eine positive Atmosphäre und ein positives Miteinander in der Gruppe geschaffen.

Ich möchte außerdem meinen Eltern danken, die mir ein Umfeld geschaffen haben, in dem ich mich vollkommen auf meine Promotion konzentrieren konnte.

Einen Dank möchte ich auch an meine Freunde entrichten, insbesondere an Björn, Björn und Arne, bei denen ich in all den Jahren immer wieder schöne Momente und einen Ausgleich von der Arbeit finden konnte.

Abschließend möchte ich meiner Liebsten Tabea danken, die immer für mich da war, mich stets ermutigt hat und deren Lachen und Unterstützung diese Zeit meines Lebens unvergesslich gemacht hat.

# 18 Curriculum vitae

entfällt aus datenschutzrechtlichen Gründen

## Eidesstattliche Versicherung

Ich versichere ausdrücklich, dass ich die Arbeit selbständig und ohne fremde Hilfe, insbesondere ohne entgeltliche Hilfe von Vermittlungs- und Beratungsdiensten, verfasst, andere als die von mir angegebenen Quellen und Hilfsmittel nicht benutzt und die aus den benutzten Werken wörtlich oder inhaltlich entnommenen Stellen einzeln nach Ausgabe (Auflage und Jahr des Erscheinens), Band und Seite des benutzten Werkes kenntlich gemacht habe. Das gilt insbesondere auch für alle Informationen aus Internetquellen.

Soweit beim Verfassen der Dissertation KI-basierte Tools („Chatbots“) verwendet wurden, versichere ich ausdrücklich, den daraus generierten Anteil deutlich kenntlich gemacht zu haben. Die „Stellungnahme des Präsidiums der Deutschen Forschungsgemeinschaft (DFG) zum Einfluss generativer Modelle für die Text- und Bilderstellung auf die Wissenschaften und das Förderhandeln der DFG“ aus September 2023 wurde dabei beachtet.

Ferner versichere ich, dass ich die Dissertation bisher nicht einem Fachvertreter an einer anderen Hochschule zur Überprüfung vorgelegt oder mich anderweitig um Zulassung zur Promotion beworben habe.

Ich erkläre mich damit einverstanden, dass meine Dissertation vom Dekanat der Medizinischen Fakultät mit einer gängigen Software zur Erkennung von Plagiaten überprüft werden kann.

Datum Unterschrift